Unified Kinematic Scaling Relation in the Local Universe using Integral Field Spectroscopy Surveys

Dilyar Barat

A THESIS SUBMITTED FOR THE DEGREE OF DOCTOR OF PHILOSOPHY

Australian National University
Research School of Astronomy & Astrophysics

September 13, 2021

Declaration

I hereby declare that the work in this thesis is that of the candidate alone, except where indicated below or in the text of the thesis. The work was undertaken between January 2016 and January 2020 at the Australian National University (ANU), Canberra. It has not been submitted in whole or in part for any other degree at this or any other university.

This thesis has been submitted as a Thesis by Standard Format in accordance with the relevant ANU policies. In addition, Chapter 3 & 4 are self-contained articles published in a peer-reviewed journal. Parts of Chapter 5 are also published in a peer-reviewed journal. The status of each article and extent of the contribution of the candidate to the research and authorship is indicated below:

- **Chapter 3: Barat, Dilyar**; D'Eugenio, Francesco; Colless, Matthew; Brough, Sarah; Catinella, Barbara; Cortese, Luca; Croom, Scott M.; Medling, Anne M.; Oh, Sree; van de Sande, Jesse; Sweet, Sarah M.; Yi, Sukyoung K.; Bland-Hawthorn, Joss; Bryant, Julia; Goodwin, Michael; Groves, Brent; Lawrence, Jon; Owers, Matt S.; Richards, Samuel N.; Scott, Nicholas. *The SAMI Galaxy Survey: mass-kinematics scaling relations*, 2019, MNRAS, 487, 2924-2936. The candidate participated in observing runs of the SAMI Galaxy Survey, performed data analyses, and wrote the paper under the guidance of Francesco D'Eugenio and Matthew Colless.
- **Chapter 4: Barat, Dilyar**, D'Eugenio, Francesco; Colless, Matthew; Sweet, Sarah M.; Groves, Brent; Cortese, Luca. *SHαDE: survey description and mass-kinematics scaling relations for dwarf galaxies*,

2020, MNRAS, 498, 5885-5903. The candidate participated in the observing runs of the SHαDE-Survey, performed most of data reduction, analyses, and wrote the paper under the guidance of Francesco D'Eugenio and Matthew Colless. Sections 4.1, 4.2.2, 4.2.3, and 4.3 are contributed by Francesco D'Eugenio. Section 4.2.4 is contributed by Sarah M. Sweet. The remainder of the Chapter 4 is written by the candidate.

- **Parts of Chapter 5** are published in *The Taipan Galaxy Survey: Scientific Goals and Observing Strategy*, 2017, PASA, 34, 47-75. da Cunha, Elisabete; Hopkins, Andrew M.; Colless, Matthew; Taylor, Edward N.; Blake, Chris; Howlett, Cullan; Magoulas, Christina; Lucey, John R.; Lagos, Claudia; Kuehn, Kyler; Gordon, Yjan; **Barat, Dilyar**; Bian, Fuyan; Wolf, Christian; Cowley, Michael J.; White, Marc; Achitouv, Ixandra; Bilicki, Maciej; Bland-Hawthorn, Joss; Bolejko, Krzysztof Brown, Michael J. I.; Brown, Rebecca; Bryant, Julia; Croom, Scott; Davis, Tamara M.; Driver, Simon P.; Filipovic, Miroslav D.; Hinton, Samuel R.; Johnston-Hollitt, Melanie; Jones, D. Heath; Koribalski, Brbel; Kleiner, Dane; Lawrence, Jon; Lorente, Nuria; Mould, Jeremy; Owers, Matt S.; Pimbblet, Kevin; Tinney, C. G.; Tothill, Nicholas F. H.; Watson, Fred. Sections 5.3, 5.4, and 5.5 are contributed by Michael J. Cowley, Samuel R. Hinton, and Matt S. Owers, respectively.

Dilyar Barat

Acknowledgements

There are many factors that have gone into completing this thesis. Firstly I have to acknowledge the traditional owners of the land on which I carried out my research, the Ngunnawal people, of what is now known as the Australian Capital Territory. In addition, also the Gamilaraay and Kamilaroi people whose land Siding Spring Observatory resides, and finally the Atacameños of the Atacama desert, where Paranal observatory is located.

It takes a village to write a PhD, there are many people without whose help I would not have been able to cross the finish line, with the most important ones being Matthew Colless, Francesco D'Eugenio. You guys have not only been my supervisors, but also my mentors and friends. When things got tough, whether in my research or my personal life, I could always rely on you two to help me pull through. I feel extremely lucky to have had your guidance for the past 5 years.

I would also like to express my gratitude to Natalia Eiré Sommer, my partner in life. You made me a better and stronger person yet at the same time completely comfortable with showing vulnerability. Thanks to you, I found my way, and the determination to take the right path regardless of how difficult it will be.

To my family, my parents, and my brother, I am sorry that our values diverged along the way and there has been a lot of pain. I am still grateful that you tried your best in the way you knew how to accommodate my pursuit of education and knowledge.

To my counsellor Moira Turnbull, I appreciate your willingness to listen to my challenges and difficulties every month for the past three years. It may not seem it, but they have been incredibly helpful. The simple act of talking to you have made me feel relieved and understood.

Finally, I would like to acknowledge myself. For the past 5 years, there had not been a shortage of reasons to quit, family relationship fallout, continuing systemic oppression of my people, a break up, homelessness, and most recently a pandemic. All these things only made me a more resilient person. I learned to keep my mental health in check, I took on more responsibilities, and created my own options in a world that can sometimes seem hopeless. For me, the greatest result of this PhD is not the collection of discoveries and publications, but rather the discovery of myself. My heart goes out to everyone still going through all this, and those who have fallen along the way. I hope this academic journey that we all share has been a fruitful and successful way to define and shape ourselves to everyone.

I dedicate this thesis to all of my fellow Uyghur people who are currently struggling and suffering hardship. The time will come when we will shine.

Abstract

In a flat Universe with a cosmological constant and cold dark matter (the standard ΛCDM model), the total mass of a galaxy largely determines the motions of its stars and gas. Various scaling relations between the kinematics and masses of galaxies have long been observed, and characterised through a myriad observations and theoretical models. Traditionally, however, mass–kinematics scaling relations have been highly morphology-specific and the observational methods for the kinematic parameter have been specialised for the scaling relation of interest. Recently, thanks to the observational industrialisation provided by integral field spectroscopy (IFS) and the availability of large IFS galaxy surveys, the possibility of constructing a unified, morphology-independent, galaxy scaling relation has emerged.

In this thesis we study the dynamical scaling relation between galaxy mass (usually stellar mass, $M_\star$, but also baryonic and halo mass) and the generalised kinematic parameter $S_K = \sqrt{KV_{rot}^2 + \sigma^2}$ that combines rotation velocity V_{rot} and velocity dispersion σ, and has previously shown potential for unifying galaxies of all morphologies in a single scaling relation.

For the construction of this scaling relation, we make use of the data from the Sydney-AAO Multi-object Integral-field-spectroscopy (SAMI) galaxy survey. We investigate the applicability of the $\log M_\star$–$\log S_K$ scaling relation to galaxies ranging from elliptical galaxies to late-type spiral galaxies. We also investigate the effect of using either the stars or the gas component of galaxies as the kinematic tracer, optimise the combination of V_{rot}

and σ by varying the K value in the S_K parameter, and compare the kinematic measurements from IFS survey to single-fibre spectroscopy with the intention of applying the findings to large-scale single-fibre surveys.

We find that the $\log M_\star$–$\log S_K$ relation: (1) is linear above limits set by properties of the samples and observations; (2) has slightly different slopes when derived from stellar and gas kinematic measurements; (3) applies to both early-type and late-type galaxies, with smaller scatter than either the Tully-Fisher relation ($\log M_\star$–$\log V_{rot}$) for late types or the Faber-Jackson relation ($\log M_\star$–$\log \sigma$) for early types; and (4) has scatter that is only weakly sensitive to the value of K, with minimum scatter for K in the range 0.4–0.7, weakly dependent on galaxy type. We also find that while S_K and aperture velocity dispersion (e.g. $\sigma_{3''}$) are in general tightly correlated, the $\log M_\star$–$\log S_K$ relation has less scatter than the $\log M_\star$–$\log \sigma_{3''}$ relation.

The linear galaxy scaling relation from SAMI shows a lower limit that may be due either to an intrinsic mass limit or to an instrumental resolution limit. To explore the origin of this apparent linearity limit, we initiated the Study of Hα from Dwarf Emissions (SHαDE), a high spectral resolution (R=13500) Hα integral field survey of 69 dwarf galaxies with stellar masses in the range $10^6 < M_\star < 10^9 M_\odot$. We describe the SH$\alpha$DE survey goals, design, observations and data reduction processes. We use SHαDE to extend the study of the $\log M_\star$–$\log S_K$ scaling relation to include low-mass dwarf galaxies in an attempt to make the scaling relation truly universal. We find that the $\log M_\star$–$\log V_{rot}$ Tully-Fisher relation is consistent with being linear down to the lowest masses we study. In contrast, the $\log M_\star$–$\log \sigma$ Faber-Jackson relation appears to have a lower limit due to a floor in the internal velocity dispersion of the Hα-emitting gas of approximately $20\,\mathrm{km\,s^{-1}}$. Consequently, the $\log M_\star$–$\log S_{0.5}$ scaling relation also has a

lower limit at around a stellar mass of $M_\star \sim 10^{8.6} M_\odot$.

We study the options of replacing galaxy stellar mass with baryonic mass or dark matter halo mass in pursuit of creating a linear scaling relation at all masses. Replacing stellar mass with total baryonic mass, using estimates for the gas mass, reduces the severity of the non-linearity but does not remove the lower limit. However, making some simple additional assumptions to provide estimates of the galaxies' dark matter halo masses yields a $\log M_h$–$\log S_{0.5}$ scaling relation that: (1) is linear over the observed range; (2) has no apparent limit at low masses and reduced curvature at high masses; and (3) brings galaxies of all masses and morphologies onto the virial relation.

Scaling relations like the Tully-Fisher relation and the Fundamental Plane are powerful tools for measuring galaxy distances and peculiar velocities for cosmological studies. One of the motivations for exploring a generalised scaling relation is to develop such a tool, one that is applicable to all the galaxies in large-scale single-fibre spectroscopy surveys and in particular to the planned Taipan galaxy survey. A key step towards that goal is the development of the Taipan Live Data Reduction (TLDR) software, a highly automated data reduction pipeline with the capability to precisely measure aperture velocity dispersions for a hundred thousand galaxies (an order of magnitude more than in any previous survey). Although delays in commissioning the survey instrument have prevented this potential application of the generalised scaling relation being realised in time for this thesis, we use mock data to validate the functionalities and performance of TLDR and demonstrate its capabilities for measuring redshifts and both absorption-line and emission-line velocity dispersions. We outline the further work that needs to be done to tune TLDR to the as-built survey instrument and future extensions that could improve its performance and accuracy.

A generalised mass-kinematics scaling relation such as that studied in this thesis is a powerful tool. We expect that such scaling relations will soon be in common use for exploring the properties and formation histories of galaxies and for measuring galaxy distances and peculiar velocities in order to measure the mass distribution in the Universe and test the nature of gravity on large scales.

Contents

List of Figures

List of Tables

Chapter 1

Introduction

The night sky has always been a place that triggered a sense of awe and inspired the spirit of humankind. Indigenous cultures all around the world share stories that connect the wonders of the heaven to their lives. As a species, we continually looked up, to see all that is provided by the mysterious night, to absorb a sense of wonders, and to experience transcendence. With an appetite to see more and to know more, we continued our search, and the Universe has never failed to amaze with its wonders. As we piece together all that we have found, patterns emerge. A seemingly chaotic Universe shows us its intricate connections and order. We see commonalities in galaxy behaviours, we see larger structures arise from interaction between galaxies, we see rules that even the giants in the Universe must obey just as the dwarfs. The Universe grows and scales in harmony, with all its constituents in coordination. In this thesis we set out to study these building blocks of the Universe, to see whether these scaling relations can show us the fundamental physics behind galaxies' origins and behaviours.

1.1 Galaxies

1.1.1 Origin of galaxies

Galaxies are the fundamental building blocks of the Universe. They harbour everything from dust to planets, stars, and star clusters. Galaxies exist as islands of substructures, where stars, gas and planets intertwine over many systems in a complex choreography. The dynamics within and between galaxies form the forever-evolving cosmology.

The evolution of the Universe has always been a challenge for astronomers. For most of the time that astronomers have been observing the cosmos, it was believed the Universe was static—it had always been the same and would forever be the same (a notion later coined as the *cosmological principle,* Bondi & Gold 1948; Hoyle 1948). Einstein, in his General Theory of Relativity (GR), which describes the structure of space-time within the Universe, chose to add a cosmological constant (Λ) to remain consistent with the belief of a static Universe. Only just shy of a century ago, when Edwin Hubble and Georges Lemaître (Hubble 1929; Lemaître 1931) compared the distances to nearby galaxies to their motions, was it revealed that the Universe was expanding. This notion of an expanding Universe revolutionised the field of astronomy and simultaneously made the cosmological constant seem redundant. However, the significance of Λ was recently re-established, for a reason ironically opposite to that for which Einstein introduced it, with the discovery of the accelerating expansion of the Universe (Riess et al. 1998; Perlmutter et al. 1999). With these discoveries, it was clear that the Universe had a beginning and it will continue to expand eternally.

Combining the *cosmological principle* and the equations of GR, astronomers for the first time had a mathematical description of the Universe. By exploring the static and expanding scenarios of GR, in 1922 Alexander Friedmann derived models that would provided physical quantities that described the size (scale factor, a), matter and energy densities (Ω), as well as their evolution (see Mo et al. 2010, p16). With the Friedmann models, astronomers could now predict and back-track the evolution of the Universe as well as the formation of structures such as galaxies, and galaxies clusters.

Our understanding of galaxies was transformed once again just a few decades ago with the introduction of dark matter. The presence of dark matter suggested that galaxies consisted of more than stars and gas; there was another major component to galaxies to be learnt and understood. Since dark matter was proposed, many models and candidates have been employed to explain the origin and effects of dark matter. Currently the most popular and widely tested model is Cold Dark Matter (CDM). In the field of particle astrophysics, the term 'cold' corresponds to the dark matter particle being more massive than 1keV (Mo et al. 2010, p21). Cold dark matter and and the cosmological constant now form the basis of our standard model of the Universe, commonly called the ΛCDM cosmology. In this cosmology, dark energy associated with the cosmological constant makes up 70% of the energy density in the Universe, dark matter makes up 25%, and the remaining 5% consists primarily of the baryonic matter that forms everything we directly observe electromagnetically (see Wechsler & Tinker 2018, for details). It is this mere 5% of the Universe that we study and from which obtain most of our knowledge about the cosmos.

Dark matter is now believed to be a standard and critical component in the formation of galaxies. Within the expanding Universe, dark matter forms an over-density, a 'halo', that provides a gravitational well allowing baryonic matter to withstand the expansion and collapse under gravity. Since its discovery, many studies have been performed to investigate various properties of dark matter haloes, such as the progenitor mass distributions (Bond et al. 1991), merger histories (Lacey & Cole 1993), spatial clustering (Mo & White 1996), density profiles (Navarro et al. 1997), halo shapes (e.g. Jing & Suto 2002), substructure (e.g. Moore et al. 1998; Klypin et al. 1999), and angular-momentum distributions (Warren et al. 1992; Bullock et al. 2001). These studies inspired the development of more sophisticated semi-analytical models and hydrodynamical simulations. These two approaches complement each other, and have been pursued by many authors to form a better understanding of galaxy formation that can withstand tests on both large and small scales.

Direct observation of galaxy dark matter haloes has proven difficult with the currently available technologies. However, as incubators for galaxy formation, dark matter haloes can be studied by observing the properties of their products, i.e. the galaxy/-galaxies within the dark matter halo, and by observing the halo's influence on the galaxy. Within dark matter haloes, galaxies of all types are formed, and commonly, their internal properties are correlated with each other. For example, galaxy kinematic scaling relations correlate stellar and gas kinematics within the galaxies to some variants of their mass. While these scaling relations are constructed from the observables associated with the product galaxy, one can infer properties of the dark matter halo that surrounds them, as well as galaxy-halo connections. With the advent of galaxy scaling relations for various types of galaxies, astronomers are provided with a tool to peer into dark matter haloes and get a much better understanding of matter that makes up 25% of the Universe. It is the main goal of this thesis to investigate various kinematic galaxy scaling relations, to strive for better understanding of galaxy formation and kinematics.

1.1.2 Galaxy classifications & kinematics

With our current observations and understanding of galaxies we infer knowledge of the Universe. However, less than a century ago, galaxies did not exist as a concept. Thanks to the development of cosmic distance indicators such as Cepheid variable stars (Leavitt 1908), we were able to determine that our neighbouring Andromeda galaxy was in fact external to our own galaxy (Hubble 1926). This discovery proved our Milky Way galaxy was not the only one in the Universe and it became the prototype for a new class of astronomical objects. This initiated the new field of astronomical studies called extragalactic astronomy. Understanding the morphological types, formation history, kinematics, and other properties of galaxies is now more important than ever to understand the Universe at large.

1.1.2.1 Galaxy morphology

Looking out into the cosmos, astronomers have observed that galaxies exist in many shapes, sizes, and colours. This is an exercise that Edwin Hubble performed as he surveyed the local Universe (Hubble 1936). He noticed that some galaxies had smooth, elliptical, light profiles and some galaxies had flattened disks, sometimes with spiral arms or distinct dusty features. Hubble ordered his observations into a sequence based on the prominence of their features. This ordering is now often referred to as Hubble's sequence. Hubble's sequence divides galaxies into four broad classes:

- *Elliptical galaxies*: These galaxies are observed to lack distinct features and have smooth light profiles with elliptical isophotes. Most distinctly, elliptical galaxies do not have spiral arms.

- *Spiral galaxies*: As the name suggests, this class of objects have spiral arms and are gas-rich with abundant star-forming regions. Stars and gas within spiral galaxies predominantly reside in a plane and form a disk. Some spiral galaxies may also contain either a central bulge or a central bar structure.

- *Lenticular/S0 galaxies*: This class of galaxies share similarities with both elliptical and spiral galaxies. Lenticular galaxies are like elliptical galaxies in that they have smooth light profiles without spiral arms or active star formation. However, much like spiral galaxies, lenticular galaxies are observed to have a disk structure.

- *Irregular galaxies*: Irregular galaxies lack obvious symmetry. They do not have a central bulge, a well-defined disk, or spiral arms. Their light profiles are generally uneven and scattered with star-forming regions.

It is worth mentioning that the detail one can observe from photometry is often biased by the length of exposure, or depth, of the image. The work of Duc et al. (2011) has shown that, with sufficient exposure, galaxies thought to be elliptical galaxies can display spiral arm structures. This suggests that, while galaxies can be diverse on initial appearance, with greater depth of detail they might share more in common than we previously thought.

Another category of galaxies that was not included in Hubble's sequence is dwarf galaxies. Conventionally, dwarf galaxies refer to faint galaxies with magnitude $\mathscr{M}_B \geq -18$ (Sandage & Binggeli 1984). While they can be found as field galaxies that exist by themselves without being gravitationally bound to other structures, this type of galaxy is commonly found as satellites of larger and more massive galaxies.

While Hubble's system of galaxy classification was devised long ago, it is still often referenced and used as a basis for astronomical investigation (see Sandage 2005, for an in-depth review). Today, elliptical and lenticular galaxies are commonly grouped together and called early-type galaxies (ETG), while spiral and irregular galaxies are grouped together and called late-type galaxies (LTG). Note that, while these galaxies are referred to as 'early' and 'late', these descriptive words are not indications of their evolutionary stage.

There are various other classification schemes for galaxies beyond Hubble's sequence. For example, galaxies can be divided into *gas-rich* or *gas-poor* based on their gas content; *starburst* and *quiescent* based on their observed star formation rate; *fast-rotators* and *slow-rotators* based on the angular momentum of stars; and *normal* and *active* based on the activity of central nuclei (Mo et al. 2010, p38). Each classification scheme is useful for a given set of criteria and science application. In this thesis, we will generally follow the conventional typing of the Hubble sequence and classify our galaxies based on the visual observations.

1.1.2.2 Early-type galaxies

ETGs, as mentioned previously, broadly consist of two sub-classes of galaxies, elliptical galaxies and lenticular galaxies. ETGs in the local universe have compact, concentrated light profiles (e.g. D'Onofrio et al. 1994; Bertin et al. 2002; Graham & Guzmán 2003; Ferrarese et al. 2006; Kormendy et al. 2009). The colours of ETGs derived from multiple bands show that they in general have red colours (e.g. Sandage & Visvanathan 1978; Bell et al. 2004; Schlafly & Finkbeiner 2011), suggesting the stellar population of ETG stars are older and metal-rich (e.g. Stanford et al. 1998; Trager et al. 2000; Thomas et al. 2005; Gallazzi et al. 2005). The kinematics of stars within ETGs indicate they are predominantly supported by velocity dispersion rather than uniform rotation (e.g. Saglia et al. 1997; Neistein et al. 1999; Cappellari et al. 2007; Pota et al. 2013). While it has long been known that ETGs may have some cold gas, they are still gas-poor compared to LTGs of the same mass (e.g. Lees et al. 1991; Young 2002; Young et al. 2011). Elliptical galaxies have a triaxial spheroidal form, while lenticular galaxies have a spheroidal bulge component but also a disk component. Physical structure, low gas content and low star-formation rate together form the basis of classifying a galaxy as an ETG.

Galaxy scaling relations play an important role in the study of ETGs. The kinematics of ETGs follow multiple scaling relations with multiple other galaxy properties. The earliest scaling relation derived from ETGs was that between the luminosity (L) of the galaxy and the central stellar velocity dispersion (σ). This relation is known as the Faber-Jackson (FJ hereafter, Faber & Jackson 1976) relation, and had the form:

$$L \propto \sigma^4 \tag{1.1}$$

Kormendy (1977) discovered another correlation between galaxy surface brightness $\langle I \rangle_e = L/(2\pi R_e^2)$ and galaxy size (R_e). This relation is often seen in the form of a radius-luminosity relation, where the surface area of the galaxy is used to reduce the covariance between the major and minor axes of the galaxy.

A decade after the discoveries of the FJ relation and the Kormendy relation, with the availability of larger galaxy samples, it became apparent that these two relations are in fact both projections of a single plane, now known as the Fundamental Plane (FP hereafter, Djorgovski & Davis 1987; Dressler et al. 1987). The FP correlates the surface brightness ($\langle I \rangle_e$), size (R_e), and velocity dispersion (σ_0) of ETGs. It is found to hold for both elliptical and S0 galaxies, and has the form:

$$\log R_e = a \log \sigma_0 + b \log\langle I_e \rangle + \text{constant} \tag{1.2}$$

The FP has been evolving since its initial discovery. One of the most popular adaptations of the FP involves replacing the luminosity parameter with a stellar mass estimate ($M_\star$) using a mass-to-light ratio (M/L) based on some measure of the stellar population. This modification was motivated by the Virial Theorem, of which a natural consequence is the correlation $M_\star \propto \sigma^2 R_e$. This modified FP, sometimes known as the mass plane, was found to have significantly less scatter than the original version (e.g. Jorgensen et al. 1996). However, the observed mass plane of ETGs is often found to deviate from the virial predictions. This deviation of the FP from the virial prediction is called the tilt of the FP (e.g. Ciotti et al. 1996; Trujillo et al. 2004; Humphrey & Buote 2010; Bernardi et al. 2020).

The tilt of the FP has been an active area of research among astronomers; see Cappellari (2016) for a detailed review. In brief, the tilt is the result of a combination of three main factors: the M/L used to calculate stellar mass (Prugniel & Simien 1996; Forbes et al. 1998); the varying surface brightness profiles of ETGs (Ciotti et al. 1996; Graham & Colless 1997; Prugniel & Simien 1997; Bertin et al. 2002; Trujillo et al. 2004); and the fraction of dark matter within the sampling regions (Renzini & Ciotti 1993; Borriello et al. 2003; Tortora et al. 2012). As all these factors are closely associated with the intrinsic properties of galaxies, locating each galaxy on the FP and understanding the tilt of the FP provides valuable insight on the nature and formation of galaxies.

The FP is not only useful in studying the formation of ETGs, but also as a distance indicator. In the luminosity version of the FP, both L and σ are distance independent quantities that can be obtained via photometry and spectroscopy. R_e is the only parameter that has a distance component in its measurement. Therefore a well-calibrated FP can be used as a tool to determine distance to galaxies that reside beyond the limit of Cepheid variables (Saulder et al. 2019). For this reason many large astronomical surveys target ETGs exclusively and use the FP to obtain distances for studying large-scale structure in the Universe (e.g. 6dFGS: Campbell et al. 2014, Taipan: da Cunha et al. 2017).

1.1.2.3 Late-type galaxies

The structure of LTGs, comprising disk galaxies and irregular galaxies, is very different from ETGs. Disk galaxies are structurally more complex than elliptical and lenticular galaxies. Stars and gas in disk galaxies are supported by ordered rotation and form a relatively thin plane. Disk galaxies often have spiral arms, a bulge component and/or a central bar (for a detailed introduction see Mo et al. 2010; Binney & Tremaine 2008). Some authors subdivide spiral galaxies into early-spiral and late-spiral classes based on the presence or absence of a bulge (e.g. van den Bergh 1976; Gioia & Fabbiano 1987; Pohlen & Trujillo 2006; Lee et al. 2019). LTGs are typically gas-rich and light from LTGs nearly always shows dust absorption at some level. With an abundance of molecular gas, LTGs are actively star-forming; as a consequence, the stellar populations of LTGs are generally young. As a class of galaxies that is diverse in its members, and contains a wealth of information through its gas emission lines, LTGs are interesting to many authors that investigate galaxy formation and evolution (Searle et al. 1973;

Shostak 1978; Boselli & Gavazzi 2006; Schawinski et al. 2014).

The gas component of LTGs is also different from ETGs. Compared to the hot and ionised gas found in ETGs, LTGs tend to be rich in neutral and molecular gas (HI and H_2) (e.g. Young & Scoville 1991; Pogge & Eskridge 1993; Casoli et al. 1998). In disk galaxies, there is great amount of overlap between molecular gas and star-forming regions, as molecular gas clouds are nurseries of star formation. The distribution of neutral gas, however, extends well beyond the bounds of the galaxy disks (Rownd et al. 1994; Ryan-Weber et al. 2003). Studies of the neutral and molecular gas can provide important insight into the dark matter distribution of LTGs (e.g. Martimbeau et al. 1994; van Driel & van Woerden 1994; Kalberla et al. 2007).

Unlike ETGs, gas and stars in LTGs reside in a plane and move in approximately circular orbits (see Binney & Tremaine 2008, for more in-depth explanations on orbits). Studies of LTGs often involve the construction of the rotation curve of a disk galaxy. A rotation curve presents the circular velocity (V) distribution of stars or gas as a function of the orbit's radius (R). Both variables V and R often have different definitions across studies and are measured differently based on the availability of data, and tracers for the kinematics have also seen many options over the years based on the science objective and instrument design (e.g. Lelli et al. 2019). However, the concept of the rotation curve still remains a powerful tool to quantify the dominance of rotation in a disky galaxy system.

The kinematics of LTGs and their rotation curves hold important information regarding their formation and structures (see p54 of Mo et al. 2010, for discussion on rotation curves). The rotation of gas and stars reflects the gravitational potential from the enclosed mass; in a simplistic case, it follows:

$$M(r) = rV(r)^2_{rot}/G \tag{1.3}$$

where r is the radius at which the velocity (V) was measured, and G is the gravitational constant. Observation of numerous galaxy rotation curve shows that at large radius $V(r)$ is approximately constant. This leaves mass only dependent on radius, and predicts a linear accumulation of mass as the radius increases. However this is in conflict with the decreasing luminosity of disk galaxies at large radius (Freeman 1970). This observation of LTGs' flat rotation curves pointed towards the concept of an unseen mass distribution and this notion later evolved into the theory of galaxy dark matter haloes (e.g. Faber & Gallagher 1979; Roberts 2008).

Most LTGs follow the same kinematic scaling relation. By observing rotation velocities at large radius using the 21cm HI line in a small number of galaxies, Tully & Fisher (1977) discovered that there existed a scaling law that correlated LTGs' rotation velocities and their luminosities. This scaling relation has since been tested with large numbers of galaxies observed at multiple wavelength ranges with different tracers (e.g. Ponomareva et al. 2017), and while there are differences in slopes, intercepts and scatter due to sample variation and different construction methods, the essential correlation between galaxy rotation velocity and luminosity remains a tight scaling relation with form close to:

$$L \propto V^4 \tag{1.4}$$

The Tully-Fisher (TF) relation proven to be a valuable scaling relation in many areas of study. As such, there are astronomical surveys dedicated to obtaining a fine-tuned and well-calibrated TF relation (e.g. 2Mass Tully-Fisher Survey Masters et al. 2008). Like the FJ relation and FP for ETGs, the TF relation can also be used as a distance estimator for LTGs. By sampling the velocity distribution of disk galaxies and comparing it to the observed luminosity, one can use the TF relation to obtain a distance to the galaxy through the difference between luminosities. Beyond this, the TF relation also enables us to get a better understanding of disk galaxy formation and evolution, as it allows us to compare the dynamical mass and luminosity of disk galaxies. To date, theoretical models and simulations that can reasonably characterise disk galaxies are yet to reliably produce a TF relation with sensible slope, intercept and scatter without some degree of fine tuning (Somerville & Davé 2015). Understanding the TF relation in a galaxy formation context therefore remains an important area of studies.

1.1.2.4 Dwarf galaxies

Historically, dwarf galaxies are classified as galaxies with B-band magnitudes $\mathscr{M}_{\rm B} \gtrsim -18$ (Sandage & Binggeli 1984). As there is no theoretical lower limit to the dwarf galaxy magnitude, ultra-diffuse faint dwarf galaxies are still being discovered (e.g. van der Burg et al. 2016; Trujillo et al. 2017; Park et al. 2019; Lim et al. 2020). This makes dwarf galaxies the most abundant galaxies in the Universe. Since by definition dwarf galaxies are faint, most of their discovery has been limited to the local Universe, or indeed the Local Group (LG). Studies of LG dwarf galaxies have revealed a tremendous amount of information on the formation of galaxies and the dark matter distribution in the Universe. One of the discoveries from LG dwarf galaxies is that low-luminosity dwarf galaxies are metal-poor, making them excellent proxies for studying galaxy formation in the early Universe (Mateo 1998; Simon 2019). With the advantage of small distances, dwarf galaxy stellar populations can be resolved more easily with currently available instruments. With their large span of luminosity, dwarf galaxies enable astronomers to study how various galaxy properties, such as dark matter content, interstellar medium, and star-formation history, scale with their luminosity. Given their low luminosity and low stellar mass, the LG dwarf galaxies appear to the most dark-matter-rich galaxies in the Universe. Hence the formation of dwarf galaxies provides a constraint on the ΛCDM model of galaxy formation at the smallest viable scale (e.g. Porter et al. 2011; Bullock & Boylan-Kolchin 2017; Buckley & Peter 2018; Strigari 2018).

1.2 Objectives and contributions

1.2.1 The quest to improve scaling relations

Thanks to large-scale N-body simulations, the expected structure, abundance, and clustering of cold dark matter haloes in ΛCDM is well-understood (see Frenk & White 2012, for a review). The relationship between the stellar mass of a galaxy and its dark matter halo is commonly approximated using a technique called 'abundance matching', where galaxies are assigned to haloes respecting their relative mass rankings (Behroozi et al. 2013). Most recently this approximation and its predicted relation between galaxy mass and halo mass was confirmed using hydrodynamical simulations of galaxy formation for galaxies with stellar mass ($M_\star$) in the range $10^7 - 10^8 M_\odot$ (e.g. Vogelsberger et al. 2014; Schaye et al. 2015). With the availability of abundance matching provided by simulations, it is now more important than ever for observations to provide accurate stellar mass measurement for us to further characterise the mechanisms of galaxy-formation within dark matter haloes.

While *total* (i.e. dynamical, gravitating) mass can, at least in principle and in many cases in practice, be measured directly from dynamics (e.g. via rotation curves), measuring *stellar* mass has proven to be a challenging task. In fact, to date, there is no way to directly measure the stellar mass of a galaxy. Instead, it has always been an inferred quantity, commonly from photometry accompanied by an assumed light-to-mass ratio (see Courteau et al. 2014, for a review on galaxy mass estimation). It is not the goal of this thesis to challenge the assumptions behind stellar mass estimates from photometry; rather, this thesis sets out to improve, and attempt to generalise, the correlation between galaxy kinematics and this photometry-derived stellar mass (i.e. between total dynamical mass and stellar mass).

Previously, in section 1.1.2, we have seen that kinematic scaling relations exist for both early-type and late-type galaxies: namely the FJ and FP relations and the

TF relation respectively. These relations all began as kinematics-luminosity relations. However, in the pursuit of reducing the scaling relation scatter, it was found that if luminosity were to be replaced by mass estimates (of various sorts), the scatter of the relations is reduced substantially (see Cappellari et al. 2013, for the FP relation of ETGs using stellar mass, see McGaugh et al. 2000, for the TF relation of LTGs using baryonic mass). Over time, the study of kinematic scaling relations has become the study of mass-kinematics scaling relations.

On the observational side, another major advance in studying and improving the mass-kinematics relations came from the availability of large-scale Integral Field Spectroscopy (IFS) surveys. For example, Cappellari et al. (2011) showed that using galaxy kinematic maps allows one to construct Jeans anisotropic multi-Gaussian-expansion (JAM) models to obtain accurate and unbiased stellar mass estimate (Cappellari 2012). It also simultaneously provided systemic velocity and velocity dispersion at individual locations of the galaxy within the field of view. This allowed for the construction of *effective* (or *aperture*) velocity dispersion $\sigma_e \approx \langle V^2 + \sigma^2 \rangle^{1/2}$, which included the effect of rotation velocity (V) as well as local velocity dispersion (σ), covering an area that is no longer constricted to the tradition single-fibre aperture, but up to of order the half-light radius (R_e). These advances led to the conclusion that the stellar-mass FP has no intrinsic scatter and confirmed that the FP, once corrected for the mass-to-light ratio, indeed has the slope predicted from the virial theorem (Cappellari et al. 2013).

Over the years, there have also been many attempts to minimise the scatter of the TF relation by including the half-light radius (e.g. Zwaan et al. 1995; Courteau & Rix 1999; Pizagno et al. 2007; Avila-Reese et al. 2008; Hall et al. 2012; Zaritsky et al. 2014; Tonini et al. 2014), but they all showed no significant improvement. The most significant improvement on the TF relation came when it was found that the stellar mass version of the relation broke down when it reached galaxies with velocity less than ~100 $\mathrm{km\,s^{-1}}$. This led to the use of baryonic mass ($M_{\rm bar}$), which includes the cold gas mass, and the finding that the baryonic-mass TF relation (BTF) was linear over ∼5 decades in $M_{\rm bar}$ (e.g. McGaugh et al. 2000; McGaugh 2005; Lelli et al. 2016; Iorio et al. 2017).

Thanks to the availability of large-scale IFU surveys, the next wave of effort to improve galaxy kinematic scaling relations came from the pursuit of creating a generalised kinematic scaling relation (Cortese et al. 2014; Aquino-Ortíz et al. 2018; Barat et al. 2019; Gilhuly et al. 2019). This campaign aims to combine the TF and FJ relation to create a universal scaling relation that produces a linear scaling relation for galaxies of all morphologies. Although mass definitions vary, all of these studies use the 'combined velocity scale' parameter S_K (Weiner et al. 2006):

$$S_K^2 = KV_{\rm rot}^2 + \sigma^2 \tag{1.5}$$

where K is generally assumed to be constant (Kassin et al. 2007) and is often assumed to take the value $K = 0.5$ (Cortese et al. 2014; Aquino-Ortíz et al. 2018; Barat et al. 2019; Gilhuly et al. 2019). Through the combination of rotation velocity and velocity dispersion, the S_K parameter brings rotation-supported and pressure-supported systems onto the same scaling relation. From a theoretical point of view, this combination is a simplified asymmetric-drift correction, that includes the effects of anisotropy, velocity dispersion profile, and density profile (Lelli et al. 2014). Although simplistic in formalism, the $M - S_{0.5}$ relation has shown great potential as a robust scaling relation applicable to galaxies of all morphologies, as well as to the use of either stars or gas as the kinematic tracer. This thesis studies the application of this generalised kinematic tracer in depth, with the goals of characterising its advantages over traditional kinematic parameters used in morphology-specific relations and determining its limitations.

1.2.2 Thesis objectives

This thesis is motivated by previous studies of galaxy scaling relations. As we discussed earlier in this chapter, galaxy kinematic scaling relations reflect the total mass distribution in galaxies. They thus provide information on the dark matter halo that dominates the total mass (at least at large radii) and is fundamental to the formation of galaxies. Therefore there is a need for a fundamental scaling relation that is invariant with respect to galaxy morphology, star formation history, and dark matter content. Recent works point toward the $M - S_{0.5}$ scaling relation as a good candidate for investigation.

To characterise the effectiveness of the $M - S_{0.5}$ scaling relation, we set out in this thesis to make use of the data obtained by the Sydney-AAO (Australian Astronomical Observatory) Multi-object IFS (hereafter SAMI, Croom et al. 2012) galaxy survey. We use the SAMI survey data to construct the $M - S_{0.5}$ scaling relation and to compare it to the TF and FJ relations. We pay close attention to the $M_\star$ version of the scaling relation, to see if $M_\star - S_{0.5}$ also suffers from a linearity limit such as that plaguing the stellar-mass TF relation. We compare the S_K parameter to the velocity dispersion measured from the integrated spectrum within an aperture in an effort to apply the scaling relation to large single-fibre spectroscopy surveys (Barat et al. 2019). Where the SAMI survey hits its limitations, in terms of $M_\star$ range and instrument resolution limits, we obtain additional observations of dwarf galaxies with high spectral resolution to extend the scaling relation to dwarf galaxies (SHαDE, Barat et al. 2020). With the additional data, we also explore alternative mass estimates for the scaling relation, namely baryonic mass (M_b) and halo mass (M_h).

A unified galaxy scaling relation should not only apply to all galaxy types, it should also be effectively and easily applied to large samples of galaxies. Then it can be used with the diverse array of existing and upcoming galaxy surveys to probe the local and distant universe and further enrich and expand our understanding of the cosmos.

1.3 Overview of the thesis

In this thesis, we explore galaxy scaling relations in the local universe. In order to make this exploration, we first must begin with observations.

In Chapter 2, we present galaxy surveys that specifically target the local universe and are ideal for the purpose of this thesis. In this chapter, we will cover the basic design, setup, and specifications of the instruments, and discuss the advantages and the limitations of each instrument and the surveys associated with them. We will briefly showcase the scientific goals of each survey and explain how these goals aid in the formation of this thesis, and how this thesis complements and assist the goals of the surveys. Once we have covered the origin of the data used in this thesis, we move on to studying the unified scaling relation.

In Chapter 3, we use the SAMI survey to examine the conventional TF and FJ relations and to construct a unified galaxy scaling relation that can be used without morphological selection of galaxies (Barat et al. 2019; see also Chapter 2.1). We compare our work to previous results in the literature and implement methods that can improve the unified scaling relation. We provide detailed justifications for our choices of parameters and methods in constructing the unified scaling relation. By the end of this chapter, we will have a scaling relation that can be used for galaxies of all morphologies and we will also see its limitations in terms of mass range as well as its potential for diversifying observing targets in large-scale astronomical surveys.

In Chapter 4 we present new data from the SHαDE survey (Barat et al. 2020; see also Chapter 2.2), which uses VLT observations to test our findings in Chapter 3. This chapter will present some of the limiting factors affecting the unified scaling relation. We will discuss the drivers behind the observed galaxy kinematics and the meaning and the implication of these drivers for the formation and structure of our target galaxies. We seek alternative methods of constructing the unified scaling relation in order to keep it as inclusive as possible.

In Chapter 5, we show the work we have done in preparation for the planned Taipan survey (da Cunha et al. 2017; see also Chapter 2.3). We outline the workings of the Taipan survey data reduction pipeline (TLDR). We present the design and workflow, show the outcomes and current performance of the pipeline, and list the future work that needs to be carried out for the pipeline to ensure optimum performance.

In Chapter 6 we summarise the findings of this thesis and draw broad conclusions regarding the characteristics and properties of unified galaxy scaling relations. We discuss potential directions for the field and future project that would further improve our understanding of the unified galaxy scaling relation.

Chapter 2

Surveys

Obtaining a comprehensive understanding of the internal dynamics of galaxies has been a long-standing challenge. In this thesis we investigate galaxy dynamics at an industrial scale with galaxy surveys. Large-scale galaxy surveys have proven to be extremely useful in understanding galaxy populations, environment, and evolution. The optical spectra we have collected over the years have provided us with galaxy properties such as stellar ages, star formation rates (SFR), metallicity of gas and stars, and overall velocity dispersions, as well as insights about the active galactic nuclei. With the advance of technology, such as high-throughput optical fibres and robotic fibre positioning, optical spectroscopy surveys have become very efficient and are capable of returning high-quality data with unprecedented efficiencies. Large quantities of galaxy spectra are being measured and publicly released every year. This enables us to obtain a better grasp on galaxy populations as classes, to understand the effect of environment on individual galaxies, and to see the interactions between merging galaxies.

However, optical spectroscopy surveys have their own limitations. Single-fibre spectroscopy surveys are limited to providing only a single spectrum within a fixed fibre aperture at the approximate centre of each galaxy. This presents multiple challenges to astronomers studying the internal structures, distribution of matter, and other areas of study that require capturing spatial information. A galaxy's light profile, kinematic profile, stellar and gas distributions cannot be extrapolated from the integrated central information alone. Spatial information is also important for dynamical modelling of galaxies to break the degeneracy between mass, anisotropy, and intrinsic shape in galaxies. These requirements presented a need for a revolutionary technology to make available *two-dimensional* (integral field) spectroscopy of stars and gas for understanding their structure and evolution.

Measuring spatially-resolved information in galaxies has been enabled by the use of Integral Field Units (IFUs). IFUs added a whole new dimension to galaxy kinematic and evolution studies. For the first time, astronomers can examine a large area of the galaxy, or even its entirety, across all wavelengths with some spatial resolution. Some examples of the uses of such information include: star formation distributions; outflows from central active galactic nuclei (AGN); stellar population and metallicity gradients of galaxies; the measurement of stellar angular momentum; and velocity dispersion profiles. The pioneering IFS surveys such as the ATLAS^{3D} survey (Cappellari et al. 2011) using the SAURON IFU instrument (Bacon et al. 2001), and the Calar Alto Legacy Integral Field Area (CALIFA) survey using the Potsdam Multi-Aperture Spectrograph (PMAS) (Sánchez et al. 2012), have provided us with on order of 1000 galaxies in total. From these galaxy samples, despite their modest size and strong selection biases, much has been learnt about the formation and evolution of galaxies[1] (see Sánchez 2020, for a recent review).

Nowadays, the availability of high-quality IFS data has been massively increased by surveys such as the SAMI survey (Green et al. 2018; Scott et al. 2018), with its full sample of ∼3400 targets shortly to be released (Croom et al., in prep.), and the Mapping Nearby Galaxies at Apache Point (MaNGA) survey, with its aim of observing 10,000 galaxies (Bundy et al. 2015; Aguado et al. 2019). Each of CALIFA, SAMI and

---

[1] See http://www-astro.physics.ox.ac.uk/atlas3d/ for a full list of pulications from the ATLAS^{3D} survey and https://califa.caha.es/?q=content/publications from the CALIFA survey.

MaNGA has different advantages and limitations. The CALIFA survey provides the highest physical spatial resolution (0.3-1.5 kpc) and most extended galaxy coverage ($> 2R_e$); the MaNGA survey offers the widest wavelength coverage (3600-10300 Å) and the largest sample size (and so the most reliable galaxy statistics); while the SAMI survey has the highest spectral resolution (28 $\mathrm{km\,s^{-1}}$ in the red arm), providing the most accurate kinematic measurements (particularly for the gas component in galaxies), as well as sampling galaxies from the highest density regions in clusters. More detailed comparison of the various IFS galaxy surveys can be found in Sánchez (2020).

Using IFUs, integral field spectroscopy (IFS) has gained momentum in popularity among the astronomical communities, with new modifications and inventions being pursued to improve IFS for higher efficiency and better quality. This thesis takes advantage of the currently-available IFU instruments and IFS surveys to study unified galaxy scaling relations.

2.1 SAMI

Until a decade ago, performing large-scale IFS surveys was challenging due to the limited availability of the technology. A major step forward for IFS surveys was achieved with the growing availability of multi-IFU instruments capable of taking IFS observations for multiple targets simultaneously. One of the first fibre-based instruments of this kind was the Fibre Large Array Multi Element Spectrograph (FLAMES, Pasquini et al. 2002) on the 8m Very Large Telescope (VLT). In multiplex mode, FLAMES has 15 deployable IFUs of 20 spaxels (spatial elements), each with a 2×3 arcsec^2 field of view (Gillingham et al. 2004). Although the field of view of each FLAMES IFU is small, its overall efficiency (due to its multiplex advantage) has proven valuable for studies of galaxies at intermediate redshifts (e.g. D’Eugenio et al. 2013).

For galaxies in the local universe, IFUs with field of view larger than 2×3 arcsec^2 are essential to provide useful coverage. The SAMI instrument (Croom et al. 2012) on the 3.9m Anglo-Australian Telescope (AAT) was the first instrument with this capability, achieved using the 'hexabundle' fused-fibre-bundle technology (Bland-Hawthorn et al. 2011; Bryant et al. 2011). SAMI combines advantages from efficient IFUs, moderate multiplex, and a large accessible field to allow high efficiency, wide spatial coverage observations of local galaxies. SAMI has 13 IFU fibre bundles, each of which has a field of view approximately 15 arcsec in diameter, consisting of 61 high-performance optical fibres fused together to give a ∼75% filling factor. Spectra from the SAMI instrument are fed into the AAOmega spectrograph at the AAT (Sharp et al. 2006). Using AAOmega, SAMI observes over two bands across the visible spectrum: the blue band covers wavelengths 3700–5700 Å with resolution $R \sim 1700$, while the red band covers wavelengths 6300–7400 Å with resolution $R \sim 4500$. These spectral resolutions correspond to velocity dispersions of $70.4\,\mathrm{km\,s^{-1}}$ in the blue and $29.6\,\mathrm{km\,s^{-1}}$ in the red. This configuration allows SAMI to cover important spectral lines (e.g. Ca H+K, Hβ, [OIII], Hα etc.) over a reasonable redshift range while still maintaining a high spectral resolution.

The SAMI survey target galaxies consist of two main samples. Most SAMI targets are selected from the Galaxy And Mass Assembly (GAMA) survey (Driver et al. 2011). Choosing targets from GAMA offers a wealth of ancillary data that complements the observations from the SAMI survey. The SAMI galaxies selected from the GAMA survey form a series of volume-limited samples, each of which is complete to a specified stellar mass limit over a given redshift range (see Figure 1 in Allen et al. 2015). To supplement this field sample, the SAMI survey also observed mass-selected, volume-limited samples of cluster galaxies around eight massive galaxy clusters. The stellar mass of SAMI galaxy targets are estimated using their rest frame i-band absolute magnitude and $g - i$ colour following the procedure described by Taylor et al. (2011), under the assumption of a Chabrier (2003) stellar initial mass function (IMF) and exponentially declining star formation histories.

The SAMI observations began in March 2013 and were completed in May 2018 May over a total of 250 observing nights on the AAT. The survey resulted in data for just over 3000 galaxies, making it the largest sample of IFU observations of galaxies available at the time (although the MaNGA survey has since surpassed this total). For the analyses in this thesis, we make use of version 0.10 of the SAMI internal data release.

2.2 SHαDE

The SAMI galaxy survey has shed new light on the kinematics of local galaxies of all morphologies. However, due to insufficient spatial and spectral resolution, as well as the lower mass limit of the SAMI target sample, there remain questions relating to low-mass and dwarf galaxies that SAMI data is not capable of addressing.

To complement the SAMI galaxy survey with low-mass ($M_\star < 10^8 M_\odot$) dwarf galaxies, we designed the Study of Hα from Dwarf Emissions (SHαDE). The complete details of this survey are included in this thesis in Chapter 4 and in Barat et al. (2020). Here we briefly summarise the survey motivations and their impact on the instrument and sample selection.

The SHαDE survey uses the FLAMES instrument at the European Southern Observatory's 8m Very Large Telescope (VLT). With a preference for a large field of view and high spectral resolution, SHαDE uses the ARGUS monolithic IFU (rather than the small IFUs provided by OzPoz) and the GIRAFFE optical spectrograph. The ARGUS IFU has a field of view of $11.4 \times 7.3\,\mathrm{arcsec}^2$, comparable to that of a single SAMI IFU hexabundle. SHαDE uses the low resolution[1] setup of the GIRAFFE spectro-

---

[1] Low resolution by stellar astrophysics standards.

graph, with wavelength coverage of 6440–7160 Å at a spectral resolution of $R \sim 13500$, more than 3 times the spectral resolution of SAMI. This allows SHαDE to observe Hα emission from dwarf galaxies for redshifts $z \lesssim 0.08$ with dispersions as low as $9\,\mathrm{km\,s^{-1}}$. SHαDE was carried out in the months of June and August 2018. In a total of 6 nights, 69 galaxies were observed, 20 of which were chosen from the SAMI sample to act as a comparison and control sample, and the remainder chosen from the SDSS survey for their existing ancillary data. The SHαDE sample covers a stellar mass range $10^6\,M_\odot < M_\star < 10^9\,M_\odot$. The combined SH$\alpha$DE + SAMI sample spans a mass range of 10^6–$10^{12}\,M_\odot$. This long baseline in stellar mass provides an excellent sample to study the relation between stellar mass and other properties of galaxies.

2.3 Taipan

While we have seen the advantages and benefits of IFS surveys in previous sections, the results obtained from these surveys can be applied to enhance large-scale single-fibre spectroscopy surveys, as we will see in chapter 4. Single-fibre spectroscopy surveys can typically observe ∼10–100 times more galaxies than IFS surveys (e.g. 13 from SAMI versus ∼ 400 from the 2dF instrument, both using the AAOmega spectrograph at the AAT) simultaneously. Characterising the connection between IFS kinematics and single-aperture kinematics enables us to extrapolate the scientific findings from IFS surveys (consisting of up to a few thousands of galaxies) to single-fibre spectroscopic surveys (with millions of galaxies). One example of this is applying our findings from IFS survey scaling relations to single-aperture surveys, and the planned Taipan galaxy survey (da Cunha et al. 2017) provides a suitable testing ground.

Taipan is planned as a multi-object spectroscopy survey at the United Kingdom Schmidt Telescope (UKST) that aims to cover 2π steradians over the southern sky ($\delta \lesssim 10°$, $|b| \gtrsim 10°$) and obtain optical spectra for about two million galaxies out to $z < 0.4$. Taipan will achieve its high efficiency by taking advantage of the newly-developed Starbug fibre positioning technology (Brown et al. 2014). Starbugs are optical fibres held onto a curved glass plate at the focal surface of the telescope. Taipan uses the purpose-built TAIPAN spectrograph, which covers 3700–5920 Å in the blue band with spectral resolution of $R \sim 1960$ and 5800–8700,Å in the red band with spectral resolution of $R \sim 2740$. This enables us to measure velocity dispersions down to at least 70 $\mathrm{km\,s^{-1}}$.

The Taipan survey has multiple scientific goals, ranging from measuring the local Hubble parameter ($\mathrm{H_0}$) to testing models of gravity. For this thesis, we focus on the Taipan goal of mapping the density and velocity fields in the local Universe. In order to construct a detailed map of the velocity field, one needs to first obtain the peculiar velocities of the galaxies. The peculiar velocity is the deviation of each galaxy from the flow of the Hubble expansion. It is defined as:

$$v_{\mathrm{pec}} \approx cz - H_0 D, \tag{2.1}$$

where cz is the redshift in $\mathrm{km\,s^{-1}}$, H_0 is the local Hubble parameter in $\mathrm{km\,s^{-1}\,Mpc^{-1}}$, and D is the distance in $\mathrm{Mpc^{-1}}$. It is apparent that in order to obtain the peculiar velocity a reliable distance measurement is necessary.

Given the sample size of 2 million galaxies and the varying target properties of the survey, Taipan relies on the Fundamental Plane relation to measure the distances in bulk. The Fundamental Plane (FP), introduced in the previous chapter with Equation 1.2, has proven to be a useful tool in estimating galaxy distances. The 6dFGS peculiar velocity survey was the previous attempt to gather a large set of homogeneous FP-based peculiar velocities over the whole southern hemisphere (Campbell et al. 2014). It generated distances for ~9000 galaxies with an average uncertainty in distance of 26% per galaxy. With the Taipan survey, FP distances will be measured for up to 100,000 galaxies with a target precision of 20% per galaxy. In addition, recent results from Aquino-Ortíz et al. (2020) have shown that, with IFS observations, galaxies of all morphologies can be brought onto the same FP relation. This combination of studying galaxy scaling relation from IFS surveys and applying the results to single-fibre observations holds great potential for the Taipan survey if it permits a generalised form of the FP relation to be applied to a larger fraction of the galaxies in the survey sample.

The kinematic parameters for Taipan sample galaxies will be obtained by using the Taipan Live Data Reduction pipeline (TLDR). This program, which is also part of this thesis, brings together a suite of existing programs to perform data acquisition, data reduction, calibration, scientific quantity extractions, and data management and archiving, all in a fully automated fashion. TLDR will ensure Taipan survey data is of high quality and available in an analysis-ready format.

Unfortunately, due to delays in completing and commissioning the TAIPAN instrument, actual Taipan survey data was not available for this thesis. We therefore use simulated data to demonstrate the operation of TLDR and validate the basic functions of the pipeline.

Chapter 3

The SAMI Galaxy Survey: mass-kinematics scaling relations

This chapter is published in Monthly Notices of the Royal Astronomical Society as: The SAMI Galaxy Survey: mass-kinematics scaling relations. **Barat, Dilyar,** et al, 2019, MNRAS, 487, 2924.

3.1 Abstract

We use data from the Sydney-AAO Multi-object Integral-field spectroscopy (SAMI) Galaxy Survey to study the dynamical scaling relation between galaxy stellar mass $M_\star$ and the general kinematic parameter $S_K = \sqrt{KV_{rot}^2 + \sigma^2}$ that combines rotation velocity V_{rot} and velocity dispersion σ. We show that the $\log M_\star - \log S_K$ relation: (1) is linear above limits set by properties of the samples and observations; (2) has slightly different slope when derived from stellar or gas kinematic measurements; (3) applies to both early-type and late-type galaxies and has smaller scatter than either the Tully-Fisher relation ($\log M_\star - \log V_{rot}$) for late types or the Faber-Jackson relation ($\log M_\star - \log \sigma$) for early types; and (4) has scatter that is only weakly sensitive to the value

of K, with minimum scatter for K in the range 0.4 and 0.7. We compare S_K to the aperture second moment (the 'aperture velocity dispersion') measured from the integrated spectrum within a 3-arcsecond radius aperture ($\sigma_{3''}$). We find that while S_K and $\sigma_{3''}$ are in general tightly correlated, the $\log M_\star - \log S_K$ relation has less scatter than the $\log M_\star - \log \sigma_{3''}$ relation.

3.2 Introduction

Galaxy scaling relations correlate observable quantities of galaxies and capture trends among physical properties. These properties can include galaxy stellar mass ($M_\star$), half-light radius (R_e), rotation velocity (V_{rot}), velocity dispersion (σ), luminosity (L), surface brightness (Σ) and other measurable quantities (McGaugh et al. 2000; Pizagno et al. 2005; Courteau et al. 2007; Avila-Reese et al. 2008; Catinella et al. 2012). For example, the Faber-Jackson relation (FJ; Faber & Jackson 1976) connects σ and L while the Kormendy relation (Kormendy 1977) links Σ and R_e.

Galaxy scaling relations are convenient in predicting physical galaxy properties because they do not require analytic modelling of a galaxy's internal dynamics. Using scaling relations to estimate quantities such as distance and mass is efficient when the sample size is too large to obtain detailed observations or to perform individual analyses.

Scaling relations such as the FJ and Kormendy relations have significant intrinsic scatter that impacts the precision of their predictions. Sample pruning and target selection are necessary to produce tight relations. For morphologically defined classes of galaxies, the Tully-Fisher (TF; Tully & Fisher 1977) relation provides a tight relation between L and V_{rot} for disk-dominated galaxies and the Fundamental Plane relation (FP; Dressler et al. 1987; Djorgovski & Davis 1987) tightly relates R_e, σ and Σ for bulge-dominated galaxies.

Galaxy scaling relations reflect physical mechanisms at work within galaxies. They enable us to gain deeper understanding of galaxy structure, formation and evolution. For example, Kassin et al. (2012) examined V_{rot}/σ across redshift and found that galaxies accrete baryons faster earlier in their life-cycles, but that as galaxies evolve their accretion rate and gas content decrease; Obreschkow & Glazebrook (2014a) demonstrated that the scaling relation between baryon angular momentum (j), stellar mass ($M_\star$) and bulge fraction (β) of spiral galaxies (Peebles 1969; Fall 1983), can produce and explain the FP (and FJ) scaling relation; Lagos et al. (2017), using cosmological simulations, later confirmed the correlation between galaxy mass and specific angular momentum, and the evolution of the $M_\star - j$ scaling relation in passive and active galaxies. Kinematic scaling relations are also useful in the study of the dark matter content of galaxies. For example, Desmond (2017) used the FP to predict the amount of dark matter in the central regions of elliptical galaxies and suggested the deviation of the FP from the virial prediction (also known as the tilt of the FP) can be explained by non-homology in galaxy structure and variations in mass-to-light ratios; Ouellette et al. (2017) also found that the tilt of the FP correlates with the dark matter fraction of each galaxy.

The TF relation applies to disk-dominated galaxies (Bloom et al. 2017a) while the FJ and FP relations apply to spheroidal galaxies. Incorporating galaxies of other morphologies into these scaling relations not only increases the scatter, but also changes the slopes and intercepts of the relations (e.g. Neistein et al. 1999; Iodice et al. 2003; Williams et al. 2010; Tonini et al. 2014), consequently reducing the accuracy and reliability of the quantities derived.

The scatter around the stellar mass versions of the FJ and TF relations can be reduced by replacing the rotation velocity or velocity dispersion, respectively, with the

S_K parameter introduced by Weiner et al. (2006):

$$S_K = \sqrt{KV_{rot}^2 + \sigma^2} \tag{3.1}$$

where K is a constant, commonly taken to be 0.5 (e.g. Weiner et al. 2006, Kassin et al. 2007, Covington et al. 2010, Kassin et al. 2012, Cortese et al. 2014 (hereafter: C14), Simons et al. 2015, Straatman et al. 2017, Aquino-Ortíz et al. 2018 (hereafter: A18)). By combining V_{rot} and σ, S_K provides a common scaling relation for both early-type galaxies and late-type galaxies (Kassin et al. 2007). Furthermore, C14, using data from the Sydney-AAO-Multi-object IFS (Integral Field Spectroscopy) Galaxy Survey (hereafter SAMI Survey; Croom et al. 2012; Bryant et al. 2015) early data release, and A18, using data from the Calar Alto Legacy Integral Field Area survey (CALIFA; Sánchez et al. 2013), showed that S_K can bring together the gas and stellar kinematic measurements of galaxies of all morphologies onto a single dynamical scaling relation. Numerical simulation has shown S_K is minimally affected by the blurring effect due to seeing (Covington et al. 2010). Therefore, S_K is promising in the construction of a unified galaxy scaling relation that is robust with respect to morphologies and sub-optimal observing conditions.

While S_K has been a popular kinematic estimator and mass proxy, there are still a number of outstanding issues: (i) while K is commonly taken to be 0.5, this value has not been quantitatively justified; (ii) C14 found a non-linearity in the $\log M_\star$–$\log S_K$ relation below a stellar mass of $\sim 10^{10} M_\odot$, but the existence and location of this change in slope (which determines the limit of validity for the scaling relation in low-mass galaxies) has not been reliably determined; and (iii) there remains the question of how S_K relates to aperture velocity dispersion (σ_{ap}) from single-fibre surveys.

We use the latest data release from the SAMI Survey to expand on the work of C14, and explore various aspects of the $\log M_\star$–$\log S_K$ scaling relation. Our work is structured as follows. In Section 3.3, we describe the data reduction, kinematic measurements, and sample morphologies. In Section 3.4, we construct S_K from the gas and stellar measurements of our sample; compare S_K to aperture velocity dispersion ($\sigma_{3''}$) measurements; and explore the sensitivity of the scatter of the relation for different values of K. In Section 3.5, we compare our results to observations in the literature and discuss factors that influence the value of K. In Section 3.6 we summarise our findings. We assume throughout a ΛCDM cosmology with $\Omega_M = 0.3$, $\Omega_\lambda = 0.7$ and $H_0 = 70\ \mathrm{km\,s^{-1}Mpc^{-1}}$.

3.3 Data and methods

The SAMI Survey uses the AAOmega dual-beam spectrograph on the Anglo-Australian Telescope at Siding Spring Observatory (Sharp et al. 2006). SAMI obtains integral field spectra by using 13 fused-fibre hexabundles, each containing 61 fibres (Bland-Hawthorn et al. 2011; Bryant et al. 2014). The SAMI spectra cover the wavelength range 3750–5750 Å at a resolution of $R \approx 1800$, and 6300–7400 Å at a resolution of $R \approx 4300$ (Scott et al. 2018). These give dispersion resolutions $\sigma_{\rm res}$ of 70 $\mathrm{km\,s^{-1}}$ in the blue arm where we obtain the stellar kinematics, and 30 $\mathrm{km\,s^{-1}}$ in the red for gas kinematics.

The SAMI Survey includes both field and cluster galaxies (Owers et al. 2017) with redshifts $0.004 < z < 0.095$, r-band Petrosian magnitudes $r_{\rm pet} < 19.4$, and stellar masses 10^7–$10^{12} M_\odot$. The stellar masses of SAMI galaxies are estimated as (Bryant et al. 2015):

$$\begin{aligned}\log(M_\star/M_\odot) = &-0.4i + 0.4D - \log(1+z)\\ &+ (1.2117 - 0.5893z)\\ &+ (0.7106 - 0.1467z) \times (g - i)\end{aligned}$$

where $M_\star$ is the stellar mass in solar mass units, D is the distance modulus, i is the rest frame i-band apparent magnitude, and $g-i$ is the rest-frame colour of the galaxy, corrected for Milky-Way extinction (Bryant et al. 2015). More on the SAMI Survey and instrument can be found in Croom et al. (2012).

3.3.1 Data reduction and sample

SAMI data reduction consists of two stages, reducing raw data to row stacked spectra (RSS) using *2dfdr*[1] and data cube construction from the RSS using the *SAMI Python* package (Allen et al. 2014). The details of the data reduction and data cubing processes can be found in Allen et al. (2015), Sharp et al. (2015), and Scott et al. (2018).

We used gas and stellar kinematic maps extracted from SAMI internal data release v0.10 data cubes. For the stars, the velocity and velocity dispersion maps are measured using the penalised Pixel Fitting method (pPXF; Cappellari & Emsellem 2004). pPXF extracts the stellar line-of-sight velocity distribution (LOVSD) in each spatial pixel (spaxel) from the observed spaxel spectrum assuming a Gaussian form:

$$\mathcal{L}(v) = \frac{e^{-y^2/2}}{\sigma\sqrt{2\pi}} \tag{3.2}$$

where $y = (v - V)/\sigma$. The (V, σ) parameters of this model can be retrieved using a maximum likelihood optimisation. More details of the fitting routine can be found in van de Sande et al. (2017). At the time of this writing, the stellar kinematic data sample includes 2720 galaxies, all of which have also been fitted by the LZIFU (Ho et al. 2014) routine for $H\alpha$ emission line detection and measurement of the velocity and dispersion of the gas component using the one-component fit results.

Using the extracted SAMI stellar and gas kinematic maps, we select the spaxels as follows. First, spaxels are collected within an elliptical aperture with a semi-major axis of one effective radius. For all SAMI galaxies, their semi-major axis, position angles

---

[1] https://www.aao.gov.au/science/software/2dfdr

and ellipticity are determined using Multi-Gaussian Expansion (MGE, Emsellem et al. 1994) fitting to r-band images from either the VLT Survey Telescope (VST) ATLAS (Shanks et al. 2015; Owers et al. 2017) survey or the Sloan Digital Sky Survey (SDSS). Contrary to C14 and A18, where spaxels are selected based on the absolute errors in velocity and velocity dispersion, we do not perform spaxel-level quality cuts other than requiring galaxies to have more than 5 spaxels within the aperture while rejecting empty spaxels. Instead, we perform an overall relative error cut on the kinematic parameter being investigated, only keeping galaxies with relative kinematic error less than 5–10%. Rotation velocity, velocity dispersion, S_K and associated error calculations are described in the next section. However, for comparison, we also produced scaling relations with similar quality criteria at the spaxel level, using only spaxels with velocity error $\Delta V_i < 20\ \mathrm{km\,s^{-1}}$, velocity dispersion error $\Delta\sigma_i < 0.1\sigma + 25$ (van de Sande et al. 2017), on top of the 5% error cut on the final kinematic quantities. Details are shown in section 3.4.3.

Depending on the kinematic parameter to be studied and the selection criteria, our parent sample of 2720 galaxies is divided into 5 sample groups (groups A–E). The selection criteria and sample group descriptions are listed in Table 3.1. For investigation of the $\log M_\star$–$\log S_K$ scaling relation we used sample B. Sample B includes gas-kinematics measurements for 1256 galaxies, stellar-kinematics measurements for 1574 galaxies, and 904 galaxies have both gas and stellar measurements. Galaxies in sample B have a median of ∼70 spaxels. The stellar mass histogram in Figure 3.1a shows that sample B is relatively complete in the high-mass ($\geq 10^{10} M_\odot$) range, but with sufficient numbers of galaxies in the low-mass range to constrain a scaling relation.

3.3.2 Galaxy kinematics

To calculate the rotation velocities of the gas and the stars, we use the velocity histogram technique, following Catinella et al. (2005) and C14. The histogram technique

(1) Sample	(2) Selection criteria for each galaxy	(3) Number of galaxies with gas/stellar measurements	(4) All have both gas and stellar measurements?	(5) Used in Figure(s)
A	All of V_{rot}, σ, $S_{0.5}$ must have less than 5% error for each galaxy	410/270	False	3.2
B	$S_{0.5}$ has error less than 5%	1256/1574	False	3.1 3.3
B1	$\Delta V_i < 20\ \mathrm{km\,s^{-1}}$, $\Delta\sigma_i < 0.1\sigma + 25\ \mathrm{km\,s^{-1}}$ $S_{0.5}$ has error less than 5%	859/839	False	3.4
C	Measurements for gas and stellar kinematics have error less than 5%	223/223 (V_{rot}) 961/961 (σ) 904/904 ($S_{0.5}$)	True True True	3.5
D	Both $S_{0.5}$ and $\sigma_{3''}$ have error less than 5%	864/1141	False	3.6 3.7
E	Both V_{rot} and σ for both gas and stellar measurements have error less than 10%	410/410 (ETG) 232/232 (LTG) 737/737 (All types)	True True True	3.8

Table 3.1: Sample selection criteria and description. All samples had the additional criterion of minor-to-major axis ratio less than 0.95.

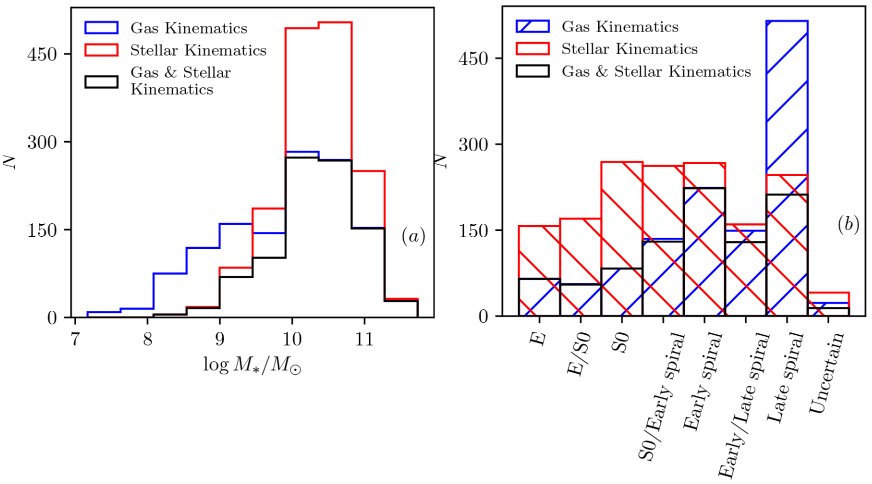

Figure 3.1: Panel (a) shows the mass distributions of sample B with various kinematic measurements available: red represents galaxies with stellar kinematics, blue represents galaxies with gas kinematics, and black represents galaxies with both gas and stellar kinematics. Panel (b) shows the visual morphology distribution of sample B: red bars represent galaxies with stellar kinematics, blue bars represent galaxies with gas kinematics, and black bars represent galaxies with both gas and stellar kinematics.

is simple to implement and, in the process of calculating the velocity width, the Hubble velocity and peculiar velocity of the system naturally cancel. We calculate the velocity width W between the 90th and 10th percentile points of the histogram of spaxel velocities within one r-band effective radius (r_e) elliptical aperture. Then we perform redshift (z) and inclination (i) corrections using an inclination angle estimated from the r-band minor-to-major axis ratio (b/a) which is obtained from the MGE fit to VST and SDSS images. We do not perform luminosity weighting on the rotation velocity. The rotation velocity is calculated as:

$$V_{rot} = \frac{W}{2\ \sin i\ (1+z)} \tag{3.3}$$

where the inclination of a galaxy is calculated as

$$\cos(i) = \sqrt{\frac{(b/a)^2 - q_0^2}{1 - q_0^2}} \tag{3.4}$$

and q_0 is the intrinsic axis ratio assumed to be 0.2. (Catinella et al. 2012). For edge-on galaxies with axis ratio less than 0.2, we do not perform inclination correction. We removed ∼60 galaxies that had axis ratio more than 0.95. We chose to retain edge-on as well as near face-on galaxies in our sample, because one of the main purposes of the study is to find a relation that is as inclusive as possible, without introducing a significant amount of outliers. We explored different sample constraints and found that $b/a > 0.95$ was a reasonable compromise, excluding galaxies lying significantly far from the scaling relation, while being as inclusive as possible.

The effective velocity dispersion σ of a galaxy is measured as the weighted mean of velocity dispersion measurements of each spaxel within an aperture radius of one effective radius, where the weight is the mean continuum flux:

$$\sigma^2 \equiv \frac{\sum_i L_i \sigma_i^2}{\sum_i L_i} \tag{3.5}$$

We highlight that we do not perform any spaxel-level quality cut here, other than having at least 5 non-empty spaxels. We then calculate $S_{0.5}$ as per Equation 3.1, with $K = 0.5$. We use bootstrapping to calculate the standard deviations of V_{rot}, σ and $S_{0.5}$ to use as uncertainties. The bootstrap method involves randomly sampling the same number of spaxels as the total number of spaxels within the aperture, allowing for repeated selection of spaxels, and calculating V_{rot}, σ and $S_{0.5}$. This step is carried out 1000 times to ensure the random samples represent the parent samples.

3.3.3 Galaxy morphologies

Galaxy morphologies in the SAMI sample vary from elliptical galaxies to late-type spiral and irregular galaxies. All SAMI galaxies are visually classified using the SDSS DR9 (Ahn et al. 2012) RGB images by 12 members of the SAMI team following the classification scheme adopted in Kelvin et al. (2014). Here we briefly summarise the classification scheme. First, judging by the presence/absence of a disk or spiral arms, the classifier determines whether a target is an early-type or late-type galaxy. Then in each class, classifiers visually determine if the galaxy contains a bulge (for late-type galaxies) or a disk (for early-type galaxies). Early-type galaxies with only a bulge, and without any disk component, are identified as elliptical (E) galaxies; early-type galaxies that show both bulge and disk components are identified as lenticular (S0) galaxies. Late-type galaxies all have spiral arms by classification definition; if there is a prominent bulge, they are classified as early-spiral galaxies; if there are only spiral arms without a central bulge, then they are classified as late-spiral or irregular galaxies. Where the SDSS image does not show enough features, or a consensus (>67%) among classifiers is lacking, the galaxy is classified as Uncertain (Cortese et al. 2016). For sample B, where we have the most galaxies for studying the $\log M_{\star}$–$\log S_{0.5}$ relation, their morphology distribution is shown in Figure 3.1b. There are relatively more early-type galaxies (E to S0 classes) in the stellar sample than the gas sample, and more late-type galaxies (early to late spiral classes) in the gas sample than the stellar sample.

Interacting galaxies, such as mergers, are typically removed from galaxy scaling relation studies. However, in our scaling relations, in order to obtain a scaling relation with minimal sample selection, we do not remove interacting galaxies from the main sample (sample B). The impact of merger galaxies is quantified further in section 3.4.2.

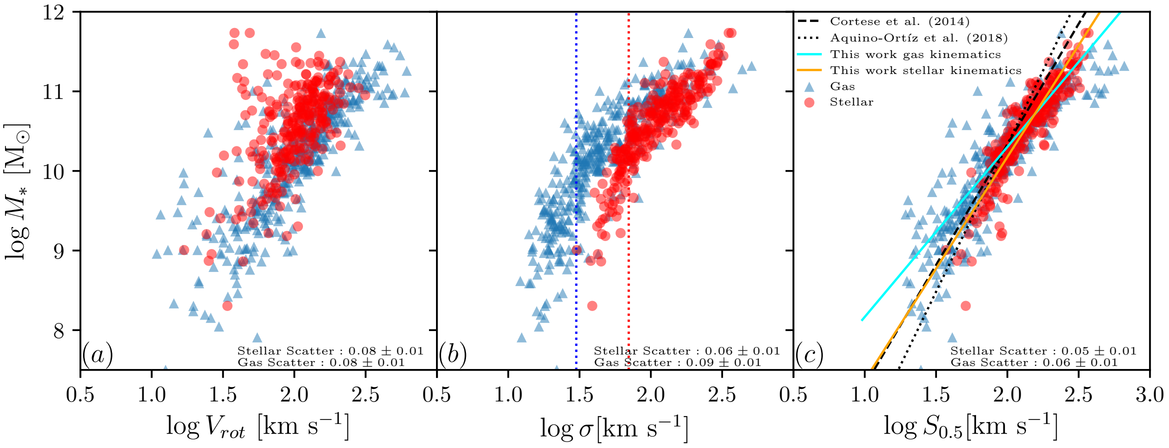

Figure 3.2: SAMI scaling relations from sample A: (a) Tully-Fisher, (b) Faber-Jackson, and (c) generalised $S_{0.5}$ scaling relation. Red dots represent galaxies with stellar measurements, blue triangles represent gas measurements. The observed scatter measured from the median absolute deviation for each scaling relation is annotated in each plot. In panel (b), the red and blue vertical dotted lines represent SAMI spectral resolutions, 70 $\mathrm{km\,s^{-1}}$ and 30 $\mathrm{km\,s^{-1}}$, respectively. In panel (c) the orange solid line is the best fit line to the stellar $\log M_\star$–$\log S_{0.5}$ scaling relation, and the cyan solid line is the best fit line to the gas scaling relation. Relations found by C14 and A18 are included for comparison; they are represented by the black dashed line and black dotted line respectively.

3.4 SAMI scaling relations

3.4.1 $S_{0.5}$ reduces scatter

In this section we demonstrate the advantage of using the $S_{0.5}$ parameter in dynamical scaling relations in contrast to using V_{rot} and σ alone when using IFS data. In both C14 and A18, the $\log M_\star$–$\log S_{0.5}$ scaling relation showed significant reduction in scatter when compared to the TF relation using V_{rot} and FJ relation using σ. For comparison, we perform the same comparison between $S_{0.5}$, V_{rot} and σ using sample A (as described in Table 3.1). In sample A, for each of the gas and stellar kinematic measurements, all of $S_{0.5}$, V_{rot} and σ have less than 5% error for all galaxies. Figure 3.2 shows the correlation of stellar mass ($M_\star$) with V_{rot}, σ, $S_{0.5}$ (i.e. the stellar mass TF, FJ, and combined $S_{0.5}$ scaling relations) as constructed from sample A data. We perform maximum likelihood linear fitting to all the scaling relations in Figure 3.2, and measure their orthogonal median absolute deviations as their scatter. The fitting method is described in more detail in section 3.4.2.1; in this case we fit a simple linear relation with no cut-off. As can be seen from the annotated scatter values in the figure, for both the gas and stellar versions of these scaling relations, the $\log M_\star - \log S_{0.5}$ relation consistently has less scatter than the TF and FJ relations. We also use morphologically-selected samples to compare the TF relation using LTGs, the FJ relation using ETGs, and the $\log M_\star - \log S_{0.5}$ scaling relation using both LTGs and ETGs. $S_{0.5}$ continued to provide the tightest scaling relation.

A caveat here is that our V_{rot} measurements for late-type spiral galaxies do not reach the peak of their rotation curves, hence they cannot accurately trace the potentials of galaxies, and so, in our 'TF' relation, V_{rot} is not as good an estimator of $M_\star$ as $S_{0.5}$. In addition, the inclination estimation obtained from Equation 3.4 assumes axisymmetry in galaxies, with gas discs being in the equatorial plane. This assumption of $q_0 = 0.2$ in fact does not hold true for galaxies of all morphologies; see Weijmans et al. (2014)

and Foster et al. (2017) for alternative cases of q_0 values. It is possible that this choice of q_0 value contributed to the scatter observed in the scaling relations.

The fits from C14 and A18 (from orthogonal fitting of the combined gas and stellar mixed sample) are shown in Figure 3.2c by the dashed line and dotted line respectively. There are small differences between the slopes for our gas and stellar samples, shown in orange and cyan respectively, both with each other and with the linear relations found by C14 and A18. However, given the differences in sample selection, survey systematics, and fitting methods, it is hard to interpret the observed differences in slope as physical differences.

3.4.2 Linearity of the $S_{0.5}$ scaling relation

C14 constructed the gas FJ and $\log M_\star$–$\log S_{0.5}$ scaling relations and observed that the slope became steeper for low-mass ($M_\star < 10^{10} M_\odot$) galaxies. This change in slope is also present in our FJ relation in Figure 3.2b, and the $\log M_\star$–$\log S_{0.5}$ relations in Figure 3.2c. A bend in these kinematic scaling relations is expected, as the fitted linear relations would otherwise predict zero motions for low-mass galaxies ($\sim 10^5 - 10^6 M_\odot$). The cause of the bend will be discussed in more detail in Section 3.5.1, but for now it is crucial to take the bend into consideration in fitting the scaling relation. To locate the change in slope in our $\log M_\star$–$\log S_{0.5}$ scaling relations more precisely, we investigate the scaling relations in detail with sample B in Figure 3.3, where galaxies are selected only based on $\Delta S_{0.5}/S_{0.5} \leq 0.05$.

3.4.2.1 Straight line with a knee

To find the point at which the slope of the relation changes, we hypothesise that there exists a sample limit at position $(S_{0.5,\mathrm{lim}}, M_{\star,\mathrm{lim}})$ where a single linear model can no longer describe the distribution of the sample. For all stellar mass measurements below this $M_{\star,\mathrm{lim}}$ value $S_{0.5}$ values will be normally distributed around a limiting value

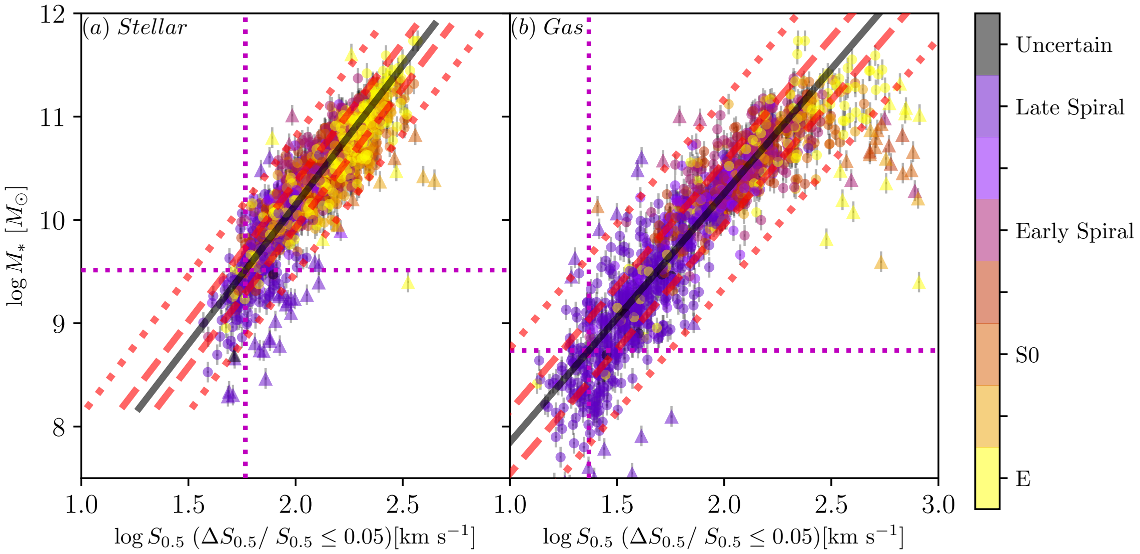

Figure 3.3: SAMI stellar and gas $S_{0.5}$ scaling relations from sample B. The black solid line shows the line of best fit, with fitting parameters shown in Table 3.2. Red dashed and dotted lines show 1 and 3 RMS distance from the line of best fit. Triangular points are galaxies >3 RMS away from the line of best fit, and are excluded from the fitting routine. The magenta vertical and horizontal dotted lines show the location where the distribution of points deviate from a linear relation, which we fit as the sample limit. These limits occur at different $S_{0.5}$ values and different stellar masses for the stellar and gas samples: $S_{0.5,\mathrm{lim,stellar}} = 59\ \mathrm{km\,s^{-1}}$ for the stellar sample, $S_{0.5,\mathrm{lim,gas}} = 23\ \mathrm{km\,s^{-1}}$ for the gas sample.

$S_{0.5,\mathrm{lim}}$. For stellar masses above the $M_{\star,\mathrm{lim}}$ value the scaling relation is assumed to be a linear relation described by:

$$\log S_{0.5} = a \log M_{\star} + b \tag{3.6}$$

We then use this combination of a linear model with a constant limit cut-off in our maximum likelihood fitting routine, assuming $\log M_{\star,i}$ and $\log S_{0.5,i}$ for each galaxy have Gaussian uncertainties $\sigma_{\log M_{\star,i}}$ and $\sigma_{\log S_{0.5,i}}$ respectively. The total posterior logarithmic likelihood $\ln \mathcal{L}$ under this model is

$$\ln \mathcal{L} = \frac{1}{2} \sum_i \left[\ln \frac{a^2+1}{s^2_{\log S_{0.5,i}}} - \frac{(\log S_{0.5,i} - Y)^2}{s^2_{\log S_{0.5,i}}} \right] \tag{3.7}$$

where Y is a linear function above $M_{\star,\mathrm{lim}}$ and a constant below $M_{\star,\mathrm{lim}}$, namely,

$$Y = \begin{cases} a \log M_{\star,i} + b, & M_\star > M_{\star,\mathrm{lim}} \\ a \log M_{\star,\mathrm{lim}} + b, & M_\star \leq M_{\star,\mathrm{lim}} \end{cases} \tag{3.8}$$

and $s^2_{\log S_{0.5,i}} \equiv \sigma^2_{\log S_{0.5}} + \sigma^2_{M_{\star,i}} a^2 + \sigma^2_{\log S_{0.5,i}}$ where $\sigma_{\log S_{0.5}}$ is the intrinsic scatter about the model. By adjusting the fitting parameters a, b, $\sigma_{\log S_{0.5}}$, $\log M_{\star,\mathrm{lim}}$ and using Markov Chain Monte Carlo (MCMC; Foreman-Mackey et al. 2013) we can find the model parameters that maximise the likelihood given by Equation 3.7 together with their uncertainties. To ensure the model is robust against outliers, we repeat the fitting routine five times whilst rejecting points that are $> 3\sigma$ away each time (represented by triangular points in Figure 3.3). The fitting method is described in more detail as the 2D *hyper-fit* in Robotham & Obreschkow (2015).

3.4.2.2 The bends in the scaling relations

Following the fitting method described in the previous section, we fit the linear+cutoff model to our sample B galaxies, as shown in Figure 3.3; the fitted parameters and their uncertainties are given in Table 3.2.

There are 40-50 outliers in our stellar and gas scaling relations, mostly at $\log S_{0.5} \geq 2.5$. In the stellar scaling relation, visual inspection of these galaxies shows them to be contaminated by either foreground stars or (in clusters) nearby bright galaxies. In the gas scaling relations, these galaxies are generally ETGs with relatively larger errors in their gas kinematic measurements. 13 of the outliers in the gas scaling relation are

Sample	Figure	Y	Slope (a)	Intercept (b)	$Y_{\rm lim}$ $[\rm km\,s^{-1}]$	$M_{\star,\rm lim}[M_\odot]$	Scatter ($\rm MAD_{orth}$)
B	3a	$S_{0.5,\rm stellar}$	0.37 ± 0.01	-1.77 ± 0.06	58.3 ± 1.0	$10^{9.56}$	0.048 ± 0.002
	3b	$S_{0.5,\rm gas}$	0.42 ± 0.01	-2.26 ± 0.06	23.0 ± 1.0	$10^{8.62}$	0.070 ± 0.002
B1	4a	$S_{0.5,\rm stellar}$	0.35 ± 0.01	-1.60 ± 0.10	58.3 ± 1.0	$10^{9.62}$	0.041 ± 0.002
	4b	$S_{0.5,\rm gas}$	0.39 ± 0.01	-1.99 ± 0.05	22.4 ± 1.0	$10^{8.56}$	0.063 ± 0.003
D	7a	$S_{0.5,\rm stellar}$	0.36 ± 0.01	-1.59 ± 0.06	67.0 ± 1.2	$10^{9.49}$	0.049 ± 0.001
	7c	$S_{0.5,\rm gas}$	0.40 ± 0.01	-2.16 ± 0.06	22.4 ± 1.0	$10^{8.73}$	0.061 ± 0.002
D	7b	$\sigma_{\rm stellar}$	0.38 ± 0.01	-1.82 ± 0.06	67.4 ± 1.1	$10^{9.61}$	0.068 ± 0.002
	7d	$\sigma_{\rm gas}$	0.48 ± 0.01	-2.98 ± 0.14	26.3 ± 1.1	$10^{9.17}$	0.090 ± 0.004

Table 3.2: Scaling relation fitting results from *hyper-fit*. All scaling relations have the form as described in Equation 3.8.

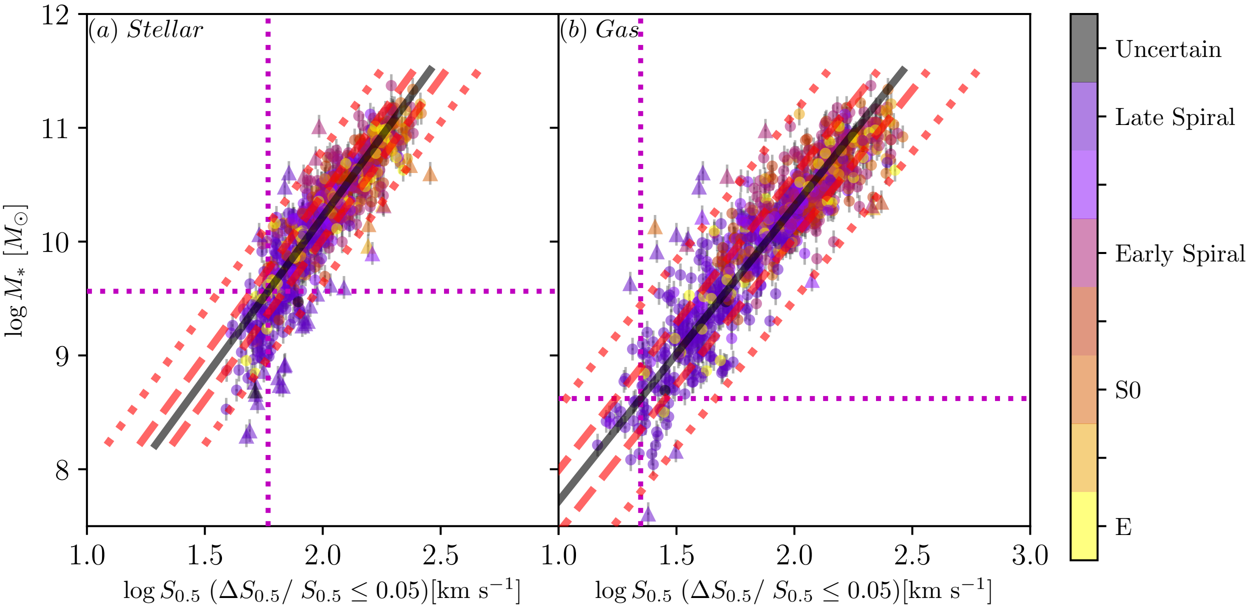

Figure 3.4: SAMI stellar and gas $S_{0.5}$ scaling relations from sample B1. As for Figure 3.3, except that the galaxy kinematics are measured after additional spaxel-level quality cuts as described in Table 3.1; fits are given in Table 3.2.

found to be merger galaxies. Removing these merger galaxies did not change the slope, intercept or the scatter of the scaling relation. All of the outliers disappear when we apply a more stringent quality cut than $\Delta S_{0.5}/S_{0.5} \leq 0.05$.

The fitted $M_{\star,\mathrm{lim}}$ for each of the gas and stellar versions of the scaling relation can be converted to $S_{0.5,\mathrm{lim}}$ using the model. For the stellar version of the scaling relation, the bend occurs at $(M_{\star,\mathrm{lim,stellar}},\ S_{0.5,\mathrm{lim,stellar}}) = (10^{9.6} M_\odot,\ 59\ \ \mathrm{km\,s^{-1}})$, and for the gas version, $(M_{\star,\mathrm{lim,gas}},\ S_{0.5,\mathrm{lim,gas}}) = (10^{8.9}\, M_\odot,\ 23\ \ \mathrm{km\,s^{-1}})$. The fact that the bend in the stellar and gas scaling relations occurs at different stellar mass values suggests the nature of the bend in our scaling relation is unlikely to be a physical phenomenon.

3.4.3 Effect of spaxel-level quality cut

The $\log M_\star - \log S_{0.5}$ scaling relation in our study with sample B is constructed with minimal sample selection as well as minimal quality cut on the spaxels, in order to be as inclusive as possible. This procedure is different from C14 and A18. To investigate the importance of high quality spaxels, we perform a similar spaxel-level cut where we only keep spaxels with velocity error $\Delta V < 20\ \mathrm{km\,s^{-1}}$, velocity dispersion error $\Delta\sigma < 0.1\sigma + 25$, on top of the 5% error cut on the $S_{0.5}$ parameter. The velocity dispersion spaxel selection routine follows van de Sande et al. (2017), which ensures spaxels have $S/N > 3\text{Å}^{-1}$ for $\sigma > 35\ \mathrm{km\,s^{-1}}$. These criteria produce sample B1. Figure 3.4 shows the scaling relations produced with sample B1, and Table 3.2 shows the fitting results.

By introducing spaxel-level quality cuts, the slopes of both stellar and gas scaling relation decreased by 0.02 to 0.03 (i.e. by 2 to 3σ). The scatters of both scaling relations were also reduced significantly. The locations of the sample limits (Y_{lim}, $M_{,\mathrm{lim}}$) remained the same. It is clear that performing spaxel-level quality selection can increase the quality of the scaling relations. However, by applying a spaxel-level quality cut, sample sizes were reduced by 30% to 50%. For our study, it is better to have larger sample sizes than scaling relations with less scatter, as the sample will be divided further in later sections.

3.4.4 Gas and stellar $S_{0.5}$ disagreement

To test whether the $S_{0.5}$ parameters from the stellar and gas kinematics trace the same gravitational potentials, we compare the rotation velocities, velocity dispersions and $S_{0.5}$ measurements of stellar and gas components on a per-galaxy basis with SAMI samples C (as described in Table 3.1). Galaxies in the sample are selected to have both gas and stellar kinematic errors less than 5% for each of V_{rot}, σ and $S_{0.5}$. Figure 3.5a, using sample C, shows that stars in general rotate more slowly than the gas. This is

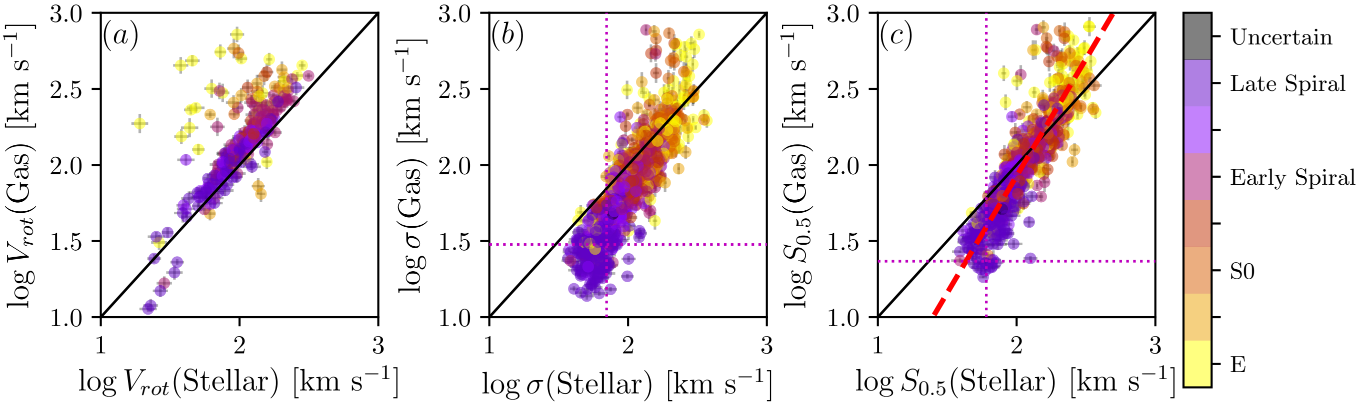

Figure 3.5: Comparison between SAMI sample C gas and stellar measurements of (a) V_{rot}, (b) σ, and (c) $S_{0.5}$. Galaxies are colour-coded by morphology. For visibility, we show 3 standard deviation error bars. Black solid lines in each panel show the one-to-one relation. The red dashed line in panel (c) is the best-fit line to the points. Horizontal and vertical magenta lines in panel (b) show the gas and stellar instrumental dispersions (30 km s^{-1} and 70 km s^{-1} respectively) and in panel (c) show the fitted gas and stellar sample limits (23 km s^{-1} and 59 km s^{-1} respectively).

due to asymmetric drift, where the rotation velocity of the stars is lower than that of the gas because stars have additional pressure support against gravity from a higher dispersion (Binney & Tremaine 2008). The mean ratio between the stellar and gas rotation velocities is $\langle V_{rot,stellar}/V_{rot,gas}\rangle \sim 0.77 \pm 0.29$ which is consistent with the value (∼0.75) obtained by C14.

Using sample C, where both gas and stellar σ measurements have less than 5% error, the offset between the SAMI gas and stellar FJ relations observed in C14 is reflected in our FJ relation. The mean ratio between gas and stellar dispersions is $\langle \sigma_{stellar}/\sigma_{gas}\rangle \sim 1.58 \pm 0.59$, as shown in Figure 3.5b, consistent with the value (∼1.55) found by C14. We note that $\sigma_{stellar} > \sigma_{gas}$ for galaxies with $\log \sigma_{gas} < 2.5$ is expected due to asymmetric drift. There are some elliptical and S0 galaxies with $\log \sigma_{gas} > 2.5$ that lie significantly above the one-to-one line, and there are a few factors that could lead to this deviation. Firstly, these galaxies have low gas abundance, making it harder to obtain accurate σ_{gas} measurements (Lees et al. 1991; Young 2002; Young et al. 2011); secondly, it is possible the gas component in these ETGs could be in a less stable configuration than in LTGs, possibly due to filamentary gas (Kleiner et al. 2017) and shocks (Gaspari et al. 2012; Sil'chenko et al. 2019) leading to higher σ_{gas} uncertainties as shown in Figure 3.5b.

In C14, the gas and stellar $S_{0.5}$ parameters are found to have a mean logarithmic difference (gas − stellar) of −0.02 dex. In our sample C, the logarithmic difference is −0.05 dex. In Figure 3.5c, while the one-to-one line (black) goes through our $S_{0.5,gas} - S_{0.5,stellar}$ distribution, the best-fit (red-dashed) line has a slope of 1.49 ± 0.02, which suggests a systematic disagreement between $S_{0.5,gas}$ and $S_{0.5,stellar}$. One explanation of $S_{0.5,stellar} > S_{0.5,gas}$ for $S_{0.5} < 100\,\mathrm{km\,s^{-1}}$ can be traced to the fact that $\sigma_{stellar} > \sigma_{gas}$. However, inclusion of $V_{rot,gas}$ component where $V_{rot,gas} > V_{rot,stellar}$ does not seem to sufficiently compensate $S_{0.5gas}$ to bring balance between $S_{0.5,stellar}$ and $S_{0.5,gas}$. The scatter in the $S_{0.5,gas} - S_{0.5,stellar}$ correlation increases for galaxies with

$\log S_{0.5,gas} > 2.25$. As in Figure 3.5b, this increase in scatter can be explained by E and S0 galaxies having larger uncertainties in their σ_{gas} measurements. However, in the *hyper-fit* routine, measurements are error-weighted, reducing the impact of points with large errors; moreover, with a tighter uncertainty cut (using galaxies with <2% errors) the slope remained significantly above unity (1.34 ± 0.04). Lastly, restricting the sample to only include galaxies with both gas and stellar measurements above the fitted sample limit, the slope remained steeper than unity at 1.49 ± 0.02. This disagreement between stellar and gas $S_{0.5}$ parameters requires investigation on a per-galaxy basis, especially for lower mass ($\log M_\star < 9.5$) galaxies where $S_{0.5,stellar} > S_{0.5,gas}$. This will be studied in more detail in future.

3.4.5 IFS and aperture kinematic measurements

While IFS data provides resolved spatial information on galaxy kinematics, compared to single fibre observations it is observationally expensive. In order to compare the effect of IFS data on the scaling relations, we constructed aperture spectra from SAMI data cubes within a 3-arcsecond-diameter (SDSS-like) aperture. Applying a 5% error quality cut to the aperture velocity dispersions, we obtained $\sigma_{3'',gas}$ for 864 galaxies, and $\sigma_{3'',stellar}$ for 1141 galaxies; these form sample D (see Table 3.1). Figure 3.6 shows a comparison between average velocity dispersion σ_{1R_e}, $S_{0.5}$ parameter and $\sigma_{3''}$, and their logarithmic difference as a function of $R_e/3''$, the galaxy size relative to the aperture diameter. Galaxies are colour-coded by their $0.5V_{rot}^2/\sigma^2$ ratio to show the balance between V_{rot} and σ within the $S_{0.5}$ parameter, galaxies with $0.5V_{rot}^2/\sigma^2$ ratio above and below the colour bar limits are shown in solid red and solid blue respectively.

For stellar measurements, the kinematics is mostly pressure-supported and dominated by σ_{1R_e}, which is confirmed by 1098 out of 1141 galaxies having $0.5V_{rot}^2/\sigma^2 < 1$. The inset residual plots comparing the residuals to galaxy size indicate that galaxies with $0.5V_{rot}^2/\sigma^2 > 1$ have $R_e > 6''$, and they are furthest away from the one-to-one

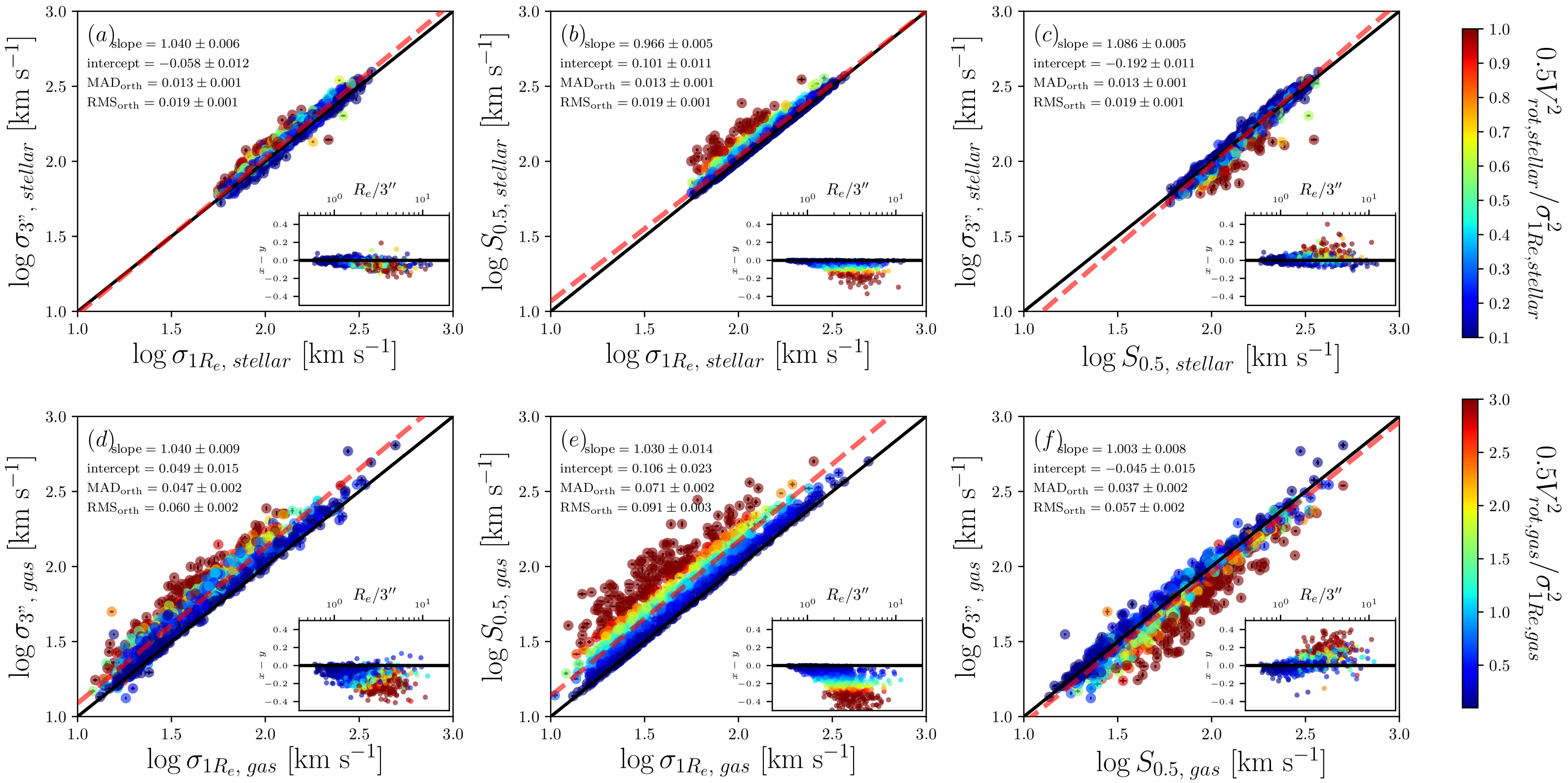

Figure 3.6: Direct comparison, using sample D, between $S_{0.5}$ and $\sigma_{3''}$ (the 3-arcsecond-diameter aperture velocity dispersion), and average velocity dispersion σ_{1R_e} within $1R_e$ from gas and stellar kinematics. Their differences against apparent galaxy size are plotted in the inset plots. Black solid lines are the one-to-one relations; red dashed lines are the best fits; points are colour coded by $0.5V_{rot}^2/\sigma^2$ to indicate the dominant term in the $S_{0.5}$ parameter.

line in all panels. From panel a, the increasing $0.5V_{rot}^2/\sigma^2$ ratio from the line-of-best-fit confirms that $\sigma_{3''}$ contains a V_{rot} component. Comparing panel a and c, we can see that galaxies with $0.5V_{rot}^2/\sigma^2 > 1$ are affected the most by replacing σ_{1R_e} with $S_{0.5}$. Since these large galaxies with high $0.5V_{rot}^2/\sigma^2 > 1$ ratio make up less than 5% of the sample, the scatter remained the same between $\sigma_{3''} - \sigma_{1R_e}$ and $\sigma_{3''} - S_{0.5}$ comparisons.

The disparity due to the V_{rot} component between σ_{1R_e}, $S_{0.5}$ and $\sigma_{3''}$ is amplified for the gas kinematics, shown in the lower panels of Figure 3.6. Gas has relatively more rotation support than stars; 386 out of 864 galaxies have $0.5V_{rot}^2/\sigma^2 > 1$, which makes up 44% of the sample (for stellar measurements, 4%). The range of $0.5V_{rot}^2/\sigma^2$ values is larger compared to the stellar measurement, as shown by the values on the colour bar.

For both gas and stellar components, comparing $\sigma_{3''}$ to σ_{1R_e} shows that $\sigma_{3''}$ contains additional rotation support. However, by replacing σ_{1R_e} with $S_{0.5}$ (effectively adding a $0.5V_{rot}^2$ component), $S_{0.5}$ for large ($R_e > 6''$) galaxies became significantly larger than their $\sigma_{3''}$ values. This indicates that the rotation velocity component within $\sigma_{3''}$ measurements is weighted less than that within the $S_{0.5}$ parameter. It is clear that if one wishes to match $\sigma_{3''}$ and $S_{0.5}$, the K value in the definition of S must be less than 0.5, but greater than 0. For our particular purpose of constructing scaling relations, we compare $\log M_\star - \log \sigma_{3''}$ and $\log M_\star - \log S_{0.5}$ in the following section.

Even though the $S_{0.5}$ parameter and 3 arcsec aperture velocity dispersion $\sigma_{3''}$ for the gas and the stars cover different parts of galaxies, they remain in broad agreement. This agreement is encouraging because while the $\log M_\star - \log S_{0.5}$ relation applies to galaxies of all morphologies, obtaining the $S_{0.5}$ parameter requires observationally-expensive IFS data, whereas the measuring the velocity dispersion in single-fibre surveys is observationally relatively cheap. The residual plots in Figure 3.6c indicates that $\sigma_{3''}$ is a fairly unbiased predictor of $S_{0.5,stellar}$ out to about $R_e = 3''$ (rather than, as one might have expected, $R_e = 3''/2$); moreover, the scatter only grows relatively gradually beyond $R_e = 3''$, and more slowly for the stellar measurements than for the gas measurements.

3.4.6 Comparing IFS and aperture scaling relations

As both aperture σ and $S_{0.5}$ are used in kinematic scaling relations, we compare variants of the FJ relation using $S_{0.5}$ and $\sigma_{3''}$ in Figure 3.7. For both stellar and gas versions, using the $S_{0.5}$ parameter consistently provides tighter relations with less scatter than using $\sigma_{3''}$ (see Table 3.2). This confirms that $S_{0.5}$ is a better mass proxy than single-aperture velocity dispersion, and suggests the promising possibility of using $S_{0.5}$ to reduce the scatter in other scaling relations such as the FP relation (e.g. Graham et al. 2017). On the other hand, for many purposes the slight increase in scatter in the scaling relation that results from using the aperture dispersion rather than $S_{0.5}$ (~ 0.02 dex for stars and ~ 0.03 dex for gas) may be an acceptable trade-off for the lower observational cost of single-fibre surveys relative to IFS surveys.

We notice in Figure 3.7 that choosing $S_{0.5}$ over $\sigma_{3''}$ yields more outliers (triangular points, excluded from the fit) that are > 3 RMS (red dotted line) away from the line of best fit (black line). This is due to factors such as inclination errors and individual spaxel quality. IFS sampling radius affects the quality of the $S_{0.5}$ parameter more than single-aperture velocity dispersion measurements. In SAMI $\sigma_{3''}$ measurements, spectra from each spaxel are co-added to form the aperture spectrum, which increases the signal-to-noise ratio, and returns more reliable (albeit less accurate) kinematic measurements.

3.4.7 Varying K

The original S_K parameter introduced by Weiner et al. (2006) combines the galaxy rotation velocity and velocity dispersion in quadrature, weighting the rotation velocity by the factor K. This is commonly taken to be $K = 0.5$, which is correct only for

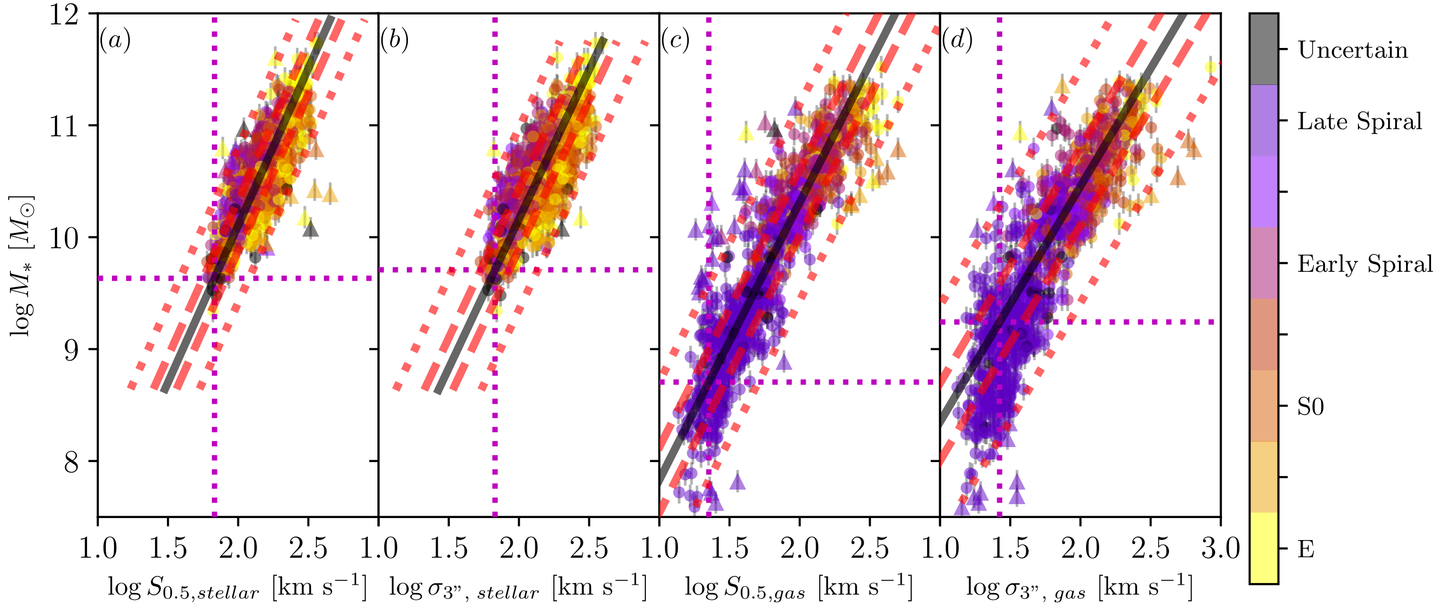

Figure 3.7: Scaling relations constructed from $S_{0.5}$ kinematic parameters and aperture velocity dispersions using sample D. Panels (a), (b), (c) and (d) show scaling relations constructed between stellar mass and, respectively, $S_{0.5,stellar}$, $\sigma_{3'',stellar}$, $S_{0.5,gas}$ and $\sigma_{3'',gas}$ measurements. Black solid lines in each panel are lines of best fit; red dashed and dotted lines define distances 1 RMS and 3 RMS away from the line of best fit. Triangular points are measurements >3 RMS away from the line of best fit, and are excluded from the fit as outliers. Horizontal and vertical magenta dotted lines are the fitted model limits. Fit parameters and uncertainties are given in Table 3.2. For both gas and stellar measurements, $S_{0.5}$ consistently produces scaling relations with less scatter than aperture velocity dispersion.

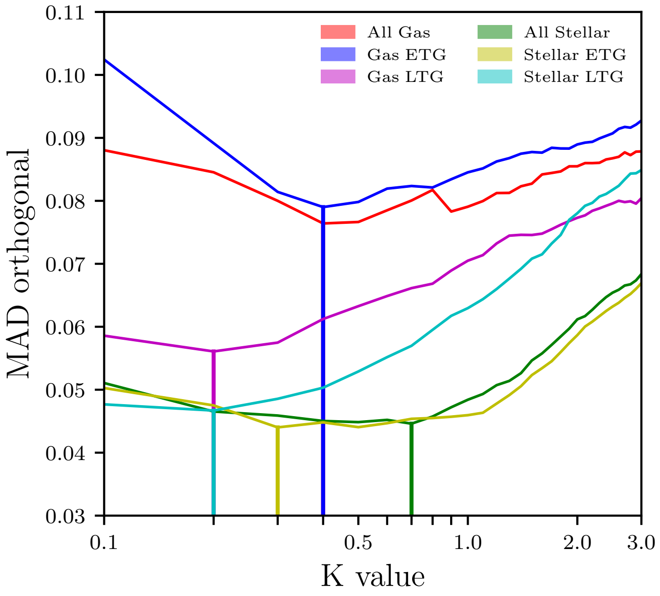

Figure 3.8: Effect of the value of K on the scatter of the SAMI gas and stellar $\log M_\star - \log S_K$ scaling relations. The curves show the scatter about the relation for each colour-coded galaxy sample and the shaded regions show the 1σ uncertainties. The gas and stellar samples are further divided into ETGs and LTGs to determine the effect of morphology. Where $S_{K,gas}$ is used, the full, ETG and LTG samples are colour-coded red, blue and purple respectively; where $S_{K,stellar}$ is used, the full, ETG and LTG samples are colour-coded green, yellow and cyan respectively. The vertical lines show the locations of the minimum scatter for each sample (n.b. the red and blue vertical lines are over-plotted).

virialised systems with spherical symmetry and isotropic velocity dispersion (Kassin et al. 2007). We empirically test the effect of changing the value of K in the construction of the S_K parameter by measuring the scatter about the scaling relations. In this section we use sample E, where each galaxy has both V_{rot} and σ with less than 10% error for both gas and stellar kinematics. We chose 10% error on V_{rot} and σ to provide a statistically large sample for determining the scatter about the scaling relation, though the results are qualitatively unaffected if we use a more stringent sample selection.

We tested K values ranging from 0 to 3 in the $\log M_\star - \log S_K$ scaling relation, and measured the orthogonal median absolute deviation from the scaling relation for

	Gas All	Gas ETG	Gas LTG
Optimal K	0.4	0.4	0.2
$\mathrm{MAD}_{\mathrm{orth}}$	0.076	0.079	0.057
	Stellar All	Stellar ETG	Stellar LTG
Optimal K	0.7	0.3	0.2
$\mathrm{MAD}_{\mathrm{orth}}$	0.045	0.044	0.047

Table 3.3: Values of K that return the minimum scatter for gas and stellar scaling relations, for each morphological sample.

each K value. We performed this test for both the gas and stellar versions of the scaling relation, and for all galaxies as well as separately for early-type (E and S0) and late-type (Sp and Irr) galaxies. We then measured the scatter in the scaling relation at every K value for each of these samples.

Figure 3.8 shows the effect of varying K in the $\log M_\star - \log S_K$ scaling relation for gas and stellar measurements, for both the full sample and for early-type and late-type galaxies; the values of K that return the minimum scatter for each version of the scaling relation are listed in Table 3.3. For the full sample and for early-type galaxies the minimum in the scaling relation scatter is broad and spans approximately $K = 0.3$–0.7. Given the uncertainties in the scatter measurements, shown as shaded regions in Figure 3.8, $K = 0.5$ returns a scatter consistent with the minimum when either ETGs or all galaxies are considered. This consistency justifies the common usage of $K = 0.5$ in the literature and the consistency of analyses when K is varied (e.g. Covington et al. 2010,C14,A18). However, the late-type galaxy scaling relations, whether based on stellar or gas kinematics, have scatter that is minimised over a narrower range around $K = 0.2$, and marginally higher scatter for $K = 0.5$. While this small coefficient for V_{rot} seems counter-intuitive given V_{rot} is the primary component in the TF relation for LTGs, it is apparent that for LTGs their σ component must be taken into consideration. The need for properly including the σ component can be due to effects such as beam-smearing where V_{rot} decreases and σ increases. In the S_K

parameter, σ is up-weighted by down-weighting the V_{rot} component, so that by using the S_K parameter, the effect of beam smearing is minimised. For a broad sample of the galaxy population, the optimum value depends on the mix of morphologies in the sample; the specific factors that lead to this situation are discussed in the following section.

3.5 Discussion

3.5.1 SAMI scaling relations

Using integral field spectroscopy (IFS) from the SAMI Survey for a parent sample of 2720 galaxies, we re-examine the $\log M_\star - \log S_{0.5}$ scaling relation studied in C14. We confirm that the $S_{0.5}$ kinematic parameter, measured from either the stars or the gas, brings galaxies of all morphologies onto a common scaling relation with stellar mass. The slopes of the scaling relation obtained here, both for the stars (0.37 ± 0.01) and for the gas (0.42 ± 0.01), are steeper than that (0.34 ± 0.01) obtained by C14. This difference is likely due to the difference in stellar mass distributions, as our sample is skewed towards higher masses ($M_\star > 10^{10}\,M_\odot$); C14 in fact fitted for galaxies with $M_\star > 10^{10}\,M_\odot$ and found a steeper slope. This difference in slope is slightly decreased when we performed spaxel-level quality cut which eliminated some of most massive galaxies ($M_\star > 10^{11.5} M_\odot$).

C14 also observed a change in slope across a mass range of $8.5 \lesssim \log M_\star/M_\odot \lesssim 11.5$; this apparent change in slope is also present in our sample. C14 suggested this slope change could be due to not accounting for the mass in neutral gas; due to lack of HI data, we are unable to test this hypothesis. However, the change in slope in our $\log M_\star - \log S_{0.5}$ scaling relation could be due to other reasons besides not accounting for the total baryonic mass. Possible causes include: a kinematic measurement limit due to the combined effects of the instrumental resolution and S/N ratio, as a reference we presented the SAMI instrument resolutions for gas and stellar kinematics in Figure 3.2; the uncertainty in the low velocity dispersion measurements positively skewing the distribution of the observed velocity dispersions; a surface brightness limit causing the low-mass sample to be biased towards brighter galaxies with relatively high velocity dispersions; an intrinsic physical effect causing low-mass galaxies to have higher velocity dispersions than expected based on the linear relation for high-mass galaxies. Unfortunately, with the currently available SAMI data and its limitations in S/N ratio, spectral resolution and sample selection, we cannot distinguish all of these possible causes.

However, we fitted a linear scaling relation with a cutoff at a sample limit $M_{\star,\mathrm{lim}}$ (corresponding to $S_{0.5,\mathrm{lim}}$) and found that the sample limits in the stellar and gas versions of the relation occur at different masses. This suggests the bend observed in our sample is unlikely to be caused by intrinsic properties such as stellar mass (this is not to say that there is no physical change in the slope of the scaling relation at some lower mass). A18 suggest galaxies with stellar mass below $\log M_\star/M_\odot \sim 9.5$ have more dark matter content within the effective radius as the mass decreases, so that the dynamical mass (from $S_{0,5}$ estimation) to stellar mass ratio for low mass galaxies increases, resulting in a change in slope in $\log M_\star - \log S_{0.5}$. Unfortunately, while we do have galaxies in our sample with $\log M_\star/M_\odot < 9.5$, the range of low-mass galaxies does not extend down to 10^7–$10^8\,M_\odot$. For future work, high S/N IFS observations of low-mass galaxies with higher spectral resolution ($\sigma_{\mathrm{res}} \sim 10$ km s^{-1}) will be necessary to fully determine the linearity of the stellar scaling relation throughout the $7 \lesssim \log M_\star/M_\odot \lesssim 12$ mass range (e.g. using Hector, Bryant et al. 2016).

3.5.2 IFS and aperture kinematics

In Section 3.4.5 and 3.4.6 we compared measurements of the $S_{0.5}$ parameter and the aperture velocity dispersion and found surprisingly good agreement between the two kinematic tracers (as seen in Figure 3.6). This agreement is interesting because, while both $S_{0.5}$ and $\sigma_{3''}$ are measures of galaxy internal motions, they measure those motions differently. By definition, $\sigma_{3''}$ measures the second moment of the LOSVD integrated over a 3-arcsecond-diameter aperture, including the effect of rotation velocity. For $S_{0.5}$, the σ component is a luminosity-averaged quantity from LOSVD dispersions measured locally over an aperture (here up to $1R_e$). By combining these local dispersion measurements with a global rotation measurement V_{rot} via a suitable scaling factor, $S_{0.5}$ produces tighter scaling relations with $M_\star$ than $\sigma_{3''}$ (as seen in Figure 3.7 and Section 3.4.6).

The extra information provided by IFS and the more complex calculation involved in deriving $S_{0.5}$ thus provide a better understanding of this scaling relation (and others). However, IFS is observationally expensive while fibre surveys are observationally cheap. So for purposes requiring very large samples (e.g. exploring the effect of environment on scaling relations for galaxies of different morphological types or using scaling relations to derive distances and peculiar velocities) aperture dispersions may be a more efficient and economical choice.

3.5.3 The importance of K

The motivation for using $K = 0.5$ in the S_K parameter originates from the virial theorem prediction of the relation between circular velocity and velocity dispersion for an isothermal sphere, $V_{circ} \propto \sqrt{\alpha} \cdot \sigma$, where α is a constant that describes the density profile of the system. We have found empirically that the scatter depends weakly on the value of K, with minimum scatter occurring between $K = 0.2$ and $K = 0.7$.

There are a number of possible factors that can theoretically influence the value of K:

(1) *Solutions to the Jeans equation.* The convention of $K = 0.5$ originates from the

singular sphere case of the Jeans equation, where the circular velocity is given by:

$$V_{circ}^2 = \frac{GM(r)}{r} = -\sigma^2 \frac{d\ln\rho}{d\ln r} \tag{3.9}$$

where ρ and r are the density and radius. For isothermal spheres, $\rho \propto \sigma^2/r^2$, and at large radius $d\ln\rho/d\ln r \sim -2$; therefore $V_{circ}^2 \sim 2\sigma^2$ (Binney & Tremaine 2008, Section 4.3.3b). As we measure V_{rot} via the velocity width technique, $V_{rot}^2 \equiv V_{circ}^2 \sim 2\sigma^2$, so $K = 0.5$ corresponds to equally weighting V_{rot} and σ, which would be optimal if they have similar uncertainties. Note that this conclusion makes assumptions about the galaxy density profile, the radius at which the kinematics are measured, and the relative precision of the V_{rot} and σ measurements—almost no real galaxies or kinematic observations satisfy all these assumptions. Hence we can see when the population is divided into different sub-populations that the value of K is different from $K = 0.5$. However, when we combine the whole population we find, as in Section 3.4.7, that $K = 0.5$ is still close to optimal.

(2) *Velocity distribution function.* The value of K depends on the velocity distribution function of a galaxy, and in particular on the bulge-to-disk ratio and the V/σ ratio for each of the bulge and disk components. In the case of pressure-supported systems with negligible rotation, the average stellar line-of-sight velocity dispersion $\overline{\sigma}_{LOS}$ is a weighted sum of directional components σ_r, σ_θ and σ_ϕ. Excluding observational artefacts, the combination of components is dictated by the anisotropy parameter (Binney & Tremaine 2008, Eqn 4.61)

$$\beta \equiv 1 - \frac{\sigma_\theta^2 + \sigma_\phi^2}{2\sigma_r^2} \tag{3.10}$$

Depending on whether the distribution function of stars is tangentially biased ($\beta < 0$), radially biased ($\beta > 0$) or isotropic ($\beta = 0$), the combination of σ_r, σ_θ and σ_ϕ making up $\overline{\sigma}_{LOS}$ will be different. Thus the K value needs to be adjusted to correct for the unobserved components of $\overline{\sigma}_{LOS}$.

(3) *Observational artefacts.* Since the optimal K value is determined by comparing the scatter in the $\log M_{\star} - \log S_{0.5}$ relation, the quality of kinematic parameter measurements and the scatter of the scaling relation are crucial. Covington et al. (2010) have shown with numerical simulations that instrument blurring effects such as spatial resolution and seeing, which contribute to the scatter in the TF relation, do not show significant effects on the measured $S_{0.5}$ values. A18 also performed a detailed kinematic analysis with spatially resolved rotation velocity measurements. They found that the $S_{0.5}$ parameter consistently reduced the scatter in scaling relations, taking into account the uncertainties in the V_{rot} measurement for dispersion-dominated systems. In Section 3.5.1, we noted that there could be multiple extrinsic causes for a non-linear scaling relation and/or increased scatter, including S/N ratios, instrument resolution, sample selection, and kinematic uncertainties. Thus the best K value is determined by a combination of intrinsic dynamical properties and observational artefacts. In order to use the $\log M_{\star} - \log S_K$ scaling relation to predict physical attributes of observed systems, it is crucial to make sure the scatter in the scaling relation is not dominated by systematic error.

3.6 Conclusions

In this paper we present the $\log M_{\star} - \log S_{0.5}$ scaling relation constructed from the SAMI Galaxy Survey. The $S_{0.5}$ parameter is useful in bringing galaxies of all morphologies onto a common relation. With no sample pruning (other than S/N quality cuts) the scatter in the $\log M_{\star} - \log S_{0.5}$ relation is significantly less than the TF and FJ relations constructed from the same sample. Interestingly, applying only a relative error cut on $S_{0.5}$, without any spaxel-level quality cut, still provides a tight scaling relation. Both the stellar and gas versions of the $\log M_{\star} - \log S_{0.5}$ scaling relation have a sample limit where the relation deviates from a linear relation. We found the sample limits occur at different stellar masses for the gas and stellar samples, implying that the apparent non-linearity in the relation is not physical; this is emphasised by the fact that the $S_{0.5,\rm lim}$ values corresponding to these mass cut-offs are proportional to the effective instrumental resolutions for the stellar and gas measurements.

Comparing $S_{0.5}$ to single-aperture velocity dispersion $\sigma_{3''}$ shows excellent agreement between the two parameters. For the gas measurements the residuals $\sigma_{3'',gas} - S_{0.5,gas}$ trend negatively with galaxy angular size, while for the stellar measurements the residuals $\sigma_{3'',stellar} - S_{0.5,stellar}$ show no correlation with galaxy angular size. In constructing the mass scaling relations, $S_{0.5}$ consistently produced less scatter than $\sigma_{3''}$.

In order to test the importance of choosing an optimal value of K in the construction of the S_k parameter, we measured the scatter of the scaling relations at different values of K. By investigating the correlation between the scatter of the scaling relation and the value of K in the S_K parameter, we found that for both stellar and gas measurements $K = 0.5$ is close to producing the minimum scatter for samples containing only ETGs or mixtures of ETGs and LTGs; however, for samples containing only LTGs $K = 0.2$ gave significantly less scatter.

These findings are broadly consistent with previous studies by C14 using early release of SAMI data and A18 using CALIFA data.

The $S_{0.5}$ kinematic parameter allows the construction of a robust and inclusive galaxy scaling relation with relatively little scatter. The tight correlation between $S_{0.5}$ and $\sigma_{3''}$ implies that a scaling relation with only slightly greater scatter can be constructed for galaxies of all morphologies using large-scale single-fibre galaxy surveys.

Acknowledgements

We thank the referee for their constructive report. The SAMI Galaxy Survey is based on observations made at the Anglo-Australian Telescope. The Sydney-AAO Multi-object Integral field spectrograph (SAMI) was developed jointly by the University of Sydney and the Australian Astronomical Observatory. The SAMI input catalogue is based on data taken from the Sloan Digital Sky Survey, the GAMA Survey and the VST ATLAS Survey. The SAMI Galaxy Survey is supported by the Australian Research Council Centre of Excellence for All Sky Astrophysics in 3 Dimensions (ASTRO 3D), through project number CE170100013, the Australian Research Council Centre of Excellence for All-sky Astrophysics (CAASTRO), through project number CE110001020, and other participating institutions. The SAMI Galaxy Survey website is sami-survey.org.

DB is supported by an Australia Government Research Training Program Scholarship and ASTRO 3D. FDE acknowledges funding through the H2020 ERC Consolidator Grant 683184. JBH is supported by an ARC Laureate Fellowship that funds JvdS and an ARC Federation Fellowship that funded the SAMI prototype. JJB acknowledges support of an Australian Research Council Future Fellowship (FT180100231). JvdS is funded under Bland-Hawthorn's ARC Laureate Fellowship (FL140100278). NS acknowledges support of a University of Sydney Postdoctoral Research Fellowship. Parts of this research were conducted by ASTRO 3D, through project number CE170100013. LC is the recipient of an Australian Research Council Future Fellowship (FT180100066) funded by the Australian Government. SB acknowledges the funding support from the Australian Research Council through a Future Fellowship (FT140101166). SMC acknowledges the support of an Australian Research Council Future Fellowship (FT100100457). BG is the recipient of an Australian Research Council Future Fellowship (FT140101202). MSO acknowledges the funding support from the Australian Research Council through a Future Fellowship (FT140100255). Support for AMM is provided by NASA through Hubble Fellowship grant #HST-HF2-51377 awarded by the Space Telescope Science Institute, which is operated by the Association of Universities for Research in Astronomy, Inc., for NASA, under contract

NAS5-26555. SKY acknowledges support from the Korean National Research Foundation (2017R1A2A1A05001116) and by the Yonsei University Future Leading Research Initiative (2015-22-0064). This study was performed under the umbrella of the joint collaboration between Yonsei University Observatory and the Korean Astronomy and Space Science Institute.

Chapter 4

IFU scaling relation for dwarf galaxies

This chapter is published in Monthly Notices of the Royal Astronomical Society as: SHαDE: survey description and mass-kinematics scaling relations for dwarf galaxies. **Barat, Dilyar,** et al, 2020, MNRAS, 498, 5885.

4.1 Abstract

The Study of Hα from Dwarf Emissions (SHαDE) is a high spectral resolution (R=13500) Hα integral field survey of 69 dwarf galaxies with stellar masses $10^6 < M_\star < 10^9 M_\odot$. The survey used FLAMES on the ESO Very Large Telescope. SHαDE is designed to study the kinematics and stellar populations of dwarf galaxies using consistent methods applied to massive galaxies and at matching level of detail, connecting these mass ranges in an unbiased way. In this paper we set out the science goals of SHαDE, describe the sample properties, outline the data reduction and analysis processes. We investigate the $\log M_\star - \log S_{0.5}$ mass–kinematics scaling relation, which have previously shown potential for combining galaxies of all morphologies in a single scaling relation. We extend

the scaling relation from massive galaxies to dwarf galaxies, demonstrating this relation is linear down to a stellar mass of $M_\star \sim 10^{8.6} M_\odot$. Below this limit, the kinematics of galaxies inside one effective radius appear to be dominated by the internal velocity dispersion limit of the Hα-emitting gas, giving a bend in the $\log M_\star - \log S_{0.5}$ relation. Replacing stellar mass with total baryonic mass using gas mass estimate reduces the severity but does not remove the linearity limit of the scaling relation. An extrapolation to estimate the galaxies' dark matter halo masses, yields a $\log M_h - \log S_{0.5}$ scaling relation that is free of any bend, has reduced curvature over the whole mass range, and brings galaxies of all masses and morphologies onto the virial relation.

4.2 Introduction

Dwarf galaxies are the most common galaxies in the Universe. In the current paradigm of galaxy formation, they are the building blocks of larger galaxies, so understanding their properties is key to understanding the cosmic process of structure formation (e.g. Searle & Zinn 1978). Thanks to large numerical simulations (e.g. EAGLE, Schaye et al. 2015; HorizonAGN, Dubois et al. 2014; IllustrisTNG, Springel et al. 2018; and Romulus, Tremmel et al. 2017), the spatial distribution of cosmic structures is understood relatively well (e.g. Artale et al. 2017, but see Hatfield et al. 2019 for a different view). However, these simulations have insufficient resolution to accurately simulate galaxies with stellar masses $M_\star < 10^9\,\mathrm{M}_\odot$, and so cannot reliably predict the properties of dwarf galaxies. In addition, these large cosmological simulations include a number of simplifications, so-called 'subgrid physics', which implement the effect of physical processes on scales that are currently impossible to simulate. These include star formation (e.g. Dutton et al. 2019), stellar feedback and supernova feedback (e.g. Hopkins et al. 2014; Marinacci et al. 2019), active-galactic nuclei feedback (AGN; e.g. Booth & Schaye 2009), metal diffusion in and outside the inter-stellar medium (e.g.

Hafen et al. 2019), but also purely gravitational collisions (so-called softening; see e.g. Vogelsberger et al. 2019, their Table 2).

The impact of subgrid physics (and of its implementation) changes with galaxy properties. Given that $M_\star$ is one of the most fundamental galaxy properties, dwarf galaxies represent an invaluable testbed, because they allow us to study how the effect of these different physical processes change below $M_\star = 10^9\,\mathrm{M_\odot}$, the dwarf-galaxy mass threshold adopted in this work. In fact, while regular galaxies span already three orders of magnitude in stellar mass ($10^9 < M_\star < 10^{12}\,\mathrm{M_\odot}$), including dwarf galaxies doubles the baseline in $M_\star$, adding the mass range between 10^6 and $10^9\,\mathrm{M_\odot}$.

Despite the desirability of including dwarf galaxies in large extragalactic surveys, the study of these low-mass systems is hampered by their defining physical properties: dwarf galaxies are less luminous than regular galaxies, so observations require longer integration times and/or larger collecting areas; they are smaller, so studying their structure requires better spatial resolution; finally, dwarf galaxies have lower velocity dispersions, so an unbiased measurement of their kinematics requires either high spectral resolution or very high signal to noise (cf. Zhou et al. 2017, their sec. 2.2.2).

In light of these obstacles, it is not surprising that dwarf galaxies have been mostly left out of the the integral field spectroscopy revolution of this decade: for example, SAMI has a mass limit of $10^8\,\mathrm{M_\odot}$ (Croom et al. 2012; Bryant et al. 2015) while MaNGA has a mass limit of $10^9\,\mathrm{M_\odot}$ (Bundy et al. 2015). This gap is partially filled by studies of local dwarf galaxies, but these works do not employ the same methods as large extragalactic surveys: they rely either on neutral hydrogen observations (e.g. Hunter et al. 2012), or on individually-resolved stars (e.g. Tolstoy et al. 2009), neither of which is yet available beyond the local Universe. A notable exception is represented by the SIGRID survey (Nicholls et al. 2011), however even the high spectral resolution of SIGRID ($R = 7000$) is insufficient to probe the regime of thermal broadening ($\lesssim 15\,\mathrm{km\,s^{-1}}$) that might bias dynamical scaling relations of dwarf galaxies. In summary, at present, no optical survey can simultaneously deliver sufficient numbers, spatial resolution, and spectral resolution to reliably study the kinematics and dynamics of dwarf galaxies, and to compare them to more massive galaxies.

The SHαDE survey was designed to fill this gap, and to deliver a sample of 69 dwarf galaxies with high spectral and spatial resolution Hα observations. The survey was designed with four goals in mind: (i) to test the linearity of galaxy scaling relations over a range in mass and with sufficient spectral resolution to not be observationally limited; (ii) to measure and explain f_{asym}, the fraction of dwarf galaxies with asymmetric kinematics; (iii) to study the dynamical effect of star-formation feedback in the low-mass regime; and (iv) to study angular momentum accretion.

The main goals of this paper are to introduce the SHαDE survey and to present our results for dwarf scaling relations. The paper is organised as follows: in Section 4.3 we outline the scientific goals of SHαDE; Section 4.4 presents the selection criteria and sample, the observations, and the data reductions; the analysis of this data is presented in Section 4.5. We then focus on the first of the survey goals, providing our analysis of mass–kinematics scaling relations for the SHαDE galaxies in Section 4.6; in Section 4.7 we discuss our results; finally, Section 4.8 provides a summary of our findings.

Throughout this paper we assume a ΛCDM cosmology with Ω_M=0.3, Ω_λ=0.7 and H_0=70 km s^{-1}, and a Chabrier initial mass function (Chabrier 2003). All magnitudes are in the AB system (Oke & Gunn 1983).

4.3 Goals of SHαDE

Dwarf galaxies with stellar mass $M_\star < 10^9\,\mathrm{M}_\odot$ are special compared to normal galaxies with $10^9 < M_\star < 10^{12}\,\mathrm{M}_\odot$. The low masses of dwarf galaxies, and the environments in which they reside, make them interesting targets which can challenge theories of galaxy formation and evolution that are based on massive galaxies. This section outlines the types of experiments that can be carried out using the SHαDE observations, including galaxy scaling relations, kinematic asymmetries, star formation and ISM turbulence, and angular momentum accretion in dwarf galaxies.

4.3.1 Galaxy scaling relations

For disc galaxies, optical luminosity correlates with HI 21 cm line width; this is the Tully-Fisher (TF) relation (Tully & Fisher 1977). Since the discovery of this scaling relation, a plethora of studies have been carried out investigating the scaling relation across multiple photometric bands (for a summary see Ponomareva et al. 2017). The TF relation has been widely used in determining galaxy distances, and subsequently measuring cosmological constants and galaxy flows (e.g. Courtois & Tully 2012). The TF relation is also an important tool in testing various theories of gravity (e.g. Milgrom 1983; Sanders 1990; Mo et al. 1998; McGaugh 2012; Desmond & Wechsler 2015).

The stellar mass TF relation (where luminosity is replaced by stellar mass) has long been observed to have a ‘knee’ at low circular velocity where the slope of the relation steepens (Matthews et al. 1998; McGaugh et al. 2000; Amorín et al. 2009; McGaugh & Wolf 2010; Sales et al. 2017). This region of the relation is predominantly occupied by dwarf galaxies, which are found to have on average larger gas fractions than regular star-forming galaxies (McGaugh et al. 2000; Hunter et al. 2012; Lelli et al. 2014; Oh et al. 2015). Further HI follow-up of dwarf galaxies showed that, by including the cold gas mass and so using the total baryonic mass instead of stellar mass, a linear TF relation is restored over 5 orders of magnitude in mass (McGaugh et al. 2000; McGaugh 2005; Lelli et al. 2016; Iorio et al. 2017). This illustrates both the importance of extending observations of galaxy scaling relations to dwarf galaxies and of understanding the physical basis of such relations.

At the massive-galaxy end of the TF relation, it has been shown that even passive, early-type galaxies obey the TF relation whenever they include enough gas to obtain reliable measurements of the circular velocity (den Heijer et al. 2015). However, early-type galaxies differ from late-type galaxies in that most early-type galaxies do not have detectable HI gas (Cortese et al. 2020), and their kinematics are dominated by unordered (or at least complex) motions, observed as velocity dispersion, rather than the highly ordered motions observed as rotation velocity. The Faber-Jackson (FJ) relation (Faber & Jackson 1976) for early-type galaxies is the correlation of their velocity dispersions with their luminosities or stellar masses.

Tightly-correlated TF or FJ relations require reliable morphological selection of (respectively) late-type or early-type galaxy samples, which is time-consuming and difficult. The desirability of unifying these relations in a generalized kinematic scaling relation that applies to galaxies of all types, which became possible with the advent of integral field spectroscopy (IFS), led to the construction of the $S_{0.5}$ parameter (Weiner et al. 2006) defined as:

$$S_{0.5} \equiv \sqrt{0.5V_{\mathrm{rot}}^2 + \langle\sigma_{\mathrm{los}}\rangle^2} \tag{4.1}$$

where V_{rot} is the rotation velocity and $\langle\sigma_{\mathrm{los}}\rangle$ is the average line-of-sight velocity dispersion. This parameter can be thought as a proxy for the circular velocity, with a uniform asymmetric drift correction, independent of galaxy morphology. Despite the simplistic approximation, $S_{0.5}$ correlates tightly with stellar mass, and—crucially—this correlation holds for all morphological types and for kinematics measured either from stars or warm ionised gas (Cortese et al. 2014). The $\log M_\star - \log S_{0.5}$ relation being, in both these senses, more universal than the TF or FJ relations, can be a powerful probe of galaxy dynamics (e.g. Oh et al. 2016; Cannon et al. 2016), structure formation (e.g. Dutton 2012; Tapia et al. 2017; Desmond et al. 2019), and can be used to measure distances and peculiar velocities and so cosmological parameters (e.g. McGaugh 2012; Glazebrook 2013; Said et al. 2015). In fact, galaxy formation theory in the context of the ΛCDM model predicts that the baryon fraction f_b increases with halo mass M_h, and peaks at $M_h \approx 10^{12}\,\mathrm{M}_\odot$ (e.g. Moster et al. 2013). Observations appear to confirm this expectation: within one effective radius (R_e), regular galaxies are baryon dominated (e.g. Cappellari et al. 2013), whereas dwarf galaxies seem to be dark matter dominated at all radii (Penny et al. 2009). If this scenario is correct, we expect this to be reflected in the $\log M_\star - \log S_{0.5}$ relation: when the dynamics become dominated by dark matter, stellar or baryonic mass will be a less precise tracer of the dynamics, due to the relatively large scatter in the f_b–M_h relation (e.g. Di Cintio & Lelli 2015; Desmond 2017). Alternatively, dwarf galaxies might be baryon-dominated within one R_e (Sweet et al. 2016), and claims of dark-matter-dominated dwarfs may stem from non-equilibrium dynamics in tidal dwarf galaxies.

The $\log M_\star - \log S_{0.5}$ relation is linear over three orders of magnitude in mass (e.g. Cortese et al. 2014), but, within limits imposed by the current mass range and spectral resolution, it *appears* to become steeper below $M_\star = 10^9\,\mathrm{M}_\odot$ (Barat et al. 2019, hereafter: B19). This value is intriguingly close to the theoretical predictions (Cortese et al. 2014, Aquino-Ortíz et al. 2018, Gilhuly et al. 2019); on the other hand, the fact that break in the $\log M_\star - \log S_{0.5}$ relation occurs at different values of $M_\star$ for the stellar and gas kinematics, and just below the instrument spectral resolution in each case, suggests that measurement systematics might also play a role, producing inflated velocity dispersions that make the relation appear steeper (B19).

In summary, based on current observational evidence is still unclear whether the change of slope in the $\log M_\star - \log S_{0.5}$ relation is due to increasing gas fractions (as for the TF relation, cf. McGaugh et al. 2000), insufficient spectral resolution (cf. B19), non-equilibrium dynamics (a natural consequence of the hypothesis in Sweet et al. 2016), or increasing dark matter fraction below $M_\star \approx 10^8$–$10^9\,\mathrm{M}_\odot$ (predicted by e.g. Behroozi et al. 2013). Part of the uncertainty is due to the fact that current IFS surveys are designed to probe galaxies with $M_\star \gtrsim 10^9\,\mathrm{M}_\odot$, so that we lack accurate data precisely where the relation becomes most interesting. It is clear that obtaining new data with better spectral resolution will extend the baseline in $M_\star$ and better constrain the $\log M_\star - \log S_{0.5}$ relation.

4.3.2 Kinematic asymmetries in dwarf galaxies

The hypothesis that the bend in the $\log M_\star - \log S_{0.5}$ relation is due to non-equilibrium dynamics of the warm ionised gas tracer is plausible. Because of Malmquist bias, magnitude-limited samples of star-forming dwarf galaxies may have higher-than-average SFR per unit mass (specific SFR; sSFR), which is associated with mergers (Robaina et al. 2009) and/or substantial accretion of cold gas (Elmegreen et al. 2012; Thorp et al. 2019). Indeed, Bloom et al. (2017a) find that a fraction $f_{\rm asym} \sim 0.5$ of isolated dwarf galaxies exhibit irregular gas kinematics, inconsistent with a rotating disc. These disturbances increase the scatter at the low-mass end of the TF relation (Bloom et al. 2017b), and therefore might also contribute to steepening the low-mass end slope of the $\log M_\star - \log S_{0.5}$ relation. Whereas asymmetric gas kinematics in massive galaxies is usually explained by recent galaxy-galaxy interactions, this is not the case for dwarf galaxies—these low-mass systems differ in two fundamental aspects from their high-mass counterparts. Firstly, asymmetric kinematics: dwarfs are found predominantly in isolation, thus ruling out a dominant role for tidal interactions. Secondly, most dwarfs have regular photometric shapes that are inconsistent with recent substantial mergers.

It is possible that these galaxies are accreting relatively large amounts of unseen neutral hydrogen from the intergalactic medium, because their halo mass is smaller than the quenching threshold (cf. Elmegreen et al. 2012). In this case, we expect $f_{\rm asym}$ to be insensitive to $M_\star$ for dwarf galaxies. Alternatively, Bloom et al. (2018) propose that the asymmetries are caused by the discrete distribution of giant molecular clouds, which becomes more coarse with decreasing stellar mass. In this case, $f_{\rm asym}$ must strongly increase with decreasing $M_\star$. Probing the gas kinematics well below $M_\star = 10^9\,{\rm M}_\odot$ could discriminate between these two models.

4.3.3 The link between star formation and ISM turbulence

Star-forming dwarf galaxies have higher SFR per unit mass on average than regular galaxies. This fact follows from the sub-linear slope of the star-forming sequence, $\log \mathrm{SFR} = (0.67 \pm 0.08) \log M_\star$ (Noeske et al. 2007; see also Speagle et al. 2014, Renzini & Peng 2015), so that the sSFR decreases with $M_\star$. With their high sSFR, star-forming dwarf galaxies can also be used to probe the interplay between star formation and gas dynamics. Part of the Hα velocity dispersion is due to turbulent motions, which are thought to regulate the conversion of gas into stars and are therefore key to understanding galaxy formation and evolution (e.g. Green et al. 2010; Federrath & Klessen 2012; Padoan et al. 2014). However, the origin of this turbulence is not well understood: possible mechanisms include star formation feedback, inter-cloud collisions (Tasker & Tan 2009), gas accretion (Klessen & Hennebelle 2010), galactic shear within the gas disc (Krumholz & Burkhart 2016), and magnetorotational instability (Tamburro et al. 2009). Recent IFS surveys have clarified that the relation between gas velocity dispersion and SFR originates from a local relation (Lehnert et al. 2009, 2013). Zhou et al. (2017) found that the observed random motions of the star-forming gas require additional sources beyond star-formation feedback. However, gas turbulence is of the order of 10–15 $\mathrm{km\,s^{-1}}$, smaller than the spectral resolution of all large IFU surveys, which may therefore introduce a systematic bias in the measurements. To test for such bias, a sample of local star-forming galaxies observed at high spectral resolution could help constrain theoretical models.

4.3.4 Angular momentum accretion of dwarf galaxies

The relation between the fundamental parameters of stellar mass $M_\star$ and angular momentum $J_\star$ has been empirically studied since Fall (1983), who found that $j_\star = qM_\star^\alpha$, where $j_\star = J_\star/M_\star$ is the specific stellar angular momentum. The scale factor q varies with morphology in the sense that bulge-dominated galaxies have a lower angular momentum than disk-dominated galaxies of the same mass. The exponent $\alpha \sim 2/3$ agrees with the analogous relation between halo specific angular momentum j_h and halo mass M_h in a scale-free cold dark matter universe, namely $j_h \propto M_h^{2/3}$ (Mo et al. 1998). In addition, the mean specific angular momentum of the baryons j_b is within a factor of two of the halo j_h (Barnes & Efstathiou 1987; Catelan & Theuns 1996a,b; Posti et al. 2018a). While the broad connection between j_b and j_h is still a topic of active research (e.g. Jiang et al. 2019; Posti et al. 2019), the $M_\star$–$j_\star$ relation is generally assumed to be a byproduct of hierarchical assembly, since galaxy mergers increase both mass and angular momentum for the haloes as well as for their stars (Lagos et al. 2018).

Low-mass galaxies are thought to be the building blocks of more massive galaxies, both in mass and angular momentum. However, while the $M_\star$–$j_\star$ relation has been confirmed over a broad range of morphologies (Romanowsky & Fall 2012; Obreschkow & Glazebrook 2014b; Cortese et al. 2016; Fall & Romanowsky 2018; Sweet et al. 2018; Posti et al. 2018b), these works (with the exception of Posti et al. 2018b), have focussed on more massive galaxies with stellar mass $M_\star \gtrsim 10^9\,\mathrm{M}_\odot$. Moreover, dwarf galaxies are fundamentally different to massive galaxies: the interrelated properties of morphology, gas fraction, star formation rate, and metallicity are not related to stellar mass by a simple power-law (e.g. Scodeggio et al. 2002; Dekel & Woo 2003; Salim et al. 2007; Tremonti et al. 2004). Neither does it follow that the relation between $M_\star$ and $j_\star$ should take the form of an unbroken power law over large dynamic range in $M_\star$. Indeed, the semi-analytic models Dark SAGE (Stevens et al. 2016) and GALFORM (Mitchell et al. 2018), cosmological zoom-in simulations NIHAO (Obreja et al. 2016), and cosmological hydrodynamical simulation EAGLE (Lagos et al. 2017) all find that simulated disk-dominated low-mass ($M_\star \lesssim 10^{9.5}\,\mathrm{M}_\odot$) galaxies have more angular momentum than predicted by a constant $\alpha \sim 2/3$ slope. This increased angular momentum could be related to an enhanced gas fraction and/or lower velocity dispersion for dwarf galaxies (Obreschkow et al. 2016). A hint of such an elevation above $\alpha = 2/3$ is seen in Fall

& Romanowsky (2013), which includes just four galaxies with masses in the range $10^{8.5} < M_\star < 10^{9.5}\,\mathrm{M}_\odot$. Posti et al. (2018b) extended the $M_\star$–$j_\star$ relation to stellar masses as low as $M_\star \gtrsim 10^7\,\mathrm{M}_\odot$ and found a constant $\alpha = 0.55$ for all stellar masses, which is at odds with the predictions of $\alpha \sim 2/3$ for massive galaxies and a shallower slope at dwarf masses. However, while Posti et al. (2018b) measured the relation down to $M_\star \gtrsim 10^7\,\mathrm{M}_\odot$, the sample only included six galaxies with $10^7 < M_\star < 10^8\,\mathrm{M}_\odot$. The lowest-mass galaxies have very small uncertainties, but those with $10^8 < M_\star < 10^{9.5}\,\mathrm{M}_\odot$ seem to show a $j_\star$ above the fitted relation, in line with Fall & Romanowsky (2013) and simulations such as Stevens et al. (2016). To test the robustness of this previous finding, and determine whether or not dwarf galaxies have elevated angular momentum, a larger sample extending to yet smaller stellar masses is needed.

4.4 Data

The SHαDE sample consists of 49 star-forming galaxies selected form the Sloan Digital Sky Survey Data Release 12 (hereafter: SDSS; Eisenstein et al. 2011; Alam et al. 2015), as well as 20 targets from the SAMI survey as control sample. These targets are observed with high spectral resolution IFU FLAMES instrument, and reduced with the standard data reduction package. Other ancillary data are obtained from the SDSS DR12. Details of these processes are outlined in the subsections below.

4.4.1 The Sample

The sample was designed to probe, as uniformly as possible, the low-mass end of the galaxy distribution. We selected our targets from SDSS by applying four constraints: (i) stellar masses in the range $10^5 \leq M_\star \leq 10^{8.5}\mathrm{M}_\odot$; (ii) apparent sizes in the range $1.2 \leq R_d\,[\mathrm{arcsec}] \leq 11$; (iii) H$\alpha$ fluxes above a threshold $f_{\mathrm{H}\alpha} > 5 \times 10^{-16}[\mathrm{erg\,s^{-1}\,cm^{-2}\,\AA^{-1}\,arcsec^{-2}}]$; and (iv) targets observable in the relevant semester

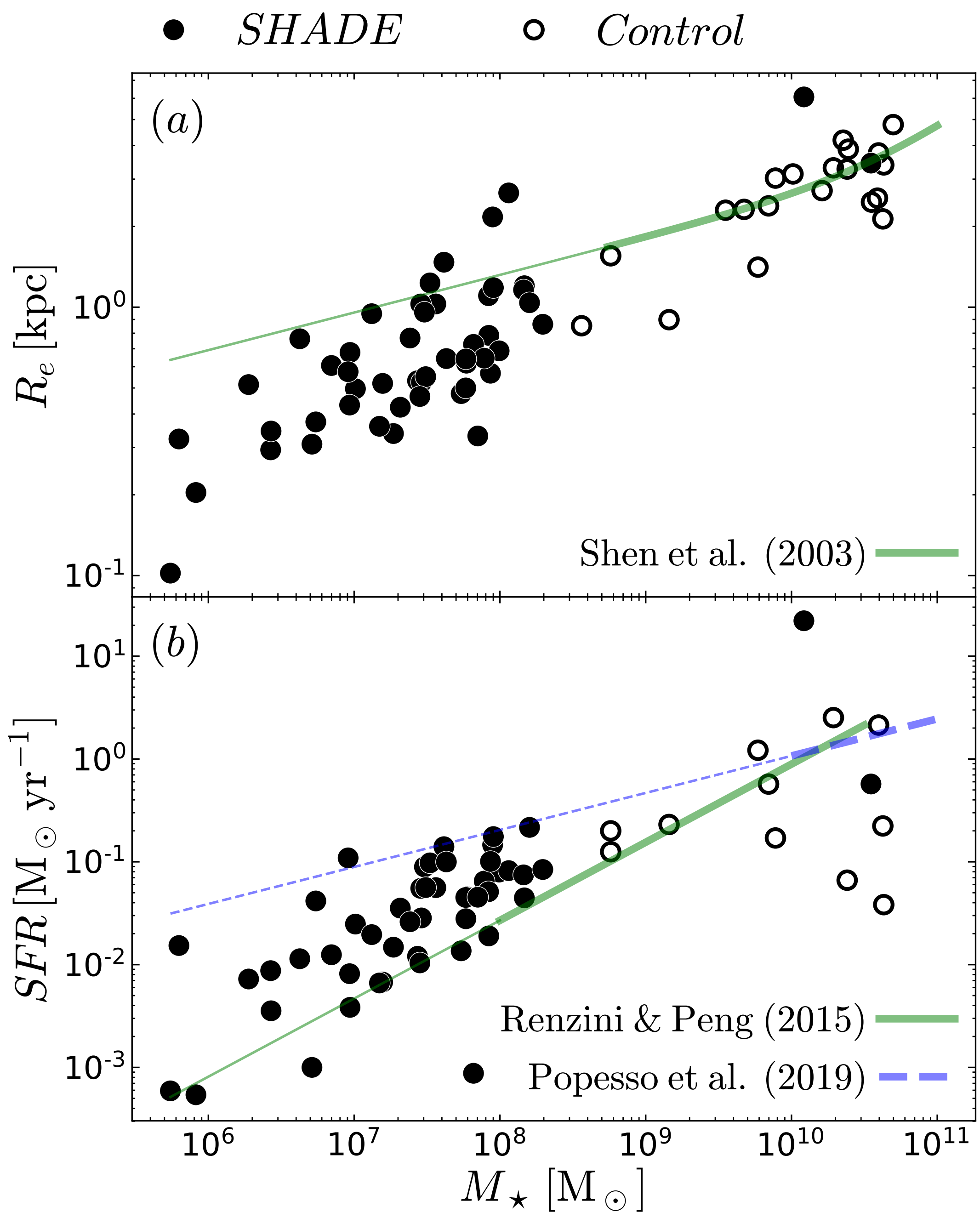

Figure 4.1: The SHαDE galaxies (filled circles) lie close to both the mass–size relation (panel a) and the star-forming sequence (panel b) of local star-forming galaxies. The SHαDE Survey also includes a control sample of 20 non-dwarf galaxies, drawn from the SAMI Survey (open circles). The lines are best-fit relations drawn from the literature (thick/thin lines mark the fitted/extrapolated domain of each relation).

(March to August). The first three criteria ensure (i) coverage of the mass range relevant to our goals; (ii) sufficient spatial resolution, while fitting within the instrument field of view (FOV); and (iii) sufficient signal-to-noise ratio (SNR) to measure Hα kinematics. These criteria and the spectral resolution of the instrument also mean we have sufficient spectral/velocity resolution (even at the low end of the mass range) to measure the expected velocity dispersions based on extrapolating the $\log M_\star - \log S_{0.5}$ relation.

We visually inspected this set of 601 galaxies and rejected 75 objects that proved to be artefacts or galaxies with significant contamination from interlopers or neighbours (including mergers). For each target galaxy the FLAMES instrument requires a guide star, which we selected from the GAIA Survey (Gaia Collaboration et al. 2016); as a result, we removed another 104 valid targets that had no suitable guide star in GAIA public data release 2 (Gaia Collaboration et al. 2018). From this final pool of 422 galaxies, we scheduled 49 targets for observation using a custom scheduler that aims at uniformly sampling the target mass range while ensuring that no target had airmass larger than 1.5 at any point during the observation.

The main SHαDE sample is complemented with 20 targets from the SAMI Survey to be used as a control sample; these additional galaxies were randomly selected within $10^{8.5} < M_\star < 10^{10.5}\mathrm{M}_\odot$ to span a broader range of masses, to ensure a consistency in the $S_{0.5}$ measurements across SAMI and SHADE.

Note that 2 non-control high-mass ($M_\star > 10^{10}\mathrm{M}_\odot$) galaxies are present in the SHαDE sample, this is because their stellar mass values from SDSS used for target selection were significantly lower in comparison to the method used in this paper. Details on our stellar mass measurement is described in section 4.4.4.

The position of the SHαDE and control galaxies on the mass–size plane is shown in Figure 4.1a (filled and empty circles, respectively). Both sets of galaxies have sizes that are not inconsistent with the local mass–size relation for star-forming galaxies (solid green line; Shen et al. 2003). The mass–size relation is measured only down to $10^{8.5}$ $M_\odot$: below this lower limit we simply extrapolated the best-fit function (indicated by the thin section of the line). The SHαDE galaxies lie systematically below this extrapolation in radius, but are consistent with a single linear mass–size relation spanning the entire mass range. For the star-forming sequence, the SHαDE galaxies lie systematically above the local relation and its extrapolation to lower masses (Renzini & Peng 2015, green line in Figure 4.1b), as expected given that we selected bright Hα emitters (cf. Section 4.4.1). However, other authors have reported a shallower slope for the star-forming sequence (e.g. Popesso et al. 2019; dashed blue line in Figure 4.1b); the SHαDE galaxies lie systematically below a (more extreme) extrapolation of this relation.

4.4.2 Observations

We present new data from the FLAMES instrument at the 8 m VLT Unit Telescope 2 (Pasquini et al. 2002), using the ARGUS IFU and the GIRAFFE optical spectrograph. ARGUS is a rectangular array of 22 × 14 square microlenses; at the 1:1 scale, each microlens samples 0.52 arcsec and the IFU FOV spans $11.4 \times 7.3\,\mathrm{arcsec}^2$. Light from individual microlenses in the IFU is fed to GIRAFFE using optical fibres. Besides the IFU itself, ARGUS also provides 15 dedicated sky fibres, which can be placed anywhere inside the instrument FOV. Within the slit, the fibres are arranged in 15 bundles, each consisting of 20 object fibres and a single sky fibre. On the detector, the fibres are separated by 5.3 pixels, whereas the bundles are separated by 12–20 pixels.

We used setup L682.2, consisting of the low-resolution grating centred at $\lambda_{\mathrm{central}} = 6822\,\mathrm{\AA}$ and the LR06 filter. This configuration delivers a nominal spectral resolution $R = 13500$ ($\Delta\lambda = 0.505\,\mathrm{\AA}$) and the spectrum is sampled with 0.2 Å pixels. The wavelength range is 6440–7160 Å, covering the rest-frame Hα emission at 6562.8 Å up to redshift $z \approx 0.08$, appropriate for our target selection. The detector read speed was set to 50 kHz and high gain, because at this spectral resolution our data is limited by

Table 4.1: Summary of observations: the main sample.

SHαDE ID (1)	SDSS SpecObjID (2)	$f_{\mathrm{H}\alpha}$ † (3)	T_{exp} s (4)	$\langle$AM$\rangle$ (5)	Seeing arcsec (6)	Run (7)
1	344558384307005440	8.17±1.59	900 × 3	1.12	0.92	A
2	385144108173256704	7.66±3.31	900 × 3	1.12	0.83	A
9	388552594202585088	7.10±4.25	900 × 3	1.96	1.22	B
42	585558149897938944	8.72±0.63	900 × 3	1.28	0.99	A
46	585553751851427840	9.50±0.64	900 × 3	1.12	1.33	A
55	666581432214251520	15.96±0.73	500 × 2	1.57	1.34	B
56	1326366762505103360	10.35±2.07	500 × 2	1.27	0.6	A
59	736372110183655424	9.49±0.13	900 × 3	1.03	0.89	B
64	743256427883161600	21.76±0.92	500 × 2	1.16	1.16	B
128	1025746258003781632	10.30±2.01	500 × 2	1.17	1.29	A
132	1033705622308153344	10.39±0.61	500 × 2	1.15	1.66	A
136	667815084277393408	25.33±3.56	500 × 2	1.16	0.83	A
137	1159814941646022656	9.23±3.31	900 × 3	1.17	0.72	B
148	1151799775146829824	6.32±0.33	900 × 3	1.16	1.17	A
151	1105748373979293696	7.29±1.16	900 × 3	1.14	0.75	A
152	1150797565365610496	6.56±4.37	900 × 3	1.24	0.81	A
165	459448556403582976	16.12±0.69	500 × 2	1.12	0.73	B
171	1128315028525574144	11.57±0.72	500 × 2	1.26	1.54	A
194	1819558756229343232	6.70±2.57	900 × 3	1.73	1.04	A
200	1375985247325284352	11.72±0.98	500 × 2	1.22	0.6	A
218	1816204695102842880	6.63±1.33	900 × 3	1.28	0.77	A
231	1939939348900243456	30.66±4.00	500 × 2	1.95	0.64	B
260	1829747929997404160	5.57±0.47	900 × 3	1.2	0.74	A
271	2014355951074699264	6.97±2.58	900 × 3	1.23	0.88	A
283	1946713989006256128	10.24±0.71	500 × 2	1.3	0.8	B
284	2058148387030591488	46.53±1.42	500 × 2	1.18	0.65	A
286	3321458402864949248	7.41±3.64	900 × 3	1.25	1.26	A
288	2049141199587010560	10.15±1.66	500 × 2	1.17	0.65	A
311	2485035976443848704	8.58±2.03	900 × 3	1.42	0.99	A
314	1234065512632182784	21.22±11.44	500 × 2	1.3	0.69	A
315	431222718478706688	10.91±0.74	500 × 2	1.3	0.85	A
319	1150711803458643968	5.82±0.25	900 × 3	1.1	1.3	A
320	1155193413423884288	7.15±0.36	900 × 3	1.1	1.45	A
322	1254417201423738880	33.39±11.03	500 × 2	1.64	0.77	A
323	1157472431619729408	8.58±4.37	900 × 3	1.26	0.69	A
327	1166516459447281664	5.80±2.05	900 × 3	1.14	0.7	B
330	425751828999727104	6.01±0.47	900 × 3	1.42	0.84	A
331	1150794541708634112	6.53±2.98	900 × 3	1.29	1.16	A
343	1219400493801957376	8.16±6.26	900 × 2	1.52	1.52	A
344	1676573588242589696	6.64±0.40	900 × 3	1.13	0.86	B
352	1214947748281870336	5.02±0.56	900 × 3	1.14	0.67	B
424	3087280562621147136	17.63±3.15	500 × 2	1.32	1.47	A
430	3088358084452575232	6.52±0.45	900 × 3	1.37	1.38	A
431	3099604713595758592	7.38±0.46	900 × 3	1.27	2.01	A
433	3091856729999173632	17.83±5.95	500 × 2	1.87	0.95	B
435	3132266537138808832	7.57±0.55	900 × 3	1.43	1.35	A
469	2931991316961191936	11.77±0.75	500 × 2	1.37	0.92	A
496	952674913926277120	12.22±0.79	500 × 2	1.17	0.81	A
520	1156448780808120320	10.71±2.31	500 × 2	1.51	0.87	A

† Units of $10^{-16}\,\mathrm{erg\,s^{-1}\,cm^{-2}\,\AA^{-1}\,arcsec^{-2}}$. Source: SDSS DR12 (Thomas et al. 2011)

Table 4.2: Summary of observations: the control sample, drawn from SAMI.

SHαDE/ GAMA ID (1)	$f_{\mathrm{H}\alpha}$ † (2)	T_{exp} s (3)	⟨AM⟩ (4)	Seeing arcsec (5)	Run (6)
106049	4.78±1.94	900 × 3	1.53	1.06	B
296934	28.65±7.44	900 × 3	1.29	0.71	C
319150	4.77±1.74	900 × 3	1.29	1.12	B
511921	13.92±3.47	900 × 3	1.75	0.95	B
594906	30.35±3.60	900 × 3	1.96	1.05	B
9008500333	2.75±0.93	900 × 3	1.10	0.79	B
9008500356	1.50±0.63	900 × 3	1.10	1.32	B
9011900125	-	900 × 3	1.11	0.72	B
9011900128	-	900 × 3	1.39	0.83	B
9016800065	2.13±0.51	900 × 3	1.12	0.68	B
9016800314	1.36±0.40	900 × 3	1.12	1.33	B
9091700123	-	900 × 3	1.35	0.89	B
9091700137	-	900 × 3	1.02	1.13	B
9091700444	-	900 × 3	1.11	1.20	B
9239900178	3.02±1.15	900 × 3	1.75	1.31	B
9239900182	19.10±1.88	900 × 3	1.05	1.38	B
9239900237	16.28±2.62	900 × 3	1.23	1.11	B
9239900246	-	900 × 3	1.35	1.05	B
9239900370	-	900 × 3	1.20	0.92	B
9388000269	-	900 × 3	1.06	1.15	B

† Units of $10^{-16}\,\mathrm{erg\,s^{-1}\,cm^{-2}\,\AA^{-1}\,arcsec^{-2}}$. Not used for the control sample.

read-out noise.

The observations (see Tables 4.1 & 4.2) were carried out under ESO program 0101.B-0505 in two Visitor Mode runs (A and B), complemented by a Service Mode run (C) allocated as time compensation. Each target was observed for either 17 min (for targets brighter than $f_{\mathrm{H}\alpha} > 5 \times 10^{-16}\,\mathrm{erg\,s^{-1}\,cm^{-2}\,\AA^{-1}\,arcsec^{-2}}$) or 45 min; the integrations were split into either two 8.5 min-long exposures or three 15 min-long exposures. The median airmass-corrected seeing was 0.88 arcsec, with a dispersion of 0.32 arcsec (values are full-width at half maximum, FWHM).

4.4.3 Data reduction

We perform a standard data reduction[1] using the `giraf-kit` package provided by ESO (Blecha et al. 2000; Royer et al. 2002). The bias level was estimated using the overscan

---

[1] The current reduced data is not flux-calibrated, but flux-calibration will be performed for the official data release (Sweet et al. in prep.).

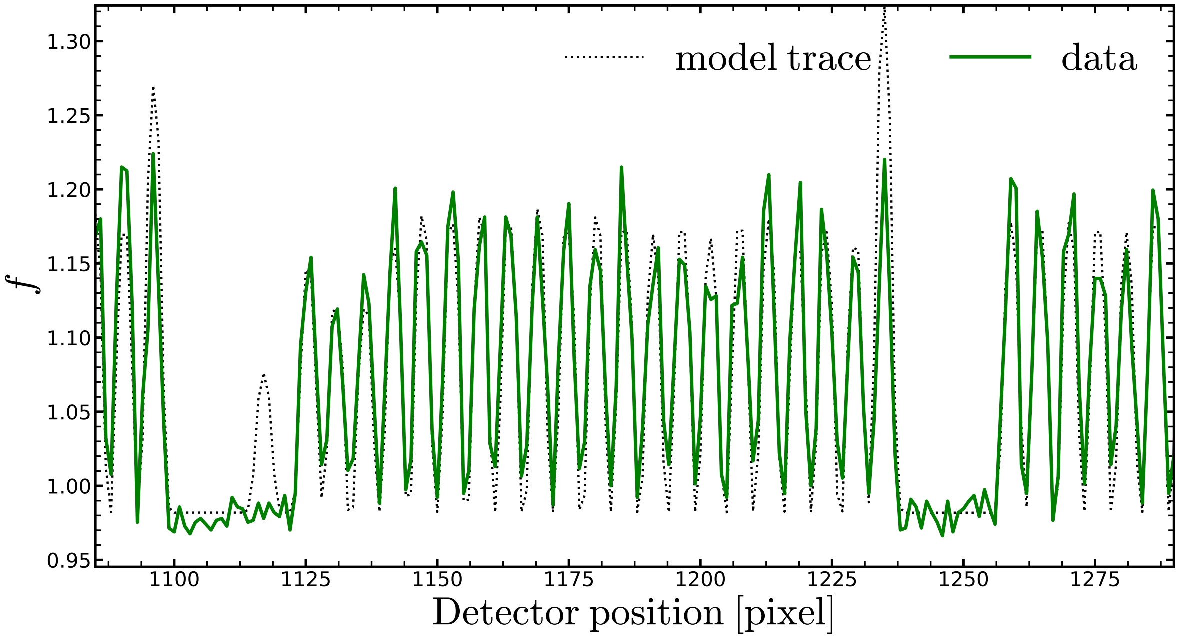

Figure 4.2: Comparison of a section of the model for the spatial distribution of light derived from a flat-field frame with data from a science frame. The model trace (dotted black line) is the multiple Gaussian fit to a flat-field frame; the science trace (solid green line) is the region around the sky line at $\lambda = 6864.97\,\text{Å}$ for a science frame. For display purposes, we show only one bundle, consisting of the 21 fibre traces between the two troughs; the fibre present in the fibre-flat model but absent in the science frame is used for simultaneous wavelength calibration and was switched off in our setup.

regions. For each galaxy, we traced the centroid and width of the spectra using the most recent Nasmyth flat, and derived both the flat field and the scattered light model. For each row along the dispersion direction, we sum the flux inside the fibre trace (optimal extraction, Horne 1986, is not yet implemented); given that the science spectra are too faint to trace their position on the CCD, we use the fibre traces derived from the Nasmyth flat-field frames. This approach is justified by a direct comparison of the flat-field traces to the science traces, which can be determined around bright emission sky lines (Figure 4.2).

Table 4.3: Prominent singlet sky emission lines used to measure the instrument spectral resolution (from Hanuschik 2003).

Line ID (1)	λ_c [Å] (2)	FWHM [Å] (3)	Line ID (1)	λ_c [Å] (2)	FWHM [Å] (3)
1	6477.921	0.158	10	6841.963	0.154
2	6505.000	0.251	11	6871.073	0.158
3	6522.433	0.166	12	6889.302	0.173
4	6533.050	0.173	13	6900.808	0.157
5	6544.036	0.163	14	6912.638	0.162
6	6562.760	0.226	15	6923.192	0.189
7	6568.789	0.159	16	6939.542	0.150
8	6596.645	0.175	17	7003.873	0.253
9	6627.632	0.252			

4.4.3.1 Wavelength calibration

The wavelength calibration relies on dedicated Th-Ar lamp exposures. In the relevant function of `giraf-kit`, the dispersion solution consists of an optical model (which predicts the position of each line on the detector), plus a polynomial correction (Royer et al. 2002). The free parameters are constrained iteratively using the position of 70 unsaturated emission lines on the detector. We validate the resulting calibration using prominent emission sky lines taken directly from the science frames. First we created a model continuum spectrum, consisting of the sum of the galaxy and sky continua. We smoothed the spectra with a median filter (kernel width of 10.2 Å, or 51 pixels), we masked the regions within five FWHM from any emission line, and we fitted a spline to the smooth, masked spectrum. This model was then subtracted from the observed spectra to obtain an emission-line spectrum.

We selected a list of 17 bright singlet lines from the UVES Atlas (Hanuschik 2003, Table 4.3) and fitted each line with a Gaussian, allowing for uniform background[1]. We used the bounded least squares algorithm from `scipy.optimize`, which in turn relies

---

[1] We tested the use of doublet emission lines by fitting the lines simultaneously, but found the measured line widths have larger scatter than the singlet emission lines and so discarded doublets.

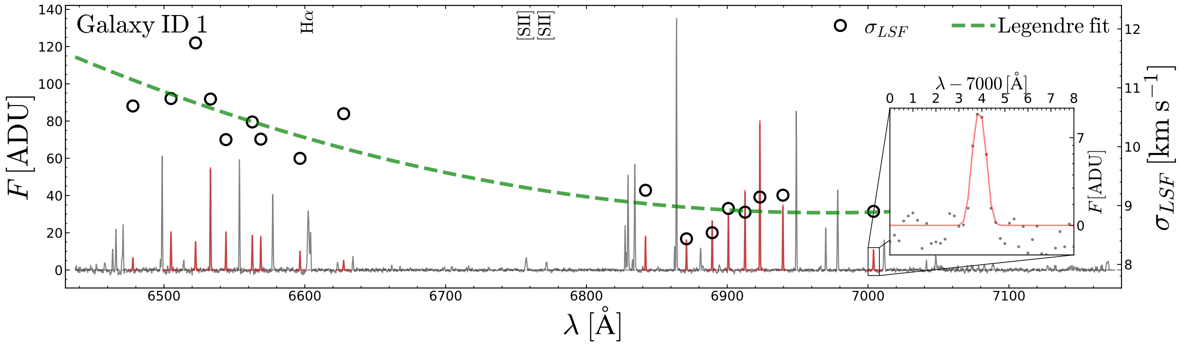

Figure 4.3: The spectral resolution is well approximated by a second-order polynomial in wavelength. The solid grey line is the IFU-stacked continuum-subtracted spectrum for galaxy ID 1 (left scale). To measure the instrument spectral resolution (right scale), we fit a Gaussian to the most prominent singlet sky lines (best-fit models are overlaid as solid red lines). The measured dispersions are marked by circles and are located at the best-fit wavelength of the relevant sky line. The dashed green line is the best-fit second-order Legendre polynomial to the line dispersions. The interpolated spectral resolution at $\lambda = 6882\,\text{Å}$ is $\sigma = 9.06\,\text{km}\,\text{s}^{-1}$. The inset diagram shows an example line fit, where the black dots represent the data and the red line traces the best-fit model.

on the Trust Region Reflective algorithm for minimisation (Branch et al. 1999). As initial values, we used the intensity, central wavelength, and intrinsic line dispersion reported in Hanuschik (2003).

As a diagnostic of the wavelength calibration, we take the relative offset $\lambda_m/\lambda_t - 1$ between the measured line wavelength and the value tabulated in the UVES Atlas. We find that both the precision and the accuracy of the wavelength solution are excellent: the standard deviation of the relative offset is 2.6×10^{-6} (0.017 Å in absolute terms), the mean offset is $(-2.5 \pm 0.6) \times 10^{-6}$ (-0.016 ± 0.004 Å).

The instrument dispersion σ_{instr} was then calculated from the best-fit line dispersion by subtracting in quadrature the intrinsic dispersion. The results from the skyline measurements are shown in Figure 4.3. The instrument dispersions were approximated across the full wavelength range with a second-order Legendre polynomial,

$$c_0 + c_1 x + \frac{c_2}{2}\left(3x^2 - 1\right) \ , \tag{4.2}$$

with coefficients $(c_0, c_1, c_2) = (9.58294, -1.1229, 0.4273)$ and with $x = (\lambda - 6740.91)/262.98$ (i.e. $x \in (-1, 1)$ over the wavelength range considered). With this approximation, the instrument dispersion at $\lambda = 6822\,\text{Å}$ is $\sigma_{\text{inst}} = 9.1\,\text{km}\,\text{s}^{-1}$, or $0.487\,\text{Å}$ in terms of FWHM. We adopt this value as the spectral resolution of the SHαDE survey.

As a further test, we measure the arc emission lines after applying the wavelength solution, and find results consistent with the measurements from the sky emission lines. In principle, adding the spectra from different spaxels may artificially broaden the line-spread function, so that the instrument resolution measured from the co-added spectrum might be coarser than the resolution measured from individual spaxels. However, in practice, we find no systematic difference between the line widths measured from the co-added spectra or from individual spaxels (although the latter show larger dispersion, as expected from their lower overall SNR).

4.4.3.2 Sky subtraction

The sky subtraction was performed using the penalised pixel fitting algorithm (`pPXF`; Cappellari 2017). As sky templates, we used the spaxels within the ARGUS IFU further away from the target galaxy that belong to the lowest 5% of the distribution of Hα flux over the whole IFU footprint.

The quality of the sky subtraction is assessed by subtracting the best-fit sky from each of the sky spaxels. To avoid a trivial fit, for any given sky spectrum under consideration we remove it from the library of sky templates. The residuals are then computed as the difference between the observed sky spectrum and the best-fit sky. The distribution of the residuals is shown in Figure 4.4. This overall distribution is not Gaussian but is composed of residual distributions for individual galaxies that are Gaussian but with different standard deviations. We highlight the best case, with a standard deviation of 4.2 ADU (galaxy 1; green histogram in Figure 4.4), and the worst case, with a standard deviation of 9.4 ADU (galaxy 165; red histogram in Figure 4.4).

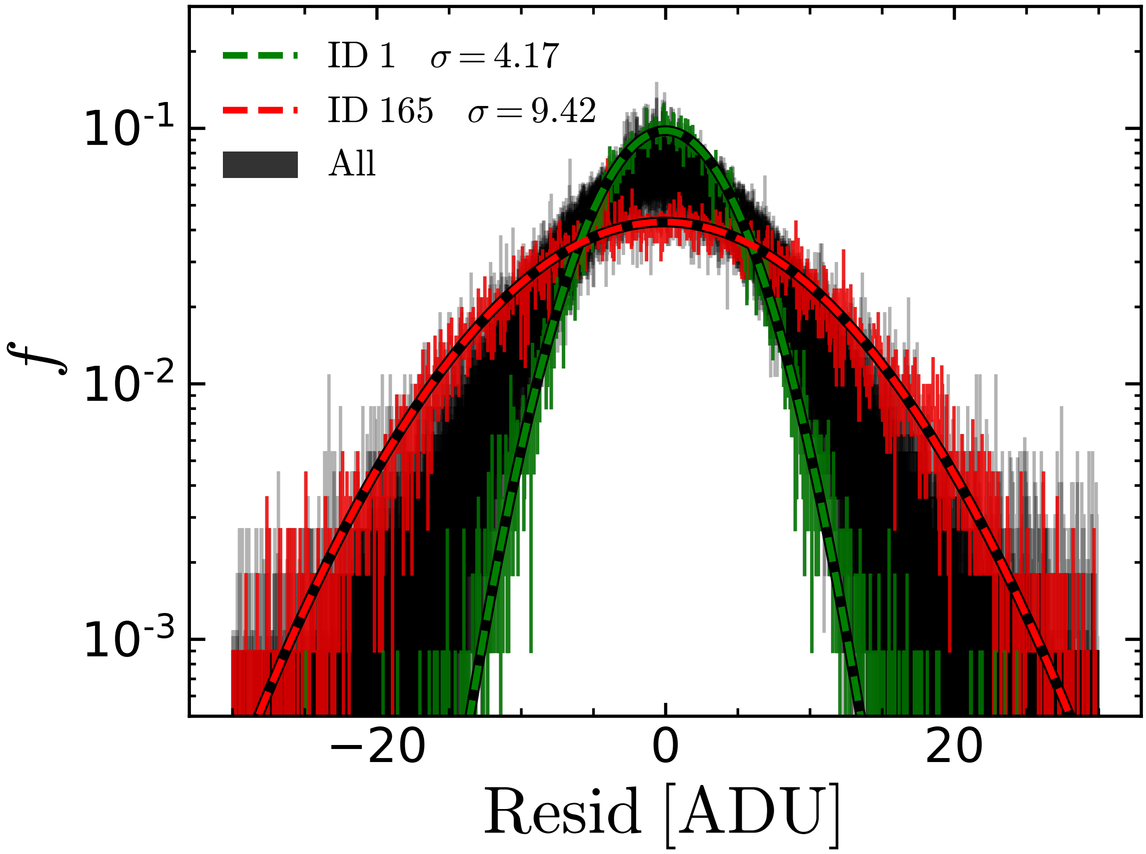

Figure 4.4: The distribution of sky subtraction residuals for each galaxy. The best and worst cases are highlighted in green and red (galaxy 1 and galaxy 165 respectively). The dashed lines show Gaussian distributions with zero mean and standard deviations from the associated distribution of residuals. The good match between these Gaussians and the histograms suggests that the sky residuals are normally distributed.

These two histograms are described very well by Gaussians with zero mean and standard deviation equal to standard deviation of the residuals for that galaxy. For each galaxy, we use test the null hypothesis that the residuals are drawn from a Gaussian using the Kolmogorov-Smirnov test. We adopt a generous significance treshold $p = 0.05$, yet find no galaxy exceeding this limit. For the two examples considered, we find a p-value of 0.99; the lowest p-value is 0.46 for galaxy 496.

4.4.4 Ancillary data

The ancillary data used in this study includes SDSS DR12 redshift (z) and within-fibre star formation rate densities ($\Sigma_{\rm SFR}$). The redshifts are emission-line based spectroscopic redshifts. The stellar mass ($M_\star$) was obtained from i-band magnitude and $g-i$ colour (Taylor et al. 2011), using the k-correction from Bryant et al. (2014). $\Sigma_{\rm SFR}$ was obtained from the extinction-corrected Hα luminosities, divided by the fibre area in physical units. Notice that, because of the Hα-flux selection criterion, the SHαDE sample might be biased to higher SFR than the average at its $M_\star$ (solid green line in Fig. 4.1b). Higher-than-average SFR cause bluer-than-average $g-i$ colour, which could bias our estimated $M_\star$, because this colour features directly in the expression of $M_\star$. To quantify this potential bias, we firstly measured the median $g-i$ colour of the SHαDE parent sample (i.e. the sample prior to any morphological or Hα-flux cut). This colour is 0.48 mag, and is indeed significantly redder than the median colour of the SHαDE sample (0.30 mag). If we replace the measured $g-i$ colour of the SHαDE galaxies with the median colour of the parent sample, we infer 0.13 dex higher $M_\star$. We remark that this bias is to be considered an upper limit, because it assumes that all the $i-$band light of the SHαDE galaxies is emitted from older stellar populations, as old as the median age of the parent sample, whereas, in reality, the stellar populations that dominate the $g-i$ colour also contribute (in part) to the $i-$band light.

For each galaxy, we used i-band SDSS DR12 photometry to measure the circularised half-light radius (R_e), the ellipticity (ϵ) and the position angle using a multi-Gaussian expansion (MGE, Emsellem et al. 1994; we use `mgefit`[1], the python implementation of Cappellari 2002). The method is described in D'Eugenio et al. (in prep.); here we briefly summarise the main steps. For each galaxy, we retrieve an image from the SDSS database that is 400 arcsec on a side and centred on the galaxy. We use `PSFEx` (Bertin 2011) to identify a set of unsaturated stars from which to measure the point spread

---

[1] Available in the Python Package Index (PyPI)

function (PSF). The local PSF is then modelled as a sum of two circular Gaussian functions and used as input to `mgefit`. R_e is calculated from the best-fit MGE model, following the definition of Cappellari (2002); ϵ is defined as the ellipticity of the model isophote of area πR_e^2.

Our photometric parameters are in excellent agreement with the measurements from the SAMI Survey, obtained using single-Sérsic profiles (Kelvin et al. 2012; Owers et al. 2017); the root mean square (rms) scatter between the MGE and Sérsic R_e measurements is 0.06 dex, implying a rms measurement uncertainty of 0.045 dex for both GAMA and MGE measurements if distributed equally (D'Eugenio et al. in prep.).

4.5 Data analysis

This work primarily focusses on the galaxy scaling relations of dwarf galaxies, especially the $\log M_\star - \log S_{0.5}$ relation. For this endeavour, the most important parameters are $V_{\rm rot}$ and σ. Since SHαDE is an IFS survey that offers us data cubes with a spectrum at every location within the FOV, we perform single-component emission-line fitting for the Hα, [NII] and [SII] lines. Then, from the spaxel-level kinematics, we calculate global $V_{\rm rot}$ and σ values. We also investigate the quality of the spaxel kinematics and look for any biases within them. The following subsections present the information extracted from the analysis in more detail.

4.5.1 Spaxel kinematics

IFS allows us to study the kinematics of gas and stars at each location (spaxel) within a galaxy. For SHαDE, galaxy gas kinematics are fitted using `pPXF`, and a set of Gaussian emission-line templates, consisting of the Hα line and the [NII] and [SII] forbidden lines. Each line is convolved with a Gaussian having standard deviation equal to the instrumental spectral resolution, with each continuum fitted with a linear interpolation.

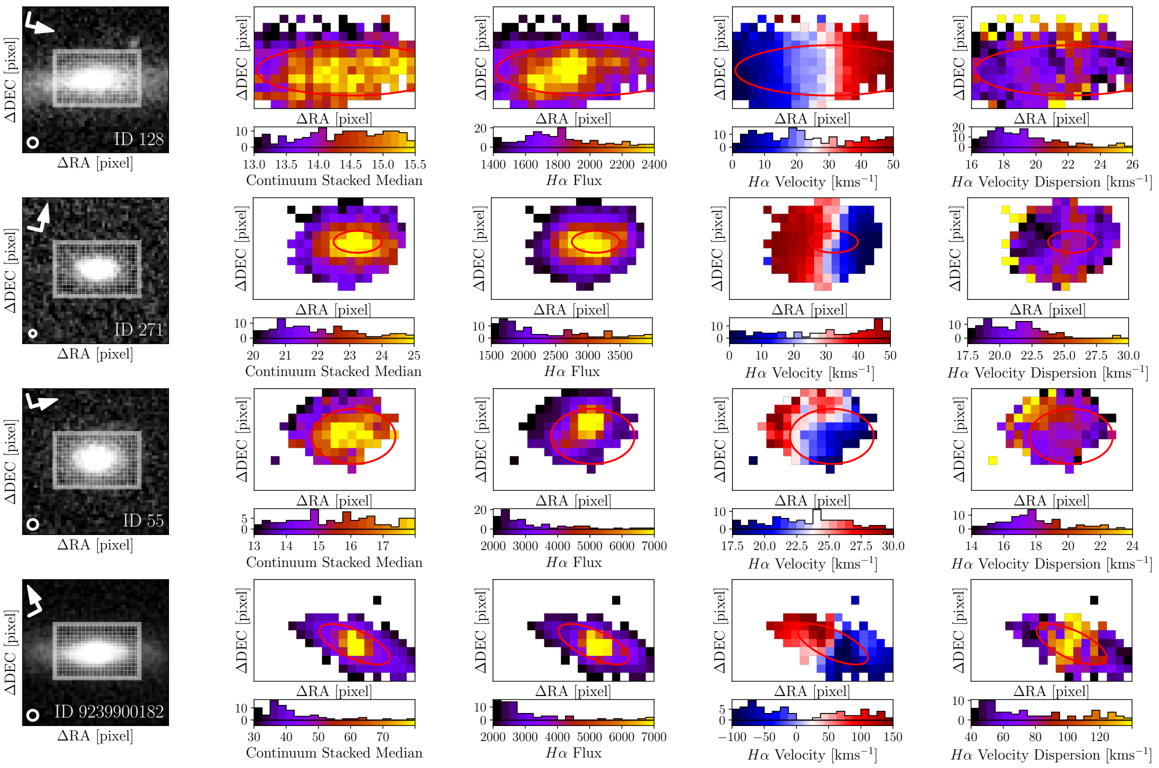

Figure 4.5: Example data from the SHαDE survey, spanning $0.003 \leq z \leq 0.055$ and $10^{7.43} \leq M_{\star} \leq 10^{10.60}\mathrm{M}_{\odot}$. From left to right: SDSS i-band image; Hα observed flux map; and Hα velocity and velocity dispersion maps. SDSS i-band images also show the FLAMES-ARGUS instrument target footprint on the galaxy with a grid representing the SHαDE spaxels; the small circles in the i-band images have diameter equal to the PSF FWHM in pixel units; each i-band image has been rotated to align the galaxy's position angle to the long axis of the ARGUS IFU (the North/East directions are indicated by the white arrow/short arm). Where there is misalignment, we use `mgefit` to measure the position angle from stacked continuum image for our spaxel sampling. The flux and kinematic maps only show spaxels with SNR > 5; each map also has an associated histogram showing the distribution of the observed quantity. The red ellipse in each SHαDE data map represents the sampling region inside $1R_e$.

We use the appropriate spectral resolution values at the wavelength positions of the emission lines from the interpolated Legendre function (see Section 4.4.3.1 and the dashed green line in Figure 4.3). In each iteration, `pPXF` creates a model spectrum by convolving the input templates with a trial velocity dispersion σ and applying a trial offset v: the best-fit σ_i and v_i are those that minimise the χ^2 of the residuals (subscript

i here runs over spaxels).

In this work, we use the Hα velocity dispersion measurements independently of the [NII] and [SII] forbidden-line measurements. However our Hα velocity dispersion measurements do not change if we constrain Hα to have the same kinematics as [NII] and [SII]. Figure 4.5 shows the SDSS photometry and Hα flux, velocity, and velocity dispersion maps for four example SHαDE galaxies. From the figure we can see that the SHαDE IFS maps clearly reveal the distributions of Hα flux, rotation velocity, and velocity dispersion in each galaxy.

We obtain the uncertainties in v_i and σ_i using a Monte Carlo approach. For each spaxel, we create 100 spectra by taking the best-fit spectral model and adding random noise. This noise is the residual between the best-fit model and the observed spectrum around the Hα line, shuffled in wavelength. We then run `pPXF` on each of these 100 realisations to estimate the rms uncertainties in the systemic velocities (Δv_i) and velocity dispersions ($\Delta\sigma_i$).

For each spaxel, we take the SNR of the Hα line to be

$$SNR = \frac{F}{\sqrt{N}\sigma_\lambda} \ , \tag{4.3}$$

where F is the integrated flux of the Hα line, N is the number of pixels the Hα line spans, and σ_λ is the standard deviation of the residual noise under the Hα line.

4.5.2 Systematic errors

Measuring accurate velocity dispersions is notoriously challenging; success depends on a combination of sufficient spectral resolution and SNR. In order to evaluate the possibility of a bias in our measurements of σ_i, we collect σ_i, $\Delta\sigma_i$, and SNR$_i$ measurements from all spaxels within an elliptical aperture for each galaxy. The apertures are defined by the half-light radius R_e, ellipticity ϵ, and position angle of the galaxies, see

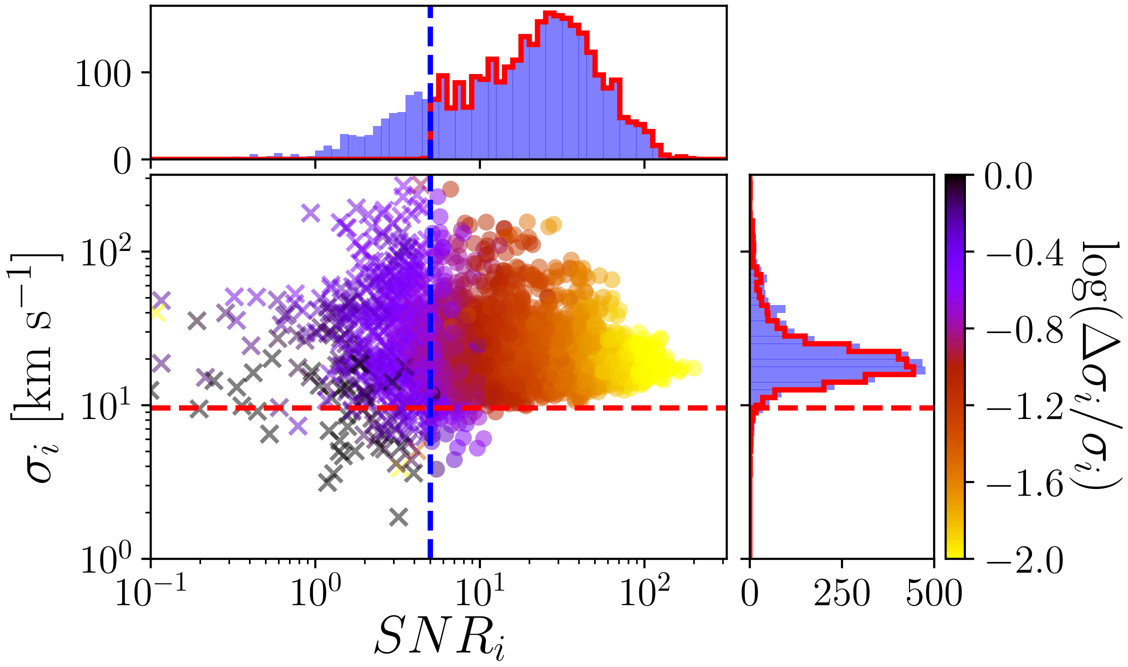

Figure 4.6: Velocity dispersion quality of all SHαDE galaxy spaxels and the effect of the SNR$_i$ >5 quality cut. The red dashed horizontal line shows the typical spectral resolution of 9.6 km s^{-1} and the blue dashed vertical line shows the quality cut we applied at SNR$_i$ >5. Circles and crosses are spaxels above and below the SNR cut respectively and spaxels are colour-coded by their relative uncertainties. The blue and red marginal histograms show the distribution of measurements before and after the quality cut, respectively. This plot shows that, with this SNR limit, our spaxel σ measurements show no obvious bias and the majority of spaxels have SNR$_i$ >10 and relative uncertainties in σ_i below 15%.

red ellipse in Figure 4.5 for example. For a few galaxies in our sample, there was misalignment between the IFU positioning and the galaxy position angle, for these cases we used `mgefit` to measure the position angle from stacked continuum images. Figure 4.6 shows the distribution of σ_i and SNR_i within these apertures for all SHαDE galaxies, colour-coded by the relative error $\log(\Delta\sigma_i/\sigma_i)$. The blue filled histograms in Figure 4.6 show that the σ_i measurements in our sample are approximately symmetric over the range $1.0 < \log\sigma_i < 1.5$ without any significant skew towards over- or under-estimation of velocity dispersion, but minor tail towards the high σ_i values. Moreover, 85% of spaxels have $\mathrm{SNR} \geq 5$, shown by the vertical dashed line; for our study, we keep all spaxels with $\mathrm{SNR}_i \geq 5$. A quality cut of $\mathrm{SNR}_i \geq 5$ results in more than three quarters of spaxels (78%) having $\log\Delta\sigma_i/\sigma_i \leq -1$. This SNR limit (corresponding to the red open histograms in both marginal distributions) does not introduce any bias in the $\log\sigma_i$ distribution. Note that the distribution of σ_i is peaked well above the instrumental spectral resolution, shown by the horizontal dashed line in the figure; the distribution implies we are resolving the internal motions for 92% of the spaxels in these galaxies. Our main findings do not change with a $\mathrm{SNR} \geq 10$ cut.

4.5.3 V_{rot} and σ measurements

To study various kinematic scaling relations, we measure the global V_{rot} and σ for each galaxy. For these, we follow the approach of Catinella et al. (2005) and Cortese et al. (2014) to remain consistent with B19. Here we provide a brief overview of the method; for more details see Section 2.2 of B19.

For the rotation velocity V_{rot}, we use the histogram technique where for each galaxy we measure the velocity width (W) between the 10th and 90th percentiles of the v_i distribution for spaxels within the $1R_e$ elliptical aperture and correct for inclination (i) and redshift (z). Following B19, we do not perform inclination corrections for nearly edge-on galaxies with (minor-to-major axes ratio) $b/a < 0.2$ and we exclude nearly face-on galaxies with $b/a > 0.95$.

For the velocity dispersion σ, we measure the root mean square velocity dispersion from all the spaxels within the $1R_e$ elliptical aperture, weighted by the continuum flux. It is worth noting that both $V_{\rm rot}$ and σ are calculated using only spaxels with SNR≥ 5. For the uncertainties in the global quantities, $\Delta V_{\rm rot}$ and $\Delta\sigma$ (as well as for $\Delta S_{0.5}$), we use a bootstrap method: we randomly pick the same number of spaxels as the total number within the aperture (allowing repetitions); we calculate $V_{\rm rot}$, σ and $S_{0.5}$ from these spaxels, as above; and we repeat this 1000 times, using the resulting standard deviations as $\Delta V_{\rm rot}$, $\Delta\sigma$ and $\Delta S_{0.5}$.

4.6 Scaling relations

After obtaining the $S_{0.5}$ kinematic parameter, we begin the analyses of kinematic scaling relations. As the SHαDE sample contains 20 galaxies that are in common with the SAMI survey, we first perform a comparison between SAMI and SHαDE kinematic measurements to determine if there is any systematic bias in any of samples. Then we construct the TF, FJ and the $\log M_\star$–$\log S_{0.5}$ scaling relations to investigate how dwarf galaxies behave on them. In this section we also compare the stellar and baryonic versions of the $\log M - \log S_{0.5}$ scaling relation.

4.6.1 Comparing SHαDE and SAMI kinematics

After obtaining the gas kinematics of the SHαDE galaxies, we compare our measurements with those from the SAMI survey. Of the 69 galaxies observed in SHADE, 20 overlap with the SAMI galaxy sample. These galaxies in common are chosen from the SAMI $\log M_\star$–$\log S_{0.5}$ scaling relation (B19) to be the control sample (see Section 4.4.1). The control sample has a mass range from $10^{8.6} M_\odot$ to $10^{10.6} M_\odot$. Because accuracy in velocity dispersion measurements is crucial in our study, these independent

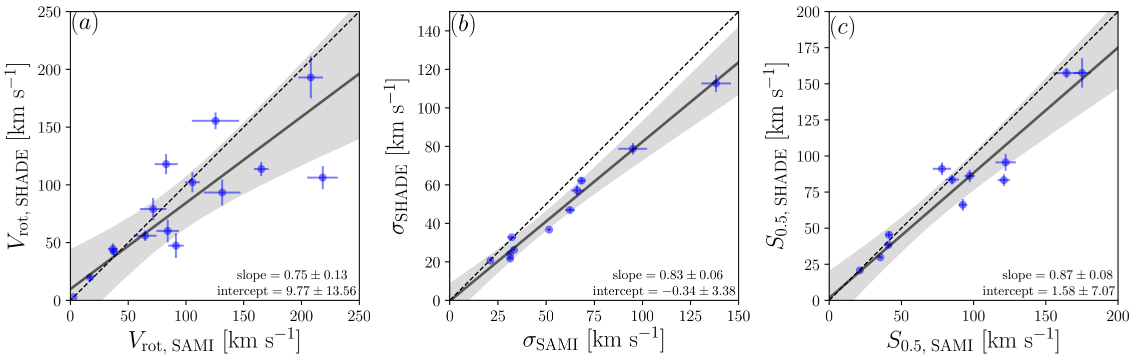

Figure 4.7: Comparing SAMI and SHαDE kinematic parameters for the control sample. The dashed lines are one-to-one relations, the solid lines are the linear best fits to the paired quantities, with the shaded region indicating the 99% confidence interval in the quantity on the vertical axis given the uncertainties in the fitted slope and intercept. The measured σ values are lower for SHαDE than SAMI while $V_{\rm rot}$ and $S_{0.5}$ are consistent between SHαDE and SAMI.

measurements of velocity dispersion for the same galaxies provide a critical test of the systematics associated with each survey.

We compare SAMI and SHαDE measurements of $V_{\rm rot}$, σ, and $S_{0.5}$ parameters in Figure 4.7. For each plot, we kept only galaxies with $\Delta V_{\rm rot}/V_{\rm rot} < 0.2$, $\Delta\sigma/\sigma < 0.1$, and $\Delta S_{0.5}/S_{0.5} < 0.1$ respectively. Separate relative error thresholds are chosen to ensure an adequate number of galaxies over sufficient range of values remain in the comparison, while rejecting outliers. The fit parameters in each plot indicate that SHαDE velocity dispersions are consistently lower than SAMI velocity dispersion. This can be explained by a combination of two improvements: firstly, the spectral resolution of SHαDE (9.6 km s^{-1}; Section 4.4.3.1) is three times better than SAMI (29.9 km s^{-1}; van de Sande et al. 2017), and secondly the spatial resolution of SHαDE is also better, which combined with the improved seeing condition for the SHαDE observations, mitigates the effect of beam smearing (see Section 4.4.2). The difference between the SHαDE and SAMI velocity dispersions is not highly significant ($\sim 2.8\sigma$) and, when combined with the rotation velocity, the $S_{0.5}$ measurements have an insignificant ($\sim 1.6\sigma$) difference.

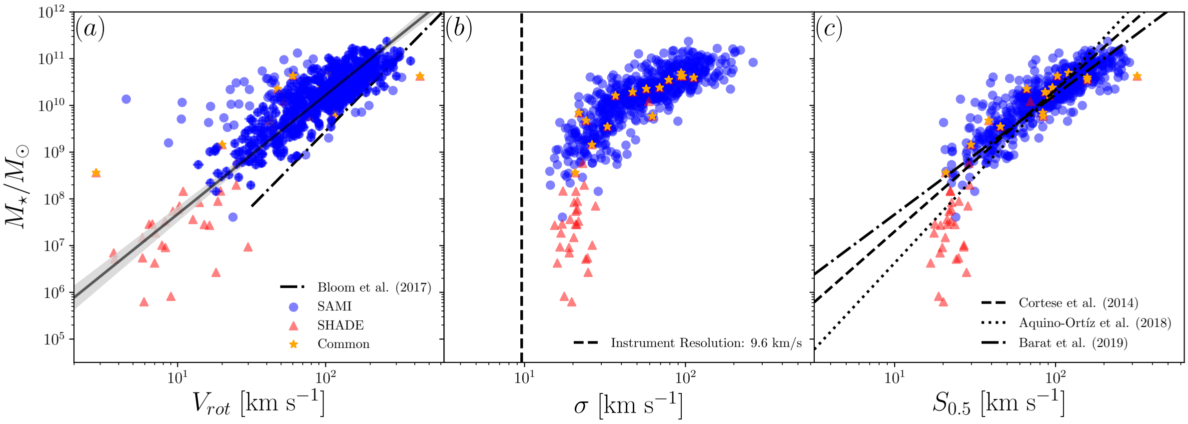

Figure 4.8: SAMI and SHαDE Tully-Fisher (TF), Faber-Jackson (FJ), and $S_{0.5}$ scaling relations. Blue circles represent SAMI measurements, red triangles represent SHαDE measurements, and yellow stars represent SHαDE measurements of the control sample from SAMI. In the TF relation shown in panel (a), the SHαDE sample in general follows the same relation (solid line) as the SAMI sample. The shaded region in panel (a) represents the 99% confidence interval in the vertical axis given the uncertainties in the fitted slope and intercept. The combined TF relation is flatter than that obtained by Bloom et al. (2017b). The FJ relation in panel (b) shows a clear bend and a lower limit for the σ measurements above the spectral resolution limit of the SHαDE observations (shown by the vertical dashed line). The bend in the FJ relation carries across to the $S_{0.5}$ scaling relation in panel (c). Best-fit lines from Barat et al. (2019); Aquino-Ortíz et al. (2018); Cortese et al. (2014) are included for comparison in panel (c).

This concordance demonstrates the robustness of the $S_{0.5}$ kinematic parameter against atmospheric seeing.

4.6.2 Kinematics scaling relations of dwarf galaxies

We extend the kinematic scaling relation studies of Cortese et al. (2014), Aquino-Ortíz et al. (2018) and B19 to dwarf galaxies by combining SHαDE data and SAMI data from B19 to construct the stellar mass TF, FJ and $S_{0.5}$ kinematic scaling relations over the mass range $10^{5.7} < M_\star < 10^{11.4}\mathrm{M}_\odot$. As we have shown in Section 4.6.1, the SHαDE $V_{\rm rot}$, σ, and $S_{0.5}$ measurements are in good correlation with those measured from SAMI data for the control (higher-mass) sample, with small scatter and slight offset. Given this agreement, it is not surprising that the scaling relations from SHαDE connect well with SAMI scaling relations without any obvious offset, as shown in Figure 4.8. The SHαDE measurements for the control sample (star symbols in Figure 4.8) lie within the SAMI sample distribution in each scaling relation, so there is no need to calibrate the SHαDE and SAMI scaling relations (and indeed our results do not change if we calibrate the kinematic measurements using the results from Section 4.6.1).

The extended TF relation and the best fit (solid) line to the SAMI sample in Figure 4.8a show that the dwarf galaxies in SHαDE follow the SAMI TF relation, albeit with greater scatter; fitting both samples simultaneously produces the same line within the uncertainties. For comparison, we included the best fit (dot-dashed) line from Bloom et al. (2017b), which also uses SAMI data. Our TF relation only agrees with Bloom et al. (2017b) at high masses ($M_\star > 10^{10} M_\odot$). This difference is due to different sampling regions of the galaxies in the two studies: in Bloom et al. (2017b), V_{rot} is measured from regions out to $2.2R_e$, whereas we sample within $1R_e$. Therefore our results only agree for high-mass galaxies with steep rotation curves, where maximum rotation velocities can occur within $1R_e$ (Yegorova & Salucci 2007).

One of the main motivations of this study is to observe galaxies with σ below the spectral resolution of SAMI ($\sim$30 $\mathrm{km\,s^{-1}}$) with higher resolution and so to constrain the FJ and $S_{0.5}$ scaling relations for low-mass galaxies. Our results in Figure 4.8b show that, despite having an instrumental resolution of 9.6 $\mathrm{km\,s^{-1}}$, low-mass dwarf galaxies in SHαDE do not reach velocity dispersion below $\sim$15 $\mathrm{km\,s^{-1}}$; i.e. the distribution of velocity dispersions in these galaxies has a physical (not instrumental) lower limit. For low-mass SHαDE galaxies with $M_\star \lesssim 10^8\,\mathrm{M}_\odot$ (i.e. excluding the control sample), the mean velocity dispersion in galaxies is 22$\pm$5 $\mathrm{km\,s^{-1}}$. While we acknowledge, based on Figure 4.6, that there are number of spaxels ($\sim$30) across the SHαDE galaxy population with have $\sigma_i > 100$ $\mathrm{km\,s^{-1}}$, these do not introduce a sufficient bias to result in the σ

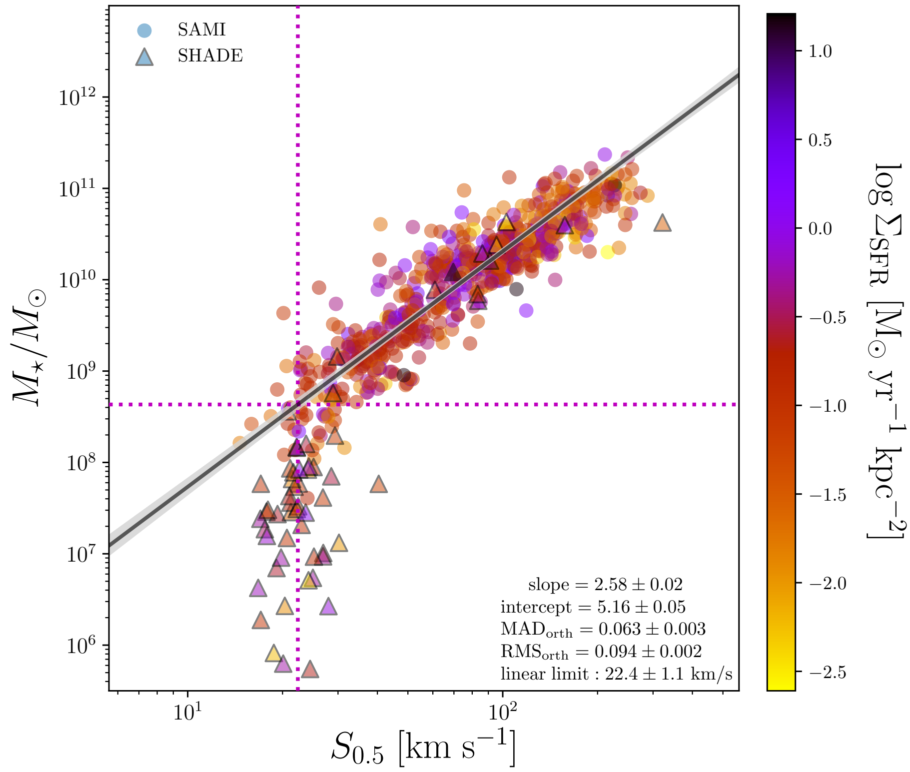

Figure 4.9: $\log M_\star$–$\log S_{0.5}$ scaling relation from combining the SAMI and SHαDE samples. Round points are SAMI measurements; triangular points are SHαDE measurements; all points are colour-coded by gas surface density. The black solid line is the best fit and the shaded region represents the 99% confidence interval in the vertical axis given the uncertainties in the fitted slope and intercept. Magenta horizontal and vertical lines indicate the limit of the linear fit; below this mass threshold, points are modelled as normally distributed around the vertical line.

floor observed in Figure 4.8b.

The lower limit for σ propagates to the $S_{0.5}$ scaling relation in Figure 4.8c. All SHαDE galaxies (apart from the control sample), lie beneath the best-fit line for the SAMI sample from B19. This confirms the bend in the gas $S_{0.5}$ scaling relation observed in B19 and suggests that a linear relation is not adequate to describe the $\log M_\star$–$\log S_{0.5}$ scaling relation. The exact location of the bend and its implications are discussed in the following section.

4.6.3 A closer look at the $S_{0.5}$ scaling relation

Using the combined SAMI and SHαDE galaxy sample, we construct the $\log M_\star$–$\log S_{0.5}$ scaling relation in Figure 4.9. In order to assess the presence of a bend in the scaling relation we adopted a Bayesian approach. We model the data as a mixture of a line with Gaussian scatter above some mass threshold $\log M_{\star,\mathrm{lim}}$ (corresponding to $\log S_{0.5,\mathrm{lim}}$ on the scaling relation) and below this mass threshold the $\log S_{0.5}$ values are distributed as a Gaussian about $\log S_{0.5,\mathrm{lim}}$ (i.e. $\log M_\star$ is not determined by $\log S_{0.5}$ for masses below $\log M_{\star,\mathrm{lim}}$). We adopt flat, uninformative priors on all the fitting parameters: the slope and intercept of the linear relation, the Gaussian scatter about the linear relation ($\log M_\star > \log M_{\star,\mathrm{lim}}$), and the Gaussian scatter about $\log S_{0.5,\mathrm{lim}}$ ($\log M_\star < \log M_{\star,\mathrm{lim}}$) and the mass threshold itself. We estimate the posterior distribution using a Markov Chain Monte Carlo approach (Metropolis et al. 1953; for details see B19, Section 3.2.1). We take the model with the maximum log likelihood to be the best-fit model. The model fitting results are shown in Table 3.2. The slope and the intercept are not affected by the addition of dwarf galaxies, because they are the same values we obtained in B19 using only SAMI galaxies (their Table 2, sample B1, c.f. slope of 2.56 ± 0.01, intercept 5.10 ± 0.05 after inversion for consistency). The linear limit fitted to the combined SAMI+SHαDE data is $S_{0.5,\mathrm{lim}} = 22.4 \pm 1.1\ \mathrm{km\,s^{-1}}$, corresponding to a stellar mass limit $M_{\star,\mathrm{lim}} = 10^{8.6}\mathrm{M}_\odot$, and is consistent with that of B19 (c.f. $S_{0.5,\mathrm{lim}} = 22.4 \pm 1.0\ \mathrm{km\,s^{-1}}$). This is interesting because, although a bend in the scaling relation was observed in B19, we could not rule out the possibility that it was an observational artefact, as the limit ($22\ \mathrm{km\,s^{-1}}$) was slightly less than the spectral resolution limit of the SAMI instrument ($30\ \mathrm{km\,s^{-1}}$). However this is definitely not the case for SHαDE data, which was observed with a spectral resolution of $9.6\ \mathrm{km\,s^{-1}}$; the fitted limit at $22\ \mathrm{km\,s^{-1}}$is more than twice the SHαDE instrumental resolution and so would appear to be physical. On the other hand, the bend observed by B19 at about $60\ \mathrm{km\,s^{-1}}$in the *stellar* scaling relation (as opposed to this *gas* scaling relation) may still be an artefact due to the

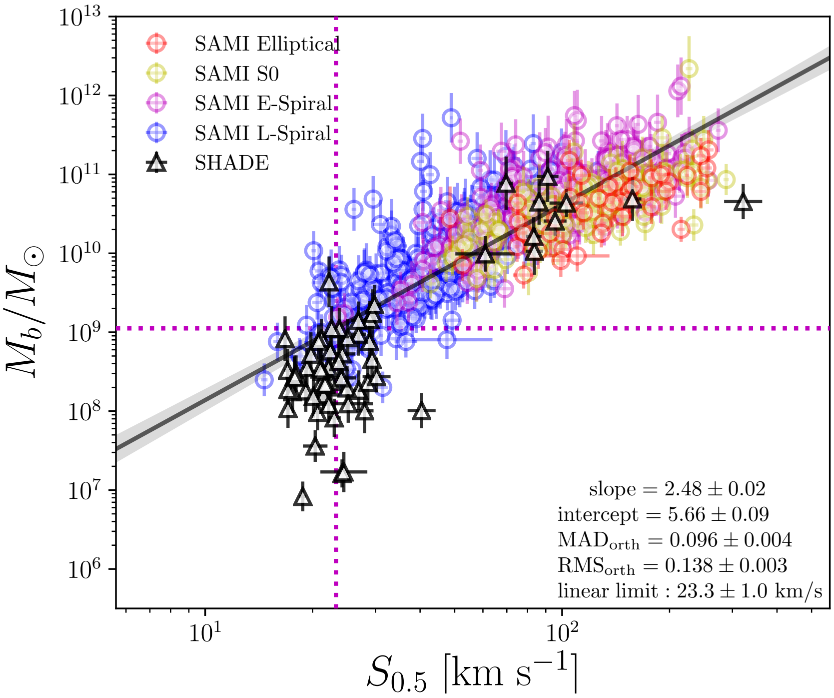

Figure 4.10: The baryonic version of the $\log M_\star$–$\log S_{0.5}$ scaling relation from combining the SAMI and SHαDE samples. Round points are SAMI measurements; triangles are SHαDE measurements. The molecular and atomic gas mass is estimated based on Kennicutt (1998). SAMI galaxies are colour-coded by their visual morphologies as elliptical, S0, early-spiral or late-spiral. It is apparent the approximated baryonic scaling relation significantly reduce the bend in the scaling relation.

SAMI instrumental resolution limit, which for stars was about 70 km s^{-1}. It is very unlikely that the observed bend is due to bias in the determination of $M_\star$ because, along the direction of $M_\star$, SHαDE galaxies are offset from the linear relation by 1 dex or more; in contrast, we estimate the bias in $M_\star$ to be $\lesssim 0.13$ dex (Section 4.4.4).

4.6.4 Baryonic $\log M_b$–$\log S_{0.5}$ scaling relation

The $\log M_\star$–$\log S_{0.5}$ scaling relation follows from the virial theorem if $M_\star$ is a fixed fraction of the total mass $M_{\rm total}$. However, if the $M_\star/M_{\rm total}$ ratio varies due to an

Table 4.4: Scaling relation fitting results from this work and B19.

Source	Y	Slope	Intercept	$S_{0.5,\mathrm{lim}}$ $\mathrm{km\,s^{-1}}$	Y_{lim} $M_\odot$	Scatter MAD$_{\mathrm{orth}}$
Figure 4.9	$M_\star$	2.58 ± 0.02	5.16 ± 0.05	22.4 ± 1.1	$10^{8.64}$	0.063 ± 0.003
Figure 4.10	M_b	2.48 ± 0.02	5.66 ± 0.09	23.3 ± 1.0	$10^{9.05}$	0.096 ± 0.004
Figure 4.13	M_h	2.22 ± 0.07	7.84 ± 0.75	-	-	-
B19*	$M_\star$	2.56 ± 0.01	5.10 ± 0.05	22.4 ± 1.0	$10^{8.56}$	0.063 ± 0.003

* inverted

increased gas fraction in lower mass galaxies (as expected over our wide mass range; see Foucaud et al. 2010), this will introduce a curvature in the $\log M_\star$–$\log S_{0.5}$ relation. To improve the coupling with M_{total}, therefore, it is in principle better to include the gas mass by using baryonic mass M_b rather than stellar mass $M_\star$. However, due to the lack of direct HI observations for SHαDE galaxies, we have to construct the $\log M_b$–$\log S_{0.5}$ scaling relation by summing the stellar mass with an approximate estimate of the gas mass, which we derive for each SAMI and SHαDE galaxy from its star formation rate (SFR) as follows. The SFR is obtained from SDSS where available (see Section 4.4.4) and converted to SFR surface density (Σ_{SFR}) by dividing by the SDSS fibre aperture in kpc^2 at the redshift of the galaxy. From Σ_{SFR}, we then estimate the surface density of neutral and molecular hydrogen gas (Σ_{gas}) by inverting the star formation law (Kennicutt 1998), described by:

$$\Sigma_{\mathrm{SFR}} = (2.5 \pm 0.7) \times 10^{-4} \left(\frac{\Sigma_{\mathrm{gas}}}{\mathrm{M_\odot\,pc^{-2}}} \right)^{1.4\pm0.15} \mathrm{M_\odot\,yr^{-1}\,kpc^{-2}}\,. \tag{4.4}$$

We also explored other, more recent, variants of the star formation law, namely those of Federrath et al. (2017) and de los Reyes & Kennicutt (2019). However the Federrath et al. (2017) relation only estimates cold molecular gas while the de los Reyes & Kennicutt (2019) uses UV-based estimation, requiring a conversion and thus introducing additional uncertainties and systematics. We therefore choose to employ the original star formation law from Kennicutt (1998), which relates HI and CO densities to Hα

SFRs.

Once we have obtained Σ_{gas}, we multiply this gas surface density by the projected area of the galaxy defined by R_e (in kpc^2) and ellipticity to obtain the gas mass M_{gas}, which we sum with $M_\star$ to get the estimated total baryonic mass M_b. For the uncertainties in our M_b measurements, we use the uncertainties in Equation 4.4 and perform Monte Carlo sampling 1000 times. This provides a distribution of M_b for each galaxy and we take the standard deviations as uncertainties.

Figure 4.10 shows the baryonic version of the $S_{0.5}$ scaling relation, with M_b obtained using Equation 4.4. The fitting results are shown in Table 3.2. Comparing Figure 4.9 and Figure 4.10, we can see that the inclusion of an M_{gas} estimate reduces the extent of the bend in the relation at low masses: the ratio between $M_{\star,\mathrm{lim}}$ and the observed stellar mass is more than two orders of magnitude in Figure 4.9, whereas, for M_b, the corresponding ratio is approximately one order of magnitude (Figure 4.10). This improvement is achieved by compressing the baryonic mass for dwarf galaxies at the expense of increased scatter at all masses. There is significant overlap between SHαDE and SAMI galaxies in the $\log M_b$–$\log S_{0.5}$ relation over the range 10^8–$10^9\,\mathrm{M}_\odot$, with very few galaxies remaining below $10^7\,\mathrm{M}_\odot$. While the intercept and the scatter of the scaling relation increased as expected, since more mass (and uncertainty) is added, the slope of the relation remains approximately the same (within one standard deviation). Although visually the bend in $\log M_b$–$\log S_{0.5}$ has been reduced by the addition of the gas mass, the linear-regime limit from the model fits indicates that the bend is still present. This suggests that using baryonic mass in dwarf galaxies is still not sufficient to account for their gas kinematics, in contrast to their higher mass ($M_b > 10^{10}\,\mathrm{M}_\odot$) counterparts. Moreover, we note that, compared to the stellar mass scaling relation, the baryonic mass scaling relation appears to flatten out at masses $M_b > 10^{11}\,\mathrm{M}_\odot$, which could be due to the inapplicability of the star formation law at the high-mass end the of the scaling relation, where the hydrogen gas converts from atomic to molecular form

(Bigiel et al. 2008).

4.7 Discussion

In this section we discuss our findings regarding the $\log M_\star$–$\log S_{0.5}$ scaling relation, especially the observed lower limit on σ. We look at the range over which the $\log M_\star$–$\log S_{0.5}$ scaling relation remains linear and the location where the relation bends and becomes steeper. We explore the halo mass version of the scaling relation by taking some simple assumptions. Finally we compare our observed lower limit on σ to those in the literature and note several possible drivers for the observed limit.

4.7.1 Limitations of the $S_{0.5}$ scaling relation

The purpose of constructing the $\log M_\star$–$\log S_{0.5}$ relation is to combine $V_{\rm rot}$ and σ into a single kinematic parameter that allows star-forming and quiescent galaxies to be put on a common mass–kinematics scaling relation that is tighter than the stellar mass TF relation and has slope and intercept close to the FJ relation. Cortese et al. (2014) demonstrated that galaxies of all morphologies can be brought onto the same $\log M_\star$–$\log S_{0.5}$ scaling relation; this was confirmed by Aquino-Ortíz et al. (2018) and Gilhuly et al. (2019) using the CALIFA survey and by B19 using a larger SAMI data set. While these findings pointed towards $S_{0.5}$ possibly providing a universal mass proxy, B19 also showed that there existed an apparent bend in both the gas and the stellar versions of the scaling relation at low masses. However, due to limitations in the S/N ratio, the instrumental resolution, and the sample selection, as well as the fact that the bend occurred at different stellar masses for the gas and stellar scaling relations, the apparent bends found by B19 were arguably observational artefacts.

The SHαDE survey is partly motivated by the question of whether there is a physical component to the low-mass bend in the $\log M_\star$–$\log S_{0.5}$ scaling relation. By observing

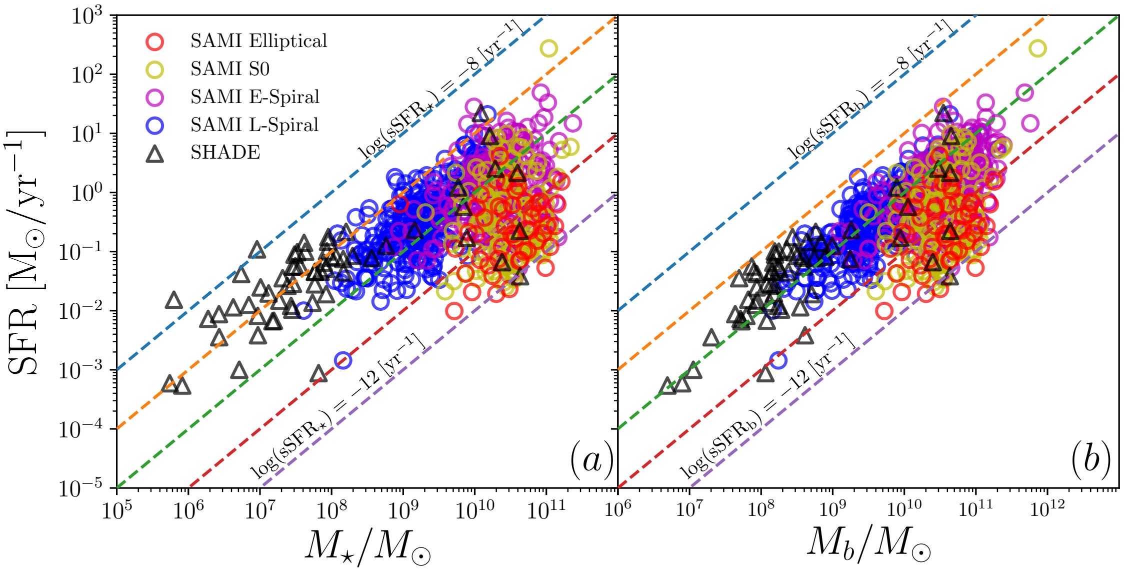

Figure 4.11: The star-forming sequence of the combined SAMI and SHαDE sample. Panel (a) shows SFR as a function of stellar mass; the dashed lines indicate specific SFR (sSFR$_\star$) in the range $[10^{-8}, 10^{-12}]\,\mathrm{yr}^{-1}$, where sSFR$_\star$ is SFR divided by stellar mass. Panel (b) shows the SFR as a function of baryonic mass; the dashed lines indicate sSFR$_b$ (SFR divided by baryonic mass). The marker shapes and colour scheme are the same as in Figure 4.10. Comparing panels (a) and (b) shows that dwarf galaxies have higher sSFR$_\star$ than more massive galaxies, but that this difference largely disappears for sSFR$_b$.

the Hα kinematics of low-mass dwarf galaxies using a high spectral resolution instrument, the results from this work show that there does indeed exist a physical limit where the *gas* version of the $\log M_\star$–$\log S_{0.5}$ scaling relation no longer follows a linear trend.

We have also seen that the linearity limit in the scaling relation is very close to the floor in σ measurements at ∼20 $\mathrm{km\,s^{-1}}$, while V_{rot} within $1R_e$ had very little contribution. Looking at the TF relation obtained in Figure 4.8a, dwarf galaxies do not significantly deviate from the the TF relation formed by more massive galaxies. This suggests that, depending on the difference in the steepness of the rotation curves and the difference in maximum rotation velocities between massive galaxies and dwarf galaxies, measuring rotation velocities at radii beyond one effective radius could possibly increase the contribution of $V_{\rm rot}$ in the $S_{0.5}$ parameter. In fact, in Figure 4.8a we can see that the TF relation from Bloom et al. (2017b) measured at $2.2R_e$ shows an offset from the TF relation measured at $1R_e$. By observing over a larger area, it is likely the limit of $S_{0.5}$ will shift away from the σ floor and potentially decrease the bend in the scaling relation. The role of aperture size will be investigated in future work.

To assess whether dwarf galaxies can be brought onto the linear $\log M_\star$–$\log S_{0.5}$ scaling relation of more massive galaxies, we constructed the baryonic version of the scaling relation. Accounting for the gas mass derived from the star formation rate (SFR) significantly increased the scatter of the relation, but also substantially reduced the severity of the low-mass bend in the scaling relation (though it did not eliminate it). We therefore take a closer look at the star-forming sequence of SAMI and SHαDE galaxies. In Figure 4.11, we plot galaxy SFR against $M_\star$ and M_b, and overlay contours of specific SFR (sSFR). Note that in Figure 4.12a, sSFR$_\star$ is defined as the ratio of SFR to $M_\star$; in Figure 4.12b, sSFR$_b$ is defined as the ratio of SFR to M_b. We can see in Figure 4.12a that dwarf galaxies reside at or above sSFR$_\star = 10^{-9}\,{\rm yr}^{-1}$, while more massive star-forming galaxies in SAMI have sSFR$_\star$ below this value. This offset in sSFR$_\star$ disappears if instead we use sSFR$_b$. In Figure 4.12b, all dwarf galaxies have migrated below the sSFR$_{\rm b} = 10^{-9}\,{\rm yr}^{-1}$ line and there are no galaxies of any mass observed above this value of sSFR$_b$. Note that we refrain from calling sSFR$_{\rm b} = 10^{-9}\,{\rm yr}^{-1}$ an upper limit to the specific star formation rate, because the comparison contains (by construction) an internal correlation between the SFR and M_b; we only use this comparison to showcase the consistency between dwarf galaxies and high-mass star-forming galaxies. This suggests that when low-mass galaxies ($M_\star < 10^9\,{\rm M}_\odot$) are to be included in the scaling relation, M_b is a better proxy than $M_\star$ for dynamical mass across the transition in dynamical regime from star-dominated to gas-dominated galaxies.

4.7.1.1 Caveats regarding gas mass estimations

While ideally direct measurements of the HI gas mass are required for an observational construction of the baryonic $\log M_b$–$\log S_{0.5}$ scaling relation, in the absence such observations, we have used gas masses estimated using indirect relations given in the literature. A caveat regarding the gas mass calculation is that, as well as assuming the same star formation law for the entire sample, the gas mass is estimated within 1 R_e. This introduces an aperture bias in the sense that galaxies with extended gas distributions will have their gas mass, and consequently their M_b, under-estimated (Thomas et al. 2004). On the other hand, one of the criteria in SHαDE sample selection requires the galaxies to have high Hα flux (specifically, $f_{\mathrm{H}\alpha} > 5 \times 10^{-16}[\mathrm{erg\,s^{-1}\,cm^{-2}\,\mathring{A}^{-1}\,arcsec^{-2}}]$), This introduces a SFR bias that we have seen in Figure 4.12a. Using SFR to estimate the gas mass means the bias in SFR will lead to an over-estimation of the gas mass, and consequently an over-estimation of M_b. Without additional observations, it is difficult to quantify the combined effect of over-estimation of M_b due to high Hα flux sample, and under-estimation of M_b due to aperture bias. Therefore it will be important to avoid such estimation in future by pursuing a more accurate baryonic mass measurement through direct HI observations of low-baryonic-mass galaxies to fully test the linearity of the scaling relation.

4.7.2 The effect of halo mass M_h

In the standard CDM paradigm, the formation and kinematics of galaxies are under the influence of their dark matter halos. We cannot directly probe the dark matter independently of galaxy kinematics. However, we can use simple empirical baryon-to-halo mass relations from the literature, under reasonable assumptions, to estimate the dark matter halo masses (M_h). One such relation is given by Moster et al. (2010, their Equation 2), linking observed galaxy stellar mass with simulated halo mass using abundance matching. In that work, the stellar-to-halo mass relation is inferred for

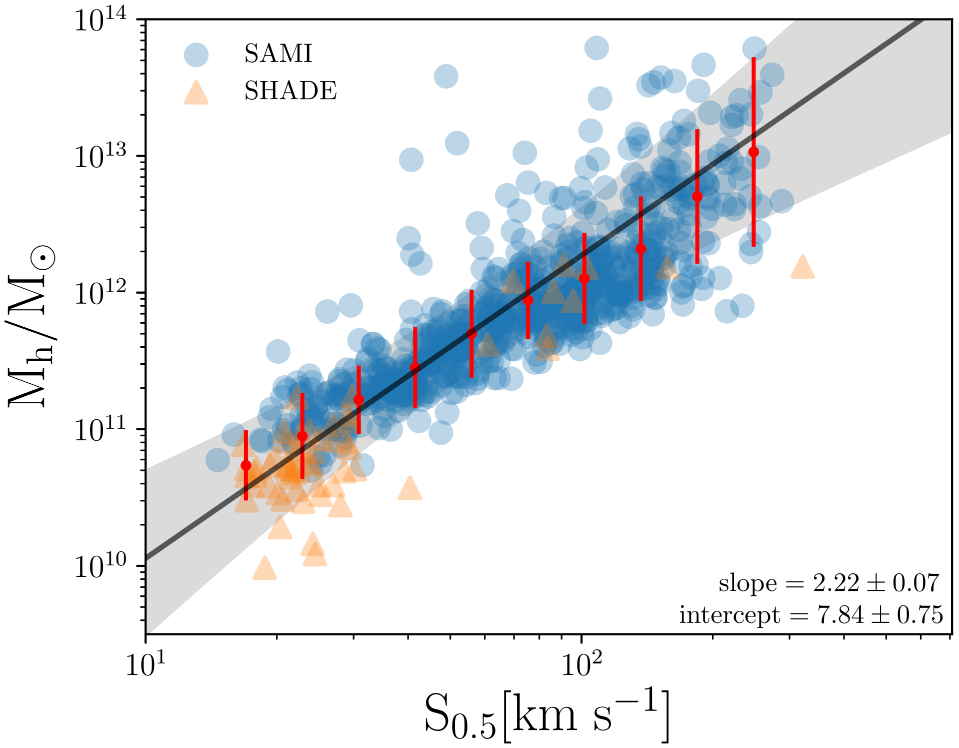

Figure 4.13: Halo mass version of the kinematic scaling relation. We estimate the halo mass of our sample by assuming a baryon-to-halo mass relation. The red points and error bars show the mean and standard deviation for the points in bins of $S_{0.5}$. We perform a linear regression (black solid line) to the binned values, with the shaded region representing the 3σ range of the best-fit line. The slope and intercept of the inverse fit with M_h as independent variable is given in the figure. We can see that, compared with the stellar mass and baryonic mass versions, although there is an increase of scatter at high masses (10^{12}–$10^{13}\,M_\odot$), the curvature in the scaling relation is greatly reduced.

galaxies with masses $10^9 < M_\star < 10^{12}\,M_\odot$. As we have seen, the baryonic mass in such high-mass galaxies tends to be star-dominated, while low-mass galaxies have higher gas content. Therefore, we assume that the stellar-to-halo mass relation in Moster et al. (2010) is a good approximation of the baryonic-mass-to-halo mass relation, and that it can be applied to dwarf galaxies with $M_\star < 10^9\,M_\odot$ and so provide halo mass estimates for our whole sample[1].

---

[1] Fits from Table 2 of Moster et al. (2010), including the effect of scatter.

Figure 4.13 shows the result of interpreting the stellar-to-halo mass ratio given by the relation of Moster et al. (2010) as baryon-to-halo mass ratio and constructing the $\log M_h$–$\log S_{0.5}$ scaling relation. We can see from the figure that, with this estimate of halo mass, the low-mass bend in the scaling relation has almost entirely disappeared. Moreover, the slight curvature of the $\log M_b$–$\log S_{0.5}$ relation at the high-mass end has also largely disappeared. Since we have made a number of assumptions, such as the applicability of the star formation law to early-type galaxies and the equivalence of the stellar-to-halo mass and baryon-to-halo mass relations, there is considerable systematic uncertainty in this figure and less constraint on systematic and sample biases in the resulting $\log M_h$–$\log S_{0.5}$ relation than the original $\log M_\star$–$\log S_{0.5}$ relation. To fit this relation, therefore, we perform a linear regression on the mean values in bins of $S_{0.5}$, shown as the red points in Figure 4.13 (although findings remain the same if we perform the fitting on the unbinned data). The fitting results are shown in the figure as well as Table 4.4.

The fact that the $\log M_h$–$\log S_{0.5}$ relation has the least amount of curvature over the range from giant to dwarf galaxies suggests that the estimated halo mass, rather than the stellar or baryonic mass, might be the most consistent quantity to use in a scaling relation that aims to unify galaxies of all morphologies. This suggests that the baryon-to-halo mass relation we have used conveniently captures the transition between gas-dominated, star-forming dwarf galaxies and dark-matter-dominated, quiescent massive galaxies. The reason why kinematics within one (optical) effective radius can successfully predict the halo mass remains to be explained, although it has been reported that total density profiles are almost isothermal (Cappellari et al. 2015; Poci et al. 2017). It is also worth noting that the $\log M_h$–$\log S_{0.5}$ relation has a slope that is closest to the virial prediction $M \propto V_c^2$, in contrast to $\log M_\star$–$\log S_{0.5}$ and $\log M_b$–$\log S_{0.5}$ (see Table 4.4). These findings underline the importance of dark matter halo mass in the construction of a unified galaxy kinematic scaling relation.

It should be noted that while M_h shows promising potential in rectifying the bend in the unified scaling relation, this result relies on quite a few significant assumptions. Direction HI observations are therefore essential for a proper test of these speculative conclusions.

Even though adding extra mass (both baryonic and dark matter) reduced the bend at low masses in the $\log M_h$–$\log S_{0.5}$ relation, there is still a lower limit to the observed gas velocity dispersion. This limit occurs just at the mass range where the gas fraction in galaxies increases substantially. Understanding the driver of this lower limit to the gas velocity dispersion is important for understanding the formation and structure of low-mass dwarf galaxies.

4.7.3 The lower limits of σ and $S_{0.5}$

As the bend in the $\log M_\star$–$\log S_{0.5}$ scaling relation originates from the observed lower limit for σ in the FJ relation, identifying the driver(s) behind σ in low-mass dwarf galaxies is crucial to understanding the limitation of the $\log M_\star$–$\log S_{0.5}$ scaling relation.

Similar lower limits for σ have been observed for HI gas at around 10 $\mathrm{km\,s^{-1}}$ (Ianjamasimanana et al. 2012) and at around 20 $\mathrm{km\,s^{-1}}$for Hα gas (Moiseev et al. 2015). Most recently, Varidel et al. (2020) found that low-redshift star-forming galaxies from SAMI have $14.1 < \sigma < 22.1$ $\mathrm{km\,s^{-1}}$. Theoretical models also predict that the σ of galaxies with low SFRs reach a minimum at $\sim$10 $\mathrm{km\,s^{-1}}$(Krumholz et al. 2018).

It is clear from this study that below a stellar mass of $10^{8.6}\,\mathrm{M_\odot}$ there is an excess of velocity dispersion relative to the gravitational potential from stellar mass. Figure 4.14 shows the distribution of the average velocity dispersion for SHαDE galaxies, excluding the SAMI control sample (i.e. for masses $M_\star \lesssim 10^9\mathrm{M_\odot}$). This distribution has a mean velocity dispersion around 21.1 $\mathrm{km\,s^{-1}}$and a 68% confidence interval of [17.1,26.7] $\mathrm{km\,s^{-1}}$. This range is consistent with that from Varidel et al. (2020), with the slight difference perhaps stemming from the beam-smearing correction that they

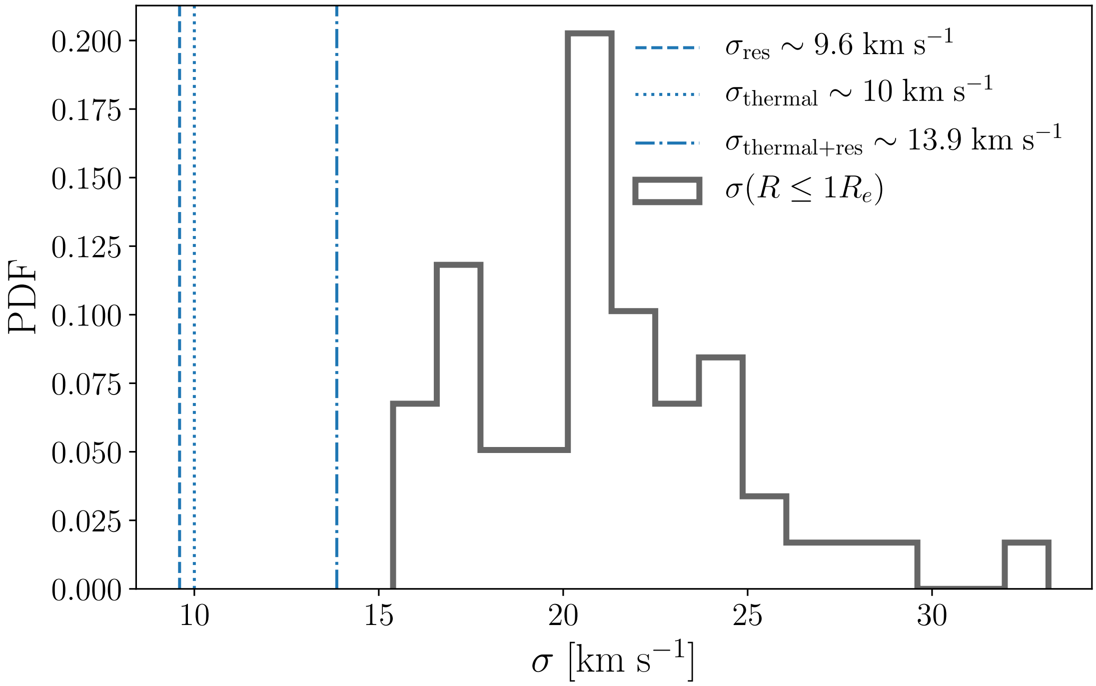

Figure 4.14: The velocity dispersion distribution for SHαDE galaxies with $\log M_\star/\mathrm{M}_\odot \lesssim 9.0$. The dashed line at $\sigma = 9.6$ km s^{-1}indicates the instrumental resolution ($\sigma_{\rm res}$). The dotted line at $\sigma = 10$ km s^{-1}represents the velocity dispersion contribution from the HII thermal contamination ($\sigma_{\rm thermal}$). The dot-dashed line at $\sigma = 13.9$ km s^{-1}represents the effective combined velocity dispersion limit $\sigma_{\rm thermal+res} = \sqrt{\sigma^2_{\rm thermal} + \sigma^2_{\rm res}}$.

perform.

There are several possible drivers for enhanced velocity dispersions in late-type galaxies, such as merger events (Glazebrook 2013), gravitational instability (Bournaud et al. 2010, 2014; Goldbaum et al. 2015), star-formation rate feedback (Lehnert et al. 2009, 2013; Green et al. 2010, 2014; Yu et al. 2019), and thermal contamination from HII regions (which contributes a velocity dispersion of ∼10 km s^{-1}; Krumholz et al. 2018). While Krumholz & Burkhart (2016) put forward star-formation feedback and gravitational instability as two models of turbulence, these models are most applicable to galaxies with relatively higher velocity dispersions ($\sigma > 50$ km s^{-1}) and higher SFR

(SFR $\gtrsim$ 10 $M_{\odot}yr^{-1}$). Additionally, applications of these models often involve adding extra velocity dispersion of ∼15 $\mathrm{km\,s^{-1}}$ (as seen in Yu et al. 2019; Varidel et al. 2020) to account for the thermal contamination of HII regions. Therefore without HII contribution, neither of the two models can explain the observed velocity dispersion in SHαDE.

The HII contamination argument (Menon et al. 2020) is plausible in explaining the velocity dispersion. This is because observations of extragalactic Hα dynamics will always overlap with HII regions. The velocity dispersion of HII regions vary between 10 $\mathrm{km\,s^{-1}}$ to 40 $\mathrm{km\,s^{-1}}$ depending on their size and temperature (e.g. 30 Doradus Chu & Kennicutt 1994). Therefore the observed Hα spectrum within an aperture will be a sum of Gaussian profiles, with minimum width of ∼10 $\mathrm{km\,s^{-1}}$ or more. This means the minimum observed velocity dispersion is partially limited by the thermal expansion of HII regions.

Another possible driver for the turbulence is supernovae feedback. Most recently, Bacchini et al. (2020) determined the energy produced by supernovae explosions alone is sufficient to provide enough energy to match the kinetic energy measured from HI and CO observations of near by star-forming galaxies. They argue that in comparison to supernovae feedback, HII expansion is of secondary importance in driving the turbulence, based on the finding by Walch et al. (2012) that HII expansion driven by stellar ionisation radiation can only explain about 2–4 $\mathrm{km\,s^{-1}}$of the turbulence. Without additional data, determining which of these factors apply remains speculative and will need to be investigated further in future studies using both more extensive HI observations, stellar kinematics data and more sophisticated dynamical modelling.

4.8 Summary

In this work, we present the SHαDE survey, a high spectral resolution Hα integral field survey of 69 dwarf galaxies in the local universe. We describe the survey goals, target selection, and data reduction process.

We investigate the $\log M_\star$–$\log S_{0.5}$ kinematic scaling relation using these dwarf galaxy observations. We find that there exists a lower limit at $S_{0.5} \approx 22.4\,\mathrm{km\,s^{-1}}$, which corresponds to a stellar mass limit of $M_\star \approx 10^{8.6}\,\mathrm{M_\odot}$. Above this limit, the scaling relation has a slope of 2.58 ± 0.02 and an intercept of 5.16 ± 0.05. This lower limit originates from an apparent lower limit in the observed Hα velocity dispersion at $\sim$20 $\mathrm{km\,s^{-1}}$. These results are consistent with previous studies of the scaling relation using only SAMI data without the additional SHαDE observations. They suggest a physical origin of the low-mass bend in the Hα version of $\log M_\star$–$\log S_{0.5}$ scaling relation. Using baryonic mass (based on estimating the gas mass from SFR measurements) reduces the severity of the bend in the scaling relation. This is partially due to the fact that, for their stellar mass, dwarf galaxies have higher sSFR compared to more massive galaxies. With some additional assumptions, the quantity that gives the most linear scaling relation is the estimated halo mass of galaxies, M_h. The $\log M_h$–$\log S_{0.5}$ scaling relation is free of any bend at the low-mass end, has reduced curvature over the whole mass range, and brings galaxies of all masses and morphologies onto the virial relation.

4.9 Acknowledgements

We would like to thank the referee for their useful and constructive feedback. We would also like to thank Christoph Federrath, Sharon Meidt, and Ken Freeman for their advice and suggestions on the analyses. This work is based on observations made with ESO telescopes at the La Silla Paranal Observatory under programme IDs 0101.B-

0505(A), 0101.B-0505(B) and 0101.B-05050(C). Part of this research was supported by the Australian Research Council Centre of Excellence for All Sky Astrophysics in 3 Dimensions (ASTRO 3D), through project CE170100013. DB is also supported by an Australia Government Research Training Program Scholarship. FDE acknowledges funding through the H2020 ERC Consolidator Grant 683184. LC is the recipient of an Australian Research Council Future Fellowship (FT180100066) funded by the Australian Government. The SAMI Galaxy Survey is based on observations made at the Anglo-Australian Telescope. The Sydney-AAO Multi-object Integral field spectrograph (SAMI) was developed jointly by the University of Sydney and the Australian Astronomical Observatory. The SAMI input catalogue is based on data taken from the Sloan Digital Sky Survey, the GAMA Survey and the VST ATLAS Survey. The SAMI Galaxy Survey is funded by the Australian Research Council Centre of Excellence for All-sky Astrophysics (CAASTRO), through project number CE110001020, and other participating institutions. The SAMI Galaxy Survey website is http://sami-survey.org/. Funding for SDSS and SDSS-II has been provided by the Alfred P. Sloan Foundation, the Participating Institutions, the National Science Foundation, the U.S. Department of Energy, the National Aeronautics and Space Administration, the Japanese Monbukagakusho, the Max Planck Society, and the Higher Education Funding Council for England. The SDSS Web Site is http://www.sdss.org/. SDSS is managed by the Astrophysical Research Consortium for the Participating Institutions. The Participating Institutions are the American Museum of Natural History, Astrophysical Institute Potsdam, University of Basel, University of Cambridge, Case Western Reserve University, University of Chicago, Drexel University, Fermilab, the Institute for Advanced Study, the Japan Participation Group, Johns Hopkins University, the Joint Institute for Nuclear Astrophysics, the Kavli Institute for Particle Astrophysics and Cosmology, the Korean Scientist Group, the Chinese Academy of Sciences (LAMOST), Los Alamos National Laboratory, the Max-Planck-Institute for Astronomy (MPIA), the Max-Planck-

Institute for Astrophysics (MPA), New Mexico State University, Ohio State University, University of Pittsburgh, University of Portsmouth, Princeton University, the United States Naval Observatory, and the University of Washington.

Chapter 5

Taipan Live Data Reduction (TLDR)

*Parts of section 5.4, 5.5 and 5.6 of this chapter are contributed by Michael J. Cowley, Samuel R. Hinton, and Matt S. Owers, respectively; they are shown in italics. These sections are also published in Publications of the Astronomical Society of Australia as: The Taipan Galaxy Survey: Scientific Goals and Observing Strategy.*da Cunha, E., ..., **Barat, D.**, et al., 2017, PASA, 34, 47. We included them in this thesis to have a complete narrative.

5.1 Introduction

Thanks to the invention of multi-fibre spectrograph (e.g. the MEDUSA spectrograph, Hill et al. 1980), the field of astronomical spectroscopy survey was industrialised. With this new technology, large-scale surveys with short timeframes were made possible. We have seen the scientific benefits of bulk spectroscopic observations from surveys such as the 2dF Galaxy Redshift Survey (2dFGRS; Colless et al. 2001), the 6dF Galaxy Survey (6dFGS; Jones et al. 2004), SDSS (Gunn et al. 2006), and the Large sky Area Multi-

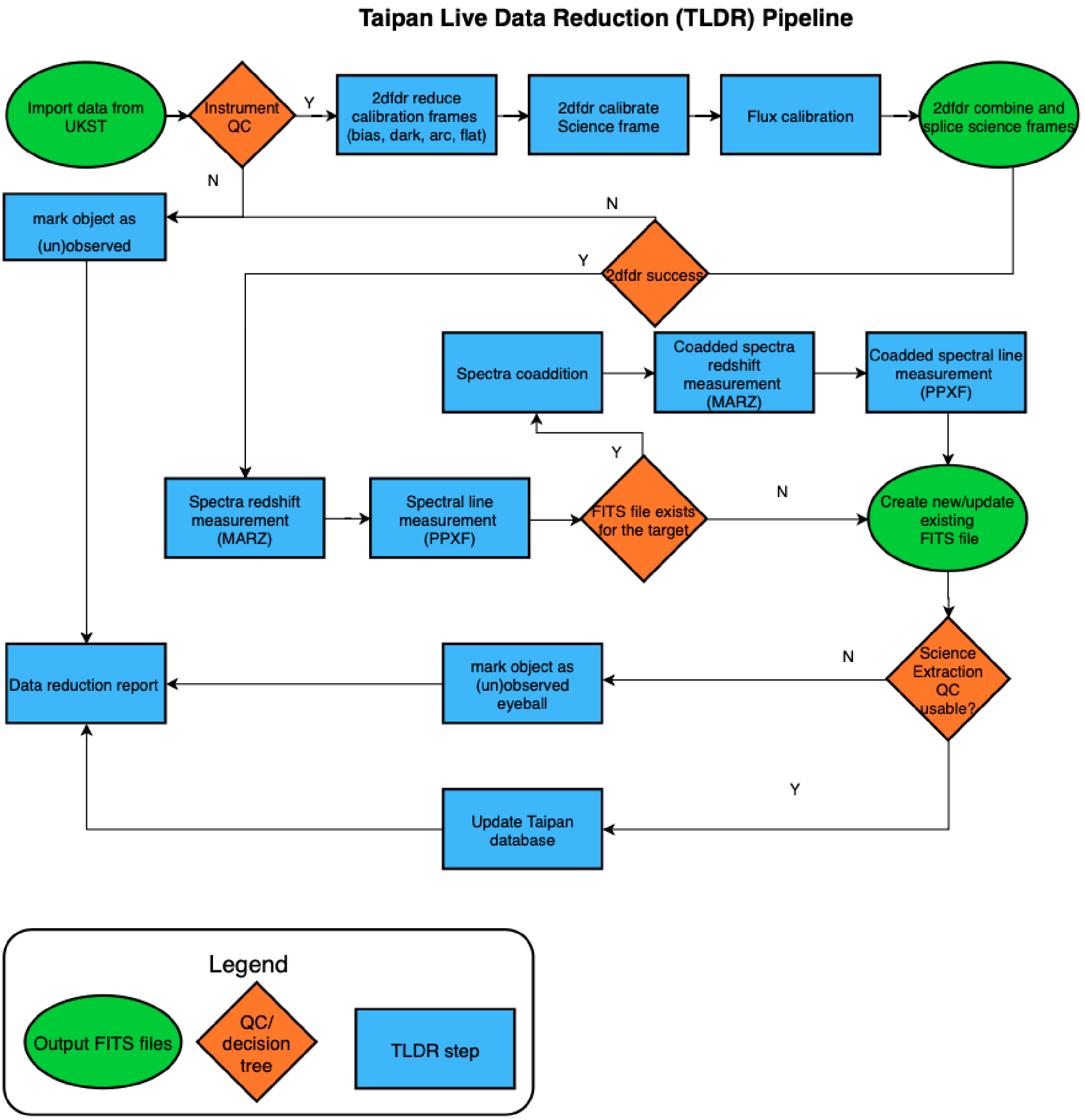

Figure 5.1: TLDR logic flow chart. The reduction process begins in the top left corner of the diagram with importing the raw data observed from the UKST and ends at the bottom left corner with the creation of the data reduction report.

Object fibre Spectroscopic Telescope spectral survey (LAMOST; Zhao et al. 2012). The trend of increasing efficiency has continued with current-day surveys such as the Australian Dark Energy Survey (OzDES; Yuan et al. 2015; Childress et al. 2017; Lidman et al. 2020), the Dark Energy Spectroscopic Instrument Survey (DESI; DESI Collaboration et al. 2016), and the planned Taipan survey (da Cunha et al. 2017). Big surveys result in big data, but astronomical observations are not without artefacts and the data do not naturally present themselves in analysis-ready tables. A big challenge in large-scale surveys is data reduction and data management. Traditionally, this process was done manually for each individual target using software such as the Image Reduction and Analysis Facility (IRAF; Tody 1986). However, this strategy is not suitable when the number of targets is on the order of millions. Hence for upcoming large-scale spectroscopic surveys such as the Taipan survey, the process of data reduction and scientific quantity extraction must be performed with minimal human interaction and ideally be fully automated, while simultaneously satisfying survey precision requirements.

The Taipan galaxy sample data are planned to be processed through the Taipan Live Data Reduction (TLDR) pipeline. This pipeline that will be triggered with the readout of new data from the TAIPAN spectrograph (Staszak et al. 2016). TLDR will be responsible for performing quality control tests and producing calibrated, science-ready spectra, as well as generating data products including redshifts, velocity dispersions, and emission line fluxes. The workflow of the pipeline is shown in Figure 5.1. TLDR takes advantage of multiple existing standard software packages as well as custom modules to perform data reduction. The main components of TLDR are 2-degree field data reduction (2dFdr) for initial data reduction from the raw observed images to wavelength- and flux-calibrated spectra (AAO Software Team 2015), MARZ for redshift determination (Hinton et al. 2016), and pPXF for kinematic measurements and emission/absorption line measurements (Cappellari 2017); these components are described in more detail in the following sections.

5.2 Creating Mock Data

The commissioning of the complex instruments used in large-scale astronomical surveys is often delayed, and this is the case with the TAIPAN instrument for the Taipan survey. At the time of writing this thesis, TAIPAN is scheduled to be commissioned in first quarter of 2021. This poses a number of challenges for constructing, characterising and validating the data reduction pipeline, such as not being able to characterise the detectors and other as-built elements of the the system, and also not having a final output file definition. To allow the development of the pipeline in anticipation of these inputs, which will only be available after the TAIPAN instrument is commissioned, we create mock data to perform initial function tests.

We created two sets of mock data. The first set aims to test the functionality of the early stages of the TLDR pipeline, with particular focus on detector characterisation and content management. For this purpose, we use a set of model spectra (Pacifici et al. 2012) with added observational artefacts, such as CCD response variance, spectral projection on the CCD, and realistic wavelength to pixel conversion.

The second set of mock data is used exclusively to test TLDR's ability to extract scientific quantities. Here we focus on deriving redshifts and stellar and gas velocity dispersions using MARZ and pPXF. We base this set of mock spectra on a subset (144) of the MILES model spectra by Vazdekis et al. (2010). For each model spectrum, we create 5 copies of the spectrum and add common emission lines to a subset of them. Then we convolve it with an intrinsic dispersion between 60 $\mathrm{km\,s^{-1}}$and 240 $\mathrm{km\,s^{-1}}$and with the TAIPAN spectral resolution (2.55 Å FWHM). We also randomly redshift the spectra, with values in the range $0.001 < z < 0.1$, and degrade them with S/N in the range $5 < \mathrm{S/N} < 30$.

With these two datasets we have the ability to test each component of TLDR to ensure its function and accuracy in the results returned and simulate the performance of the system for key measurables.

5.3 Data reduction: 2dFdr-TAIPAN

The first stage of TLDR uses a customised version of the 2dFdr multi-fibre spectroscopic data pipeline, originally developed in the mid-1990s for the 2dFGRS (Colless et al. 2001) and the 2dF spectrograph. In its early days, 2dFdr was only tasked to produced spectra for the purpose of redshift or velocity measurements, which were the main parameters of interest for the 2dFGRS. Since then, a significant amount of effort has been invested in 2dFdr to adapt it to subsequent fibre instruments such as 6dF (Jones et al. 2004), AAOMega (Smith et al. 2004) (in both single-fibre and IFU modes), and HERMES (Sheinis et al. 2014). At this stage, 2dFdr has reached a level of sophistication that allows it to produce spectra not only for redshifting, but also for chemical composition measurements and kinematic analyses. Most recently, 2dFdr has been used in production by the OzDES Survey (Yuan et al. 2015; Childress et al. 2017; Lidman et al. 2020) to perform real-time data reduction and spectra extraction for high- redshift ($z \sim 4$) and transient targets.

For the Taipan survey, 2dFdr has been modified to accommodate TAIPAN's new spectral format. The main task for 2dFdr in TLDR is to reduce the raw data by removing CCD artefacts and extracting individual spectra for further processing. Here we will use the mock data we have created to demonstrate the process. To perform data reduction on the observations obtained from one field, we need at least the following three basic files:

- **Multi-fibre flat field exposure:** This exposure is obtained from the light of a quartz lamp, illuminating the field of view with a (relatively) uniform light source so that each spectrum can be centred and traced and pixel-to-pixel response variations mapped.
- **Arc exposure:** The light source for this exposure is a lamp with known emission lines providing a reference for pixel-to-wavelength conversion.

- **Science exposure:** This exposure captures data from the scientific targets observed for the survey during the night.

As the TAIPAN spectrograph consists of a blue and a red arm to cover its full wavelength range (Kuehn et al. 2014), at minimum we will have 3 blue+red pairs of the above exposures. Once the files are ready, TLDR will import the files and configure a directory structure to group all the calibration frames and object frames before proceeding to reduce the files. The exact procedure is broken into multiple steps, described in the following subsections.

The original intended usage for 2dFdr was to reduce a small amount of data at a time, and for this purpose an intuitive graphical user interface (GUI) was developed for 2dFdr to assist with the reduction. However, for large-scale surveys with automated data reduction pipelines, such as Taipan and TLDR, using the GUI is not a sustainable approach. Instead, we make use of the scripted version of 2dFdr, a collection of terminal commands called by `aaorun`. The main commands used by TLDR are:

```
aaorun make_tlm

aaorun reduce_arc

aaorun reduce_fflat

aaorun reduce_object

aaorun combine_spectra

aaorun splice
```

The underlying logic for TLDR is to use 2dFdr by constructing these commands with appropriate inputs and arguments. While the 2dFdr GUI provides user-friendly windows and tabs for easy tuning and configuration of the reduction process, for the scripted version of 2dFdr, all reduction parameters are defined within a `taipan.idx` file. This is a machine-readable text file that allows the user to save the 2dFdr settings required specifically to reduce data from the TAIPAN instrument. For the mock data, we use the stock `taipan.idx` file with all the default settings; once commissioning data is obtained, these parameters will be fine-tuned for the as-built instrument and optimised to obtain the most accurate data reduction results.

5.3.1 Calibration

TLDR uses 2dFdr to perform data calibration with the flat field and arc exposures. This process includes tram-line mapping, wavelength calibration, and flat-fielding.

Tram-line mapping is the process of tracing the 'tram line' of the spectra on the CCD with a polynomial. For this we make use of the flat-field exposures. TLDR constructs the following command to perform tram-line mapping:

```
aaorun make_tlm 21apr20001.fits -idxFile taipan.idx
```

where `21apr20001.fits` is the flat-field exposure. Figure 5.2 shows a cropped frame of the flat-field exposure with the tram-lines (in red) overlaid on top. For the purpose of testing the functionality of TLDR, the extraction method for tram-line mapping is set to the simplest method, an unweighted sum of the flux within an aperture centred on the tram-lines. More sophisticated and accurate methods exist in 2dFdr, the best being *optimal extraction* (Farrell et al. 2019). This method fits the flux in each fibre and the background simultaneously column-by-column and will be tested when observed data are made available.

After the fibres are traced, 2dFdr uses the arc frames to perform wavelength calibration. For this process, TLDR provides 2dFdr with not only the arc exposure (`21apr20002.fits`), but also the output (`21apr20001tlm.fits`) of the previous tram-line mapping step. The exact command has the format:

```
aaorun reduce_arc 21apr20002.fits -idxFile taipan.idx -TLMAP_FILENAME 21
    apr20001tlm.fits
```

Figure 5.3 shows the reduced arc frame. Note that, at this stage, the horizontal axis has been transformed from pixel space to wavelength space.

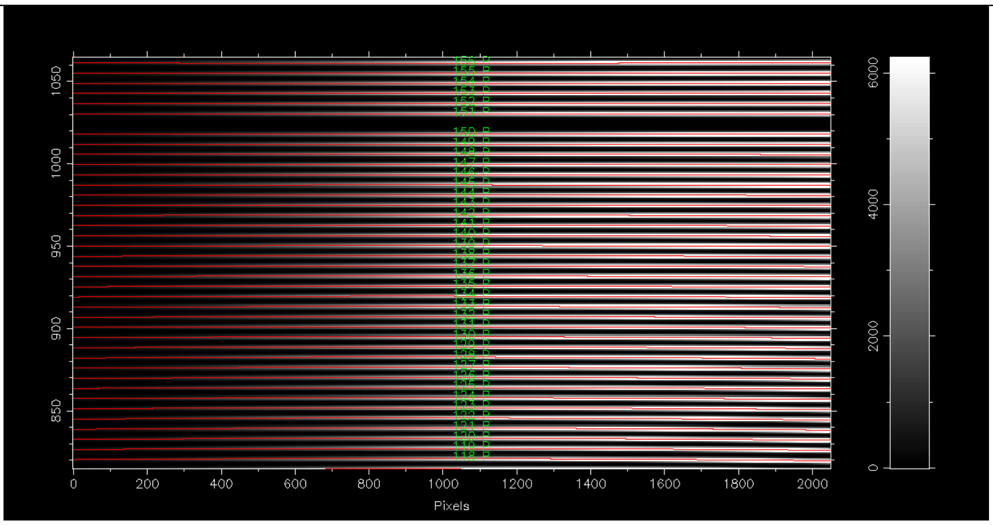

Figure 5.2: An example section of the fibre flat frame with tram-line map. Each fibre appears as an illuminated strip with increasing flux from left (the blue end) to right (the red end). The polynomial tram-line mapping done by 2dFdr is shown by the red lines. The numbers followed by a letter, e.g. 150 P, represent the fibre numbers. Note that at this stage, each fibre spectrum spans multiple pixels vertically (i.e. spatially). This example shows a satisfactory tram-line map without any appreciable offset between the red lines and spatial centres of the fibre spectra.

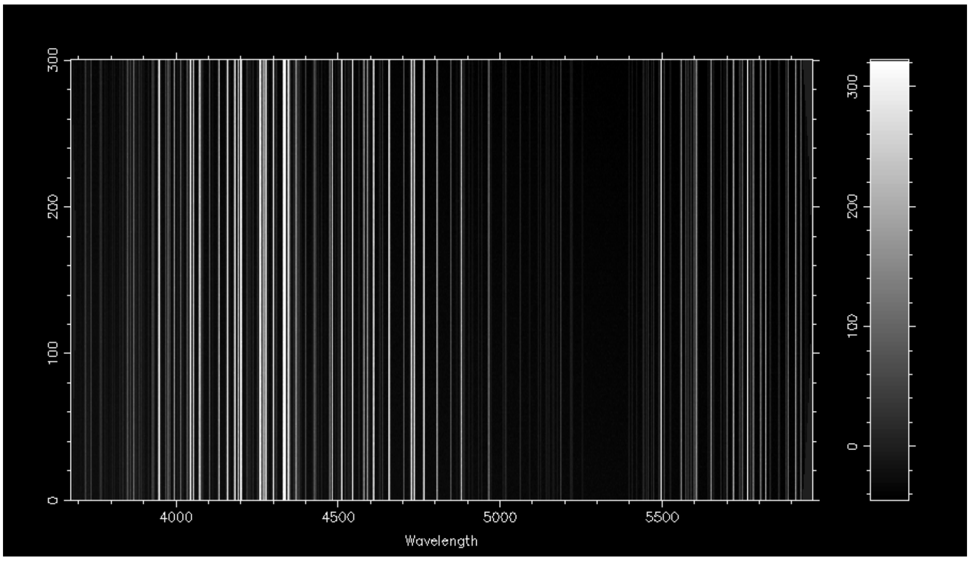

Figure 5.3: An example reduced arc frame. Note that after tram-line mapping, each row of the image corresponds to a single fibre spectrum. After arc frame reduction, the pixel scale on the horizontal axis has been replaced by a wavelength scale, in units of Ångstroms. In this example we can see that the arc frame has been reduced successfully without any fibre-to-fibre discontinuity or misalignment (i.e. each of the arc lines forms a straight, undeviated, vertical bright stripe).

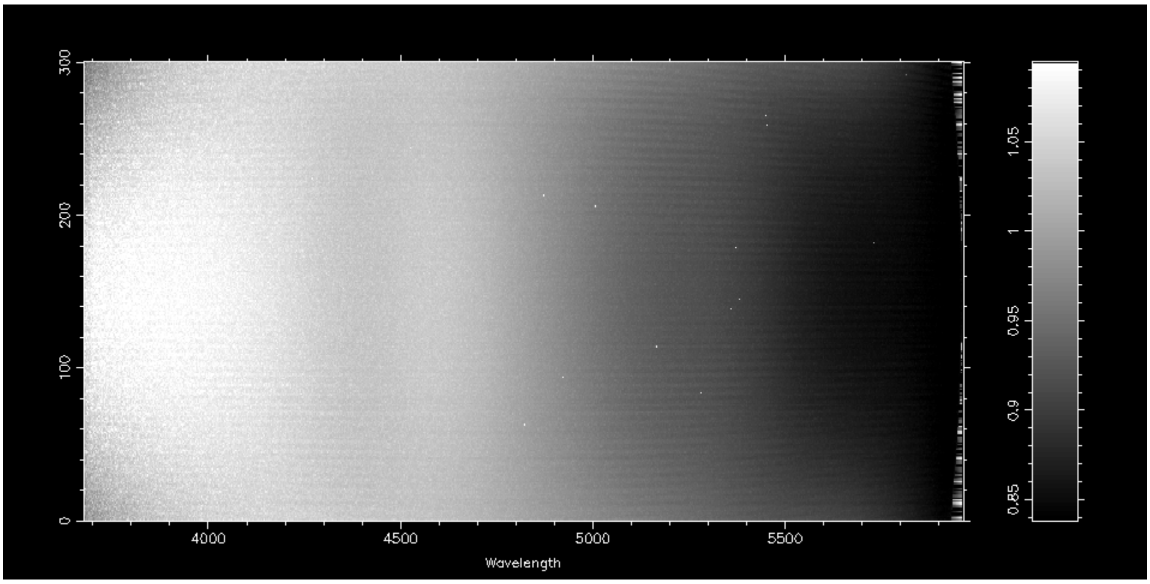

Figure 5.4: An example of a reduced flat frame. This frame shows the pixel-to-pixel response variation of the CCD as well as the general gradient across the field indicating the CCD is more responsive to the red end of the spectrum and less responsive to the blue end.

The last step of calibration is reducing the flat exposure. TLDR performs this by gathering all previous calibration data, namely the tram-line map and reduced arc frame, and constructing the following command:

```
aaorun reduce_fflat 21apr20001.fits -idxFile taipan.idx -TLMAP_FILENAME 21
    apr20001tlm.fits -WAVEL_FILENAME 21apr20002red.fits
```

The purpose of this step is to characterise the CCD at a pixel level. The basic idea is to illuminate the CCD uniformly and measure the response for each pixel. In a perfect instrument the whole frame would be uniform; however, due to variations in illumination and in each pixel's quantum efficiency and wavelength sensitivity, there is typically both a relatively smooth gradient across the frame in one or more directions as well as pixel-to-pixel response variations, as demonstrated in Figure 5.4.

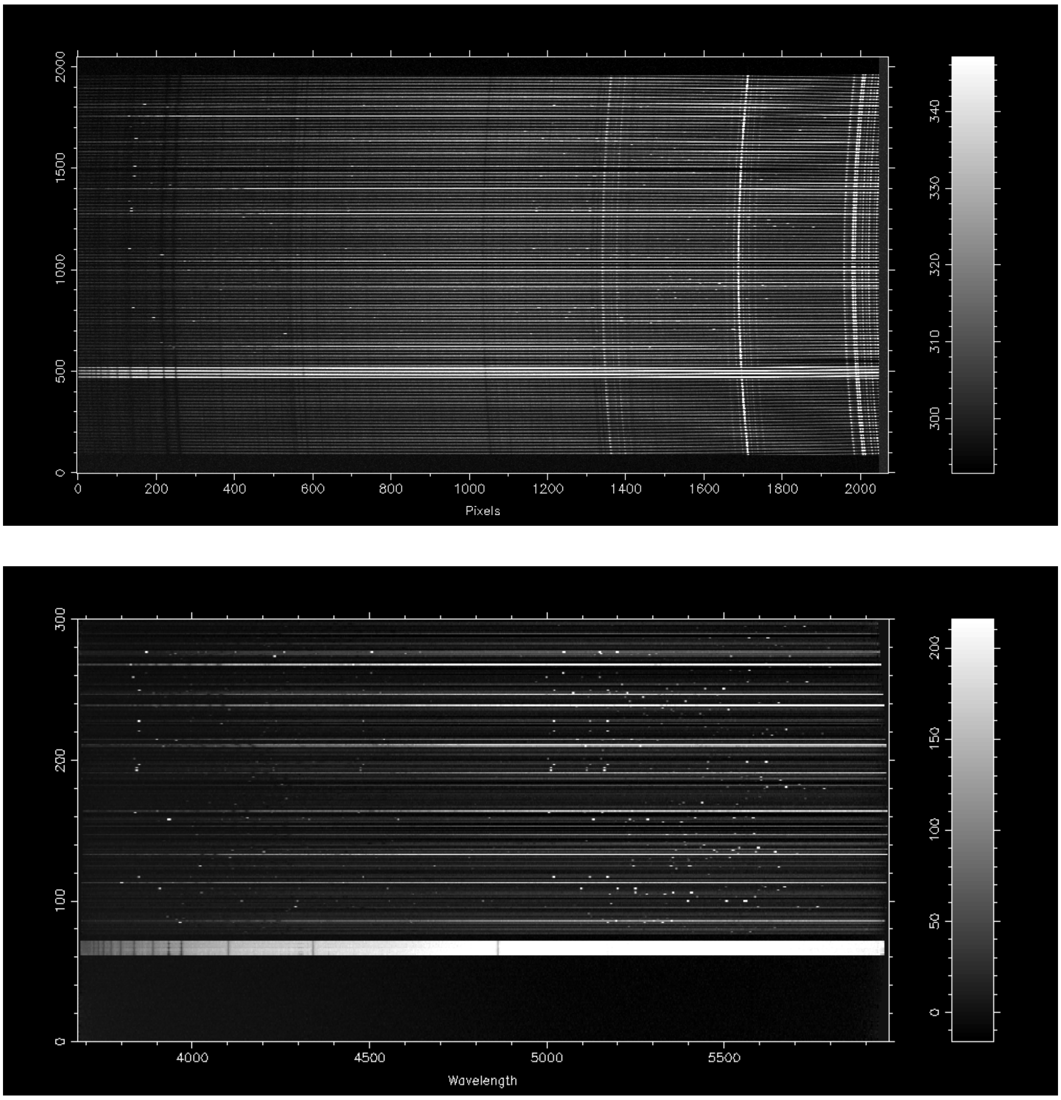

Figure 5.5: The raw (top) and reduced (bottom) mock science frames. In the top panel, we can see that the frame resembles that from the flat-field frame, but contains more features. The absorption and emission line features common across all fibres are artefacts caused by the atmosphere. After reduction, in the bottom panel, where each row corresponds to the spectrum from one fibre, we can see that all spectra have been traced, wavelength-aligned, and had atmospheric artefacts removed, leaving only the intrinsic features of the spectra.

5.3.2 Reducing science frames

Once the CCD is characterised with the flat and arc frames, the science frame (`21apr20003.fits`) can be reduced by constructing the command:

```
aaorun reduce_object 21apr20003.fits -idxFile taipan.idx -TLMAP_FILENAME 21
    apr20001tlm.fits -WAVEL_FILENAME 21apr20002red.fits -FFLAT_FILENAME 21
    apr20001red.fits
```

This process applies fibre-tracing, wavelength calibration, flat-fielding, sky-line subtraction, and cosmic ray removal. Figure 5.5 shows the science frame before and after the reduction. We can see that the CCD image was transformed from a 2048 pixel×2070 pixel image (in Figure 5.5, top panel) to a 2048 pixel×300 pixel image (in Figure 5.5, bottom panel), where each row represents a spectrum. It can be seen in the figure that rows (fibres) 1 to 61 do not have any features because these are sky fibres without any target, so that, after sky-subtraction, all features from these fibres have been removed. By contrast, rows 62 to 71 are brighter than the other fibres and contain only absorption lines; these fibres simulate the photometric standard stars that Taipan will include with every pointing of the telescope for flux calibration purposes. Once 2dFdr has reduced all the object frames, TLDR will extract all the standard star spectra in the object frames, and construct a transfer function for flux calibration; the calibration process itself is discussed further in the next section.

The Taipan survey strategy involves observing each frame with 3 exposures of 5-minute duration. For each target galaxy, these 3 exposures form a VISIT[1]. For the peculiar velocity targets, Taipan will repeatedly visit to allow signal co-addition in order to reach the desired signal-to-noise ratio. Once the signal-to-noise ratio is met, the collection of VISITS will form a REPEAT[2]. For a sub-sample of these galaxies,

---

[1] We use capitalised VISIT here to denote a Taipan survey key word; a VISIT is a set of 3 exposures, at a frame level, obtained together at the same pointing of the telescope.

[2] REPEAT is also a Taipan survey key word, it denotes a collection of VISITS for an *individual* target that are going to be co-added to boost signal-to-noise; a REPEAT starts with index 0.

multiple REPEATs will be obtained for various consistency tests.

With all 3 exposures reduced, TLDR will group these frames together and perform a combine-and-splice. For this process, TLDR constructs the following commands:

```
aaorun combine_spectra "21apr20003red.fits 21apr20004red.fits
       21apr20005red.fits" -idxFile taipan.idx
       -COMBINEDFILE CCD_2_COMBINEDred.fits

aaorun splice "CCD_1_COMBINEDred.fits CCD_2_COMBINEDred.fits"
       -idxFile taipan.idx -OUTPUT_FILE Mysplice.fits
```

With these commands, 2dFdr produces a flux-weighted combined frame for the VISIT for each arm of the spectrograph, then splices the blue and red VISIT frames to form a single VISIT frame spanning the entire wavelength coverage of the TAIPAN spectrograph. For the splicing process, 2dFdr allows the wavelengths of one arm to be rebinned to match the other (also known as ‘scrunching’) and the mid-point wavelength of the splicing to be adjusted. For the mock data, these specifications are set to the default values of scrunching the red arm and a mid-point of 5700Å. For real observations, these values will be revised and adjusted as needed.

5.4 Flux calibration

Spectral flux calibration of TAIPAN data is performed using F stars selected from the SkyMapper survey, following the approaches used by the SDSS and GAMA surveys. We transform the SDSS broad-band colours to SkyMapper broad-band colours using the colour terms measured by the SkyMapper team[1]*. A SkyMapper colour cut is used to*

---

[1] http://skymapper.anu.edu.au/filter-transformations/

select F stars for flux calibration[1]*:*

$$\left\{\left[(g-r)-0.18\right]^2+\left[(r-i)-0.11\right]^2+\left[(i-z)-0.01\right]^2\right\}^{1/2}<0.08 \qquad (5.1)$$

We note that we do not use the u–g colour cut in the SDSS algorithm due to the red leak of the SkyMapper u-band filter. We have tested our selection procedure using SDSS spectroscopic observations, and find that about 80% of the stars selected by these criteria are F stars (and the remainder are mostly G stars). Spectral calibration stars from this list will be added into, and observed in, each Taipan field. To flux-calibrate the observed galaxy spectra, we first restrict our photometrically selected standard stars to those brighter than $r = 16.5$ *and with a posterior acceptable spectral signal-to-noise. Based on the broad-band photometry, we then select and warp a synthetic spectral template from Pickles (1998) to match the standard stars, before correcting for atmospheric extinction using the extinction coefficients measured at Siding Spring Observatory. A sensitivity function is then derived from a low-order spline fit to the ratio of the observed and warped synthetic spectra of the standard stars. Finally, the blue and red arm sensitivity curves are applied to the coadded science frames to be spliced.*

5.5 Redshift: MARZ

We measure redshifts automatically using MARZ (Hinton et al. 2016), which implements a template-matching cross-correlation algorithm adapted from AUTOZ(Baldry et al. 2014). MARZ fits input spectra against a range of stellar and galactic templates, and returns the redshift and template corresponding to the best cross-correlation, along with an estimate of the reliability (confidence level) of the result. MARZ also allows easy visualisation of spectra via its web interface, however the primary usage of the application in our pipeline is to be run automatically without human input. MARZ

---

[1] `https://www.sdss.org/dr12/algorithms/boss_std_ts/`

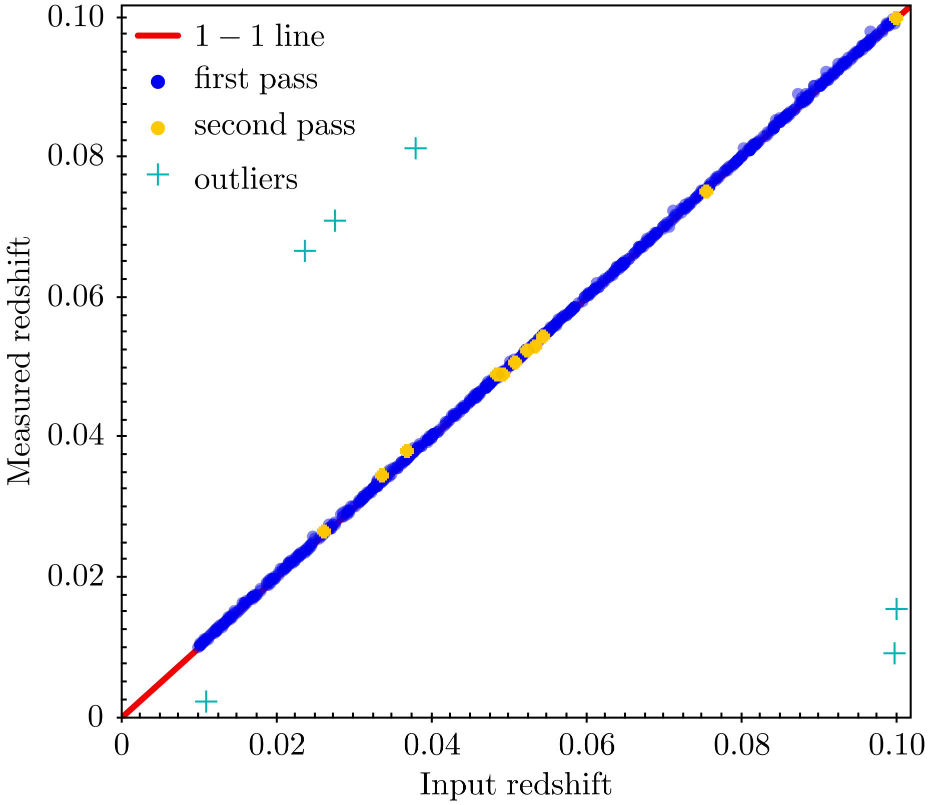

Figure 5.6: Redshift retrieval from MARZ-TLDR. Blue points represent data points from the top results returned by MARZ; yellow points represent cases when the correct results were returned as the second-top result by MARZ; cyan crosses are points where MARZ failed to obtain correct redshift results. The red line is the one-to-one line.

leverages a job queuing system, allowing fast redshift measurement and the potential to re-redshift prior targets in bulk if the data reduction pipeline undergoes improvement during the survey. The output redshifts and confidences from MARZ are fed back into the survey database, where the optimal tile configurations and observational schedule for the telescope are updated.

The performance and reliability of MARZ have been characterised well in Hinton et al. (2016) and Childress et al. (2017). Here we use the second set of (720) mock spectra to demonstrate its performance in a Taipan context. Figure 5.6 shows the comparison between the input redshift values and MARZ redshift measurements. In the scripted version of MARZ, it returns its top-three redshift results. From the figure, we can see that the great majority (704 out of 720) of spectra return accurate redshift measurements with the input/output redshift difference being less than 0.001. Of the remaining spectra, another 10 spectra had the correct redshift as the second-top result from MARZ. In total, only 6 out of the 720 spectra had incorrect redshift measurements, translating to a 99.2% accuracy. Upon inspection using the GUI version of MARZ, these 6 spectra were fit with inappropriate template spectra; once the correct templates were chosen manually, their redshifts were retrieved correctly.

5.6 Spectral measurements and quality control

After redshifts are determined, the next step is to perform further spectral measurements, using a custom version of the Penalised Pixel Fitting code (pPXF Cappellari & Emsellem 2004).

We first mask known strong emission lines and use pPXF to find the best-fitting simple stellar population (SSP) template combination, as well as an initial guess for the velocity dispersion and velocity offset (from the MARZ redshift). We then rescale the 2dFdr variance array by the ratio of the standard deviation of the residuals after subtracting the best-fit templates. The next step is to unmask emission lines and include emission templates in the pPXF fit, as well as doing iterative cleaning to remove outliers, before re-fitting (good variance estimates from the previous steps are needed for this clipping). This determines final estimates for the mean stellar velocity and velocity dispersion. We then fix the stellar kinematics derived above and re-fit to determine the optimal combination of SSP templates for the underlying stellar continuum, again using pPXF and including emission templates. We interpolate the best-fit description of the stellar continuum onto the wavelength grid for the data and subtract from the data, leaving only the emission line residual spectrum. This step minimises the impact of re-

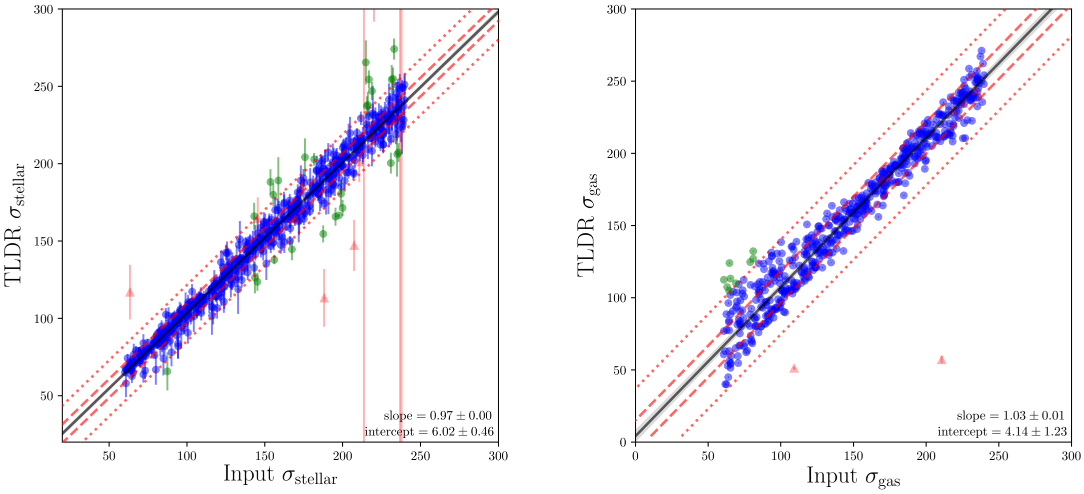

Figure 5.7: Stellar (left) and gas (right) velocity dispersion retrieval performance of TLDR. In both panels we compare the velocity dispersion values returned by TLDR with the input values. The black solid line is the best-fit to the data and the red dashed and dotted lines are offset, respectively, ±1 and ±3 standard deviations (orthogonally) away from the best-fit line. In both panels we included the galaxies with incorrect redshift measurements for completeness; these are shown as red triangles. The two red vertical lines in the left panel are extremely large error bars caused by incorrect redshifts. In the gas velocity dispersion comparison, we excluded galaxies where no emission lines were added to the MILES template spectra.

binning multiple times on the emission line measurements and uncertainties determined in the next step, which consists of fitting Gaussians to emission lines in the residual spectrum ([OII] doublet, Hδ*,* Hγ*,* Hβ*, [OIII] doublet, [OI] doublet, [NII] doublet, H, [SII] doublet). The kinematics of the Balmer lines are tied together, as are, separately, the kinematics for the forbidden lines. The Gaussian amplitudes and widths are used to determine the line fluxes and formal uncertainties are propagated through to determine a flux uncertainty. We also include an S/N proxy, which uses the standard formalism of Lenz & Ayres (1992) to estimate the line S/N based on the fit residuals.*

In Figure 5.7 we show the comparison between the input velocity dispersions and the measured stellar and gas velocity dispersions. We can see the dispersion values are highly correlated, with $\sigma_{\rm TLDR,stellar} = 0.97\sigma_{\rm Input,stellar} + 6.02$, and $\sigma_{\rm TLDR,gas} = 1.03\sigma_{\rm Input,gas} + 4.14$. While there is a slight offset between the input and retrieved stellar and gas velocity dispersion, the slopes of the correlations are just 3% away from unity. In the stellar velocity dispersions comparison, the scatter of the distribution shows a decrease in the scatter for low dispersion measurements (input $\sigma_{\rm stellar} \lesssim 120$ $\mathrm{km\,s^{-1}}$), which is an artefact stemming from the stellar continuum signal-to-noise ratio implementation not being perfectly realistic; in actual observations, lower dispersions are expected to correlate with lower S/N and will tend to have larger errors. In the gas velocity dispersion comparison, the results are more realistic, as signal-to-noise ratio typically decreases with smaller velocity dispersions, and the resulting dispersion measurements will have larger scatter and uncertainties.

Once TLDR has retrieved stellar and gas kinematics, it will forward the measurements together with others spectral measurements to the database, and the survey scheduling algorithm decides whether a target needs to be re-observed based on the survey rules, which prescribe a minimum required S/N for our targets.

5.7 The data product

The ultimate goal of TLDR is to produce an analysis-ready data product after all the processes described previously. To store all the extracted science quantities, TLDR constructs a Flexible Image Transport System (FITS) file for each target galaxy. The most important pieces of information for any spectroscopy surveys would be the spectra. As we have described previously in section 5.3.2, the Taipan survey strategy includes multiple observations in the form of VISITS and REPEATS. Consequently, each target galaxy will have multiple spectra observed and created through co-addition. The listing 5.1 below shows an example FITS file structure created for a mock target (`104.fits`). For demonstration purpose, we pretend this target has been VISITed 5 times[1] and after the third VISIT the target has accumulated sufficient signal-to-noise ratio to be used as a REPEAT, and this initial REPEAT is marked as complete. Subsequent VISITS will be used to form the next REPEAT. This exercise is reflected in listing 5.1 below, notably through the data dimension. The `PRIMARY` extension consists of a spectrum that is created by co-adding all the VISITS available for the target; this spectrum is accompanied by the co-adddded variance and the co-added sky spectrum, which is reflected by the extension dimension (4588×3), which represents the wavelength dimension repeated three times for the flux, variance, and sky flux. Similarly, the `REPEATS` extension has a dimension of (4588×3×2), with the first being wavelength array, second one representing target flux, variance, and sky flux. The third dimension indicates there are two sets of REPEATS, where the first set is a co-addition of the initial three VISITS, and the second set is from the co-addition of the subsequent two VISITS. Note that spectra co-added to form a REPEAT will not be used again for other REPEATS. The `VISIT` extension is where all the observations made for the target can be found. In the case for `104.fits`, there are 5 VISITS, hence the extension dimension (4588× 3×5).

---

[1] Recall each VISIT is a set of three 5-minute exposures, which are then combined.

In extensions 3, 4, and 5 of the FITS file, TLDR records the scientific quantities extracted from individual and co-added spectra after MARZ and pPXF analyses. The dimension of 5 rows and 61 columns represent the results from 5 observations; the first 19 columns are: VISIT number, REPEAT number, top 3 MARZ results and their cross-correlation values, QOP value from MARZ, a flag to indicate that pPXF has been performed, the reduced χ^2 from the pPXF template fit, and the velocity and velocity dispersion measurements for the stellar and gas components and their associated errors; the remaining 42 columns are the gas line flux, error, and signal-to-noise measurements for 14 emission lines: OII3726, OII3729, Hδ, Hγ, Hβ, OIII4959, OIII5007, OI6300, OI6364, NII6548, Hα, NII6583, SII6716, and SII6731. For every new spectrum co-added to the `PRIMARY` extension, MARZ and pPXF are run on the latest co-added spectrum, and the results are saved to the `PRIMARY_SCI` extension. Similarly for the `REPEATS_SCI` extension, each row corresponds to the results obtained from the latest co-added spectrum for the latest REPEAT. For the `VISIT_SIC` extension, each row contains the results for each VISIT observation.

```
Filename: 104.fits
No.   Name          Type         Dimensions
0    PRIMARY        PrimaryHDU   (4588, 3)
1    REPEATS        ImageHDU     (4588, 3, 2)
2    VISITS         ImageHDU     (4588, 3, 5)
3    PRIMARY_SCI    BinTableHDU  5R x 61C
4    REPEATS_SCI    BinTableHDU  5R x 61C
5    VISIT_SCI      BinTableHDU  5R x 61C
6    FIBRES         BinTableHDU  5R x 9C
7    HEADERS        BinTableHDU  5R x 28C
8    TARGET_STATUS  BinTableHDU  5R x 7C
9    QC_SKY         BinTableHDU  5R x 18C
```

Listing 5.1: Data structure of TLDR FITS files; each line describes a FITS extension.

Beyond the spectra and the extracted scientific quantities, other ancillary information are also included in the data product for each galaxy. One such piece of information is the `FIBRES` table. The `FIBRES` table is a FITS file binary table that is part of the raw data produced by the TAIPAN spectrograph. The table contains detailed information such as the fibre used for any particular target, the fibre's on-sky position as well as focal-plane position, fibre ID, fibre rotation angle, fibre positioning success, fibre assignment, target priority, target's program origin, and target's expected magnitude. The exact number of columns for the fibre table is likely to change once TAIPAN commissioning begins. Regardless, TLDR records this information from the raw data and stores them in the `FIBRES` extension for every VISIT. Following similar logic, key header information from each combined reduced data frame is also stored in the `HEADERS` extension. Specific headers to be stored are defined in a machine-readable file as part of the TLDR package; this file simply contains a list of headers-of-interest to be extracted from the original reduced data frame from 2dFdr. The `TARGET_STATUS` is a table that records the progress of observations that need to be carried out for each target. Currently this table records the VISIT and REPEAT number of each observation as well as a series of flags to mark the completion of a target's REPEAT as well as whether or not overall completion of observations for the target has been achieved. The `TARGET_STATUS` table also contains a placeholder for TLDR to input comments as needed. The final extension in the FITS file for each target is the `QC_SKY` extension. This extension records sky subtraction residuals for each target from the combined science frame produced by 2dFdr at a set of predefined sky lines, prior to splicing.

5.8 Future work

The initial version of any piece of software is hardly ever the final version, and TLDR will be no exception and the current state of TLDR should still be considered a prototype. The main tasks of TLDR are to reduce raw data from the TAIPAN spectrograph, perform flux calibration, and extract analyses-ready quantities leveraging MARZ and pPXF. As we have seen from the experiments using the mock data, TLDR has proven to be able to perform these tasks in a sequential order and construct a FITS output for each target galaxy. However, in order to be survey-ready, that is to extract accurate results at large scale with full automation, further development and fine-tuning of the software will need to be carried out.

In section 5.3 we described the first module of TLDR, 2dFdr, which is to be used to reduce the raw data from the TAIPAN spectrograph. However, as the spectrograph and its software are still in its final build stages, it is difficult to get a definitive characterisation of the spectrograph output files. The main components missing are mainly in the ancillary data in the output FITS files. Without these, 2dFdr reduction parameters in the `Taipan.idx` file cannot reach a consensus. Currently, for the mock data, the 2dFdr version used in TLDR is version 6.46, while the latest version of 2dFdr is 7.3. 2dFdr versions between these two versions need to be tested during the TAIPAN commissioning stage. During this testing process, it is specially important to pay attention to the following parameters:

- cosmic-ray rejection method
- heliocentric/baryocentric redshift correction specifications
- flat-field frame tram-line extraction method
- the arc line fitting polynomial order
- throughput calibration using sky observation
- using principal component analysis to remove sky emission line residuals
- reduce data frame combination order
- data splicing central wavelength

While the above items can be tested using the mock data (and indeed they have been tested), when using the actual observed data from the TAIPAN spectrograph these settings are likely to change depending on whether the reduction is being performed for an initial sanity check or for the final official data release. Future development should include plans to outline reduction scenarios and define these parameters accordingly for the intended usage.

Following the optimisation of 2dFdr, the TLDR flux calibration component will also need to be revised over the course of survey commissioning. TLDR flux calibration will rely on the F-star catalogue from the SkyMapper survey. However, at the time of writing this program, the SkyMapper F-star list was not complete. Hence, for our initial testing, we made use of the F-star catalogue from the OzDes survey as a placeholder. Prior to Taipan survey commissioning, this will require an update to provide the most up-to-date photometry input.

In terms of MARZ performance in the Taipan context, although we have seen a solid demonstration in section 5.5, its configuration will also require fine-tuning. Some aspects that can be looked into include an optimal pre-defined redshift range (to limit MARZ to only look for redshift solutions below $z \lesssim 0.1$) and a capacity to use MARZ to obtain redshifts from either one of the two arms of the spectrograph.

As for spectral measurements, there are multiple items that need to be investigated:

- the order of the polynomial used to fit the spectra
- the choice between multiplicative and additive polynomials
- the measurement of the wavelength-dependent spectral resolution
- the optimisation of the spectral template library
- the implementation of multi-Gaussian models for emission line fitting

It is also worth noting that making the emission line spectral measurements is currently the process that takes most time, with a full-frame reduction for 200 spectra taking in total close to 4 hours. In survey operations this poses a challenge for providing real-time feedback should there be the need to re-observe any target the following night. One way to ensure TLDR can be used for real-time feedback is to limit the quantities to be returned by pPXF to only the kinematic parameters and reallocate the emission line fitting process to secondary reduction at later, less time-critical periods.

The ultimate goal of TLDR is to be able to reduce Taipan survey data in real time in a fully automated fashion. In the previous subsection we outlined the need for fine-tuning the data reduction process to ensure the scientific quantities obtained for previously observed targets are consistent with the literature. However it should be possible to simultaneously create a structure for TLDR automation as we fine-tune the software. As it stands, the user's involvement in applying TLDR to reduce data are to establish an instance of TLDR and to call a small number of functions without the need for any decision-making. For automation, the simplest approach would be to implement event triggers for the automation process to impersonate a user. There are also other methods of automation, but they are beyond the scope of this thesis.

The tension between a hardware project such as the commissioning of the TAIPAN spectrograph and a software project as the development of TLDR is that the two projects follow entirely different approaches in their delivery. While it is understandable that for hardware production it is crucial to deliver a built-to-spec finished product that meets the survey requirements at the expense of production time scale, this approach is not suitable for software production. For TLDR, a software package designed to characterise and utilise a specific piece of hardware, iterative development and releases with a short, tight feedback loop is preferable. Currently, lacking actual data from the spectrograph, this feedback loop is incomplete. Therefore the focus has been to test the essential functionality of TLDR components on simulated data, a goal that this chapter demonstrates has been achieved.

Chapter 6

Conclusions

Accurately estimating the stellar mass of galaxies has always been a challenge in extragalactic astronomy (see Courteau et al. 2014, for a review). Over the last few decades, astronomers have come a long way in constructing reliable mass-kinematics scaling relations for specific types of galaxies. These have been used to measure the distances to large numbers of galaxies, proving the importance and applicability of scaling relations in cosmological studies (see Boruah et al. 2020, for an example of the use of scaling relations in the context of H_0 studies). However, we also study these scaling relations because they allow us to characterise galaxy kinematics, their dark matter halos, and their formation, growth and evolution processes. Scaling relations are not only useful for measuring cosmic distances, they also provide benchmarks against which models for the constituents and structures of the Universe can be tested.

Over recent years, the development of integral field spectroscopy (IFS) has enabled innovative recipes for constructing scaling relations that have brought significant improvements to both the Fundamental Plane (FP) and Tully-Fisher (TF) relations (e.g. Scott et al. 2015; Cortese et al. 2016; Bekeraité et al. 2016; Bloom et al. 2017a; Aquino-Ortíz et al. 2018; Tiley et al. 2019; Aquino-Ortíz et al. 2020). For the FP relation, IFS allowed the mathematical modelling of the dynamical mass as well as the inclusion of rotation velocity in the FP. These improvements directly resulted in a stellar mass version of the FP that has minimal intrinsic scatter (see Cappellari 2016, for a review). As for the TF relation, IFS allowed detailed studies of the effective velocity dispersion of the early-type galaxies. Given that effective velocity dispersion correlates with circular velocity at larger radii, it was possible to also bring early-type galaxies onto the relation (Cappellari et al. 2013; Serra et al. 2016) with late-type galaxies. Inspecting the common ingredients of these recipes, the advantage of IFS is clearly that it allows estimation of both the first and second moments of velocity at all points in a galaxy and thereby enables the construction of unified scaling relations for galaxies that are pressure-supported, rotation-supported, or a mixture of both.

The central theme of this thesis revolves around using IFS to provide a suitable combination of the first and second moments of galaxy velocity distributions to construct just such a unified galaxy kinematic scaling relation, specifically the M–S_K scaling relation (where $S_K = \sqrt{KV_{rot}^2 + \sigma^2}$). Previous studies showed the potential of this scaling relation for bringing galaxies of all morphologies onto the same relation through a simple combination of rotation velocity and velocity dispersion (Cortese et al. 2014; Aquino-Ortíz et al. 2018; Gilhuly et al. 2019). In this thesis, we made use of both existing large-scale IFS survey data sets and an additional targeted data set (all described in Chapter 2) to extensively study the properties, applicability, and limitations of the M–$S_{0.5}$ scaling relation.

In Chapter 3 we began the study of the M–$S_{0.5}$ scaling relation by building on the work of Cortese et al. (2014). We used SAMI Galaxy Survey data to show that the $S_{0.5}$ parameter brings galaxies of all morphologies over the mass range $10^{8.5}\,M_\odot \leq M_\star \leq 10^{11.5}\,M_\odot$ onto the same scaling relation with minimal sample pruning. Compared to the Tully-Fisher (TF) and Faber-Jackson (FJ) relations constructed from the same sample, the M–$S_{0.5}$ scaling relation has smaller scatter and is applicable not only to all morphological types of galaxies but also to kinematics derived from either the gas or stellar components of galaxies. The scatter in the scaling relation only depends weakly on the value of K in the S_K parameter; $K = 0.5$ interestingly returns close to the minimum scatter relative to other K values. Unsurprisingly, because $S_{0.5}$ is a combined measure of both rotation and dispersion, it correlates tightly with the more readily measured velocity dispersion within a fixed aperture (e.g. the dispersion in a $3''$-diameter fibre aperture, $\sigma_{3''}$, as measured by SDSS). Crucially, however, $S_{0.5}$ consistently returns less scatter than $\sigma_{3''}$ when used in the mass-kinematics scaling relation. Another important observation made in Chapter 3 is the apparent linearity limit in each of the gas and stellar versions of the M–$S_{0.5}$ scaling relation, where the slope of the relation becomes much steeper. For the SAMI data, these limits occurred at different stellar masses for the gas and stellar versions of the scaling relation, and in both cases the corresponding $S_{0.5}$ values were just above the gas and stellar instrumental resolutions provided by SAMI. This suggested the limits in the relation could be observational artefacts rather than physical features.

To determine if these linearity limits reflect a physical transition or are only due to the spectral resolution limits of the instrument, we therefore designed and completed a dedicated survey with a high spectral resolution IFS instrument ($R = 13500$). To determine the behaviour of the M–$S_{0.5}$ scaling relation, we specifically targeted dwarf galaxies because they lie close to and below the linear limit inferred from SAMI data. In Chapter 4 we present the SHαDE survey, an integral field spectroscopy survey of dwarf galaxies in the local Universe. The goals of SHαDE include the study of galaxy scaling relations, kinematic asymmetries in dwarf galaxies, the link between star formation and ISM turbulence, and angular momentum accretion in dwarf galaxies. SHαDE is very well suited to investigate the behaviour of the M–$S_{0.5}$ scaling relation in the low-mass ($M_\star < 10^{8.8}\,M_\odot$) regime, being designed specifically with this thesis in mind. Using the SHαDE data, we confirmed that there indeed exists a linearity limit to (at least) the gas version of the M–$S_{0.5}$ scaling relation, located at a stellar mass of $M_\star \approx 10^{8.6}\,M_\odot$. The origin of this limit is traced back to an observed intrinsic velocity dispersion floor for the Hα gas at $\sim$20 km s^{-1}. The curvature in the $M_\star$–$S_{0.5}$ scaling relation is reduced if stellar mass ($M_\star$) is replaced with baryonic mass (M_b) by including the estimated gas mass based on the galaxy's star formation rate. Ultimately, by using the halo mass (M_h), estimated under additional strong (though plausible) assumptions, the M_h–$S_{0.5}$ scaling relation was found to be both linear over the whole observed mass range and applicable to galaxies of all morphologies. However, it must be noted that this method of removing the non-linearity in the relation is less than optimal, as it not only relies on strong assumptions but also greatly increases the scatter.

Given the strong correlation demonstrated in Chapter 3 between aperture velocity dispersion from single-fibre spectroscopy (e.g. $\sigma_{3''}$) and the $S_{0.5}$ parameter obtained from IFS, it would be interesting to further investigate this correlation and test the applicability of the M–$\sigma_{3''}$ scaling relation against galaxies of all morphologies using data from large single-fibre surveys obtained with new instruments such as the TAIPAN spectrograph da Cunha et al. (2017). In anticipation of its commissioning, we have demonstrated in Chapter 5 one of the crucial components for a survey using TAIPAN, the TLDR data reduction pipeline. We outlined the reduction processes covered by TLDR, from correction of instrument artefacts to the extraction of scientific quantities and data presentation. Since there was no commissioning data available at the time of this thesis, we used simulated data to test the functionalities of TLDR and validate an initial version of the software. While there is more to be done with TLDR, including fine-tuning the pipeline to the instrument as-built, comprehensive testing, and performance optimisation, these all require real observations to allow the software to accurately cater to the data.

The research presented in this thesis contributes to the understanding of unified galaxy mass-kinematics scaling relations. The findings provide insights on the formation of galaxies and the kinematics of gas and stars as tracers of galaxies' dark matter content. Looking ahead, there are still many question left to be answered. For example, while we have established the existence of a lower limit to the linearity of the gas version of the $M_\star - S_{0.5}$ scaling relation, it is worth exploring the stellar version of the relation with a high-resolution spectrograph to determine whether a similar limit exists and whether it can also be accounted for using baryonic or halo mass versions of the relation. Another interesting area of exploration is to take advantage of the spatial information provided by IFS to construct $S_{0.5}$ at a spaxel level and study the effect of environment within the galaxy. Further work is also needed on the finding of this thesis that there is disagreement between the gas and stellar $S_{0.5}$ parameters, which suggests a difference in the driving forces behind the gas and stellar kinematics. Understanding that difference would be physically interesting as well as an important factor in reconciling the gas and stellar versions of the $M_\star$–$S_{0.5}$ scaling relation.

In conclusion, while there are some significant unanswered questions that require more observations to answer, this thesis shows that a unified mass-kinematics scaling relation for galaxies of all morphologies is close to being fully established.

Appendix A

SHαDE Galaxy Kinematics

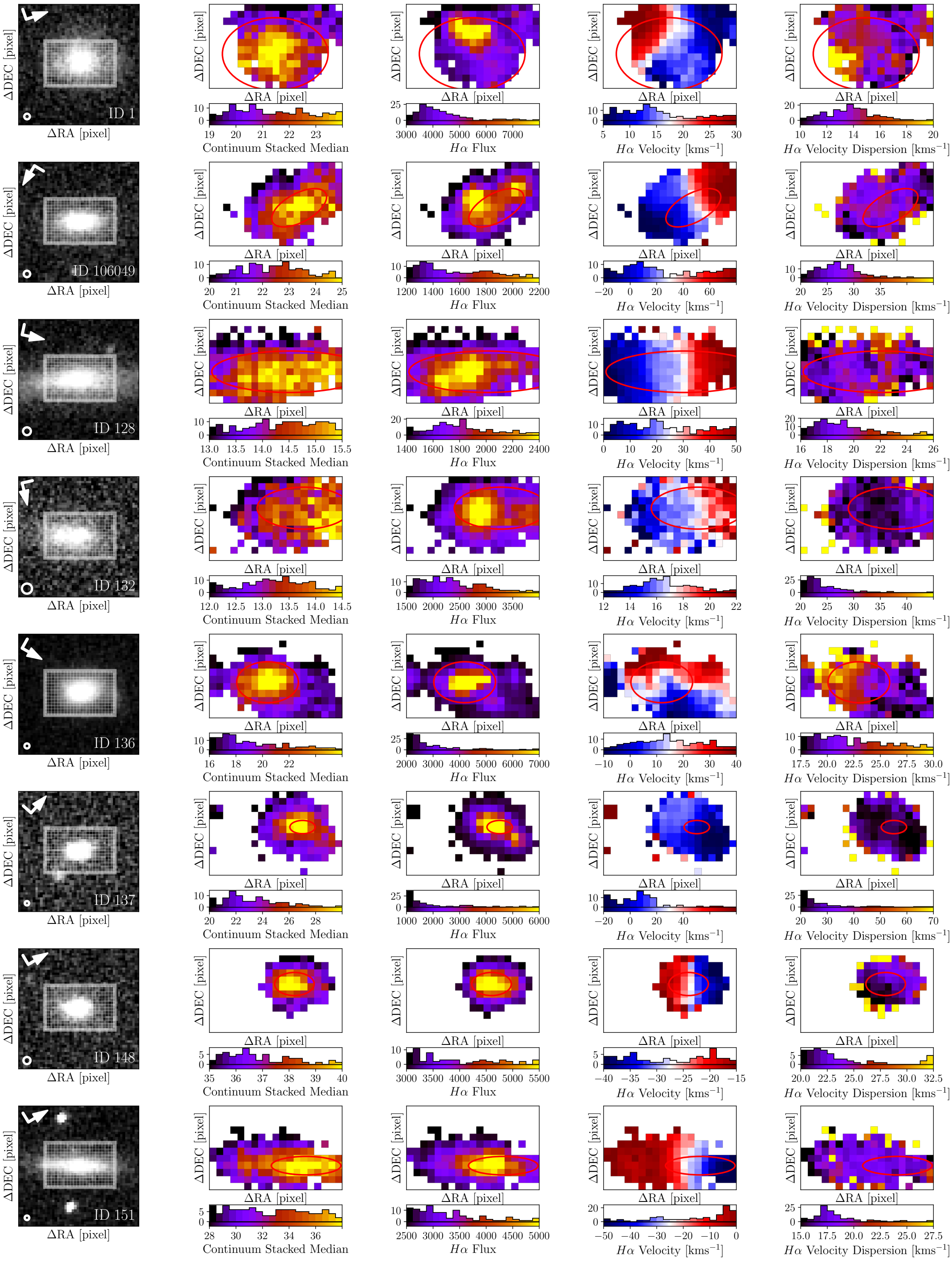
ID 1
ID 106049
ID 128
ID 132
ID 136
ID 137
ID 148
ID 151
ΔDEC [pixel]
ΔRA [pixel]
Continuum Stacked Median
Hα Flux
Hα Velocity [kms^{-1}]
Hα Velocity Dispersion [kms^{-1}]
19 20 21 22 23
3000 4000 5000 6000 7000
5 10 15 20 25 30
10 12 14 16 18 20
20 21 22 23 24 25
1200 1400 1600 1800 2000 2200
−20 0 20 40 60
20 25 30 35
13.0 13.5 14.0 14.5 15.0 15.5
1400 1600 1800 2000 2200 2400
0 10 20 30 40 50
16 18 20 22 24 26
12.0 12.5 13.0 13.5 14.0 14.5
1500 2000 2500 3000 3500
12 14 16 18 20 22
20 25 30 35 40
16 18 20 22
2000 3000 4000 5000 6000 7000
−10 0 10 20 30 40
17.5 20.0 22.5 25.0 27.5 30.0
20 22 24 26 28
1000 2000 3000 4000 5000 6000
−20 0 20 40
20 30 40 50 60 70
35 36 37 38 39 40
3000 3500 4000 4500 5000 5500
−40 −35 −30 −25 −20 −15
20.0 22.5 25.0 27.5 30.0 32.5
28 30 32 34 36
2500 3000 3500 4000 4500 5000
−50 −40 −30 −20 −10 0
15.0 17.5 20.0 22.5 25.0 27.5

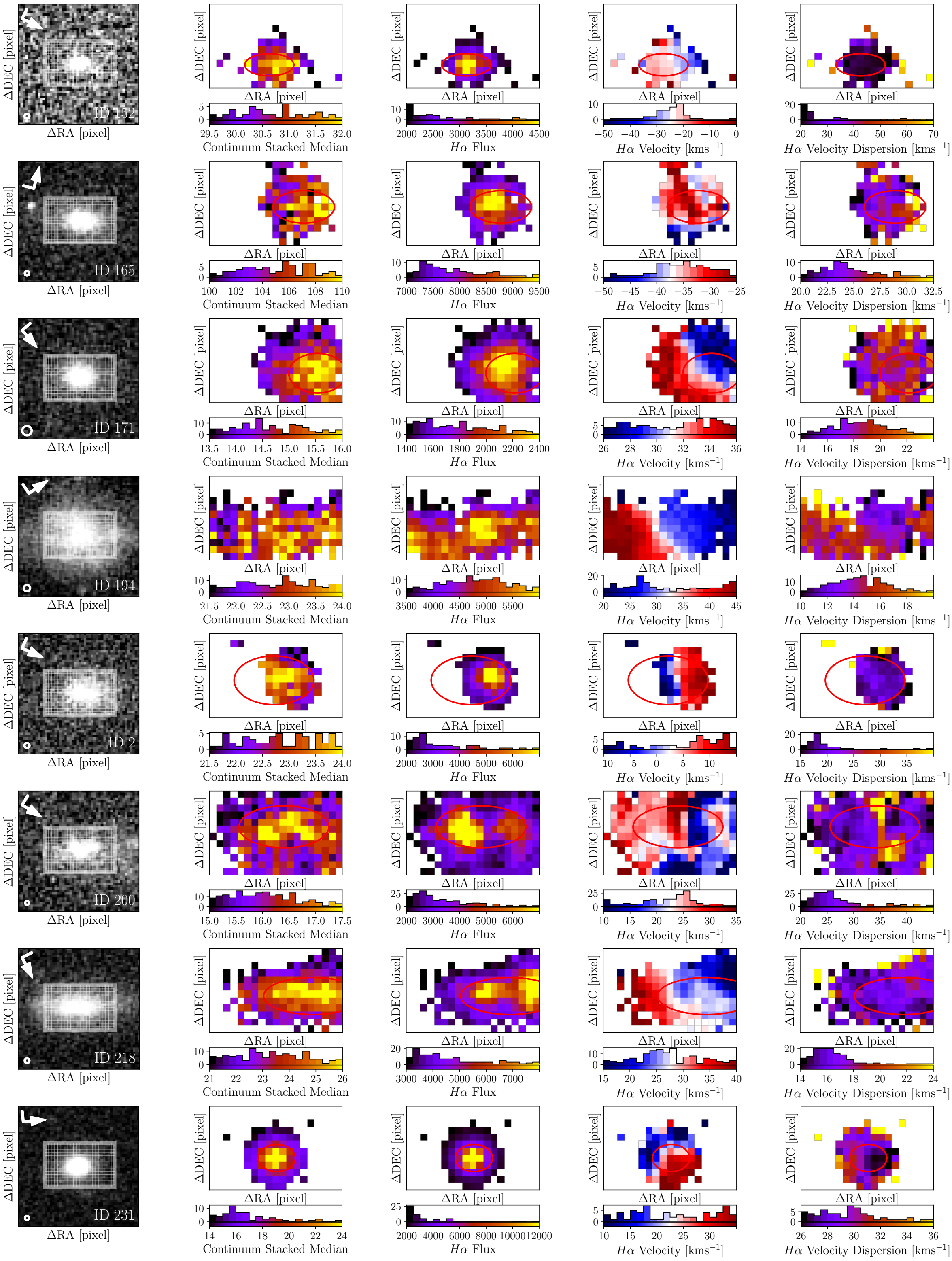
ΔDEC [pixel]
ΔRA [pixel]
ID 152
29.5 30.0 30.5 31.0 31.5 32.0
Continuum Stacked Median
2000 2500 3000 3500 4000 4500
Hα Flux
−50 −40 −30 −20 −10 0
Hα Velocity [kms^{-1}]
20 30 40 50 60 70
Hα Velocity Dispersion [kms^{-1}]
ID 165
100 102 104 106 108 110
7000 7500 8000 8500 9000 9500
−50 −45 −40 −35 −30 −25
20.0 22.5 25.0 27.5 30.0 32.5
ID 171
13.5 14.0 14.5 15.0 15.5 16.0
1400 1600 1800 2000 2200 2400
26 28 30 32 34 36
14 16 18 20 22
ID 194
21.5 22.0 22.5 23.0 23.5 24.0
3500 4000 4500 5000 5500
20 25 30 35 40 45
10 12 14 16 18
ID 2
21.5 22.0 22.5 23.0 23.5 24.0
2000 3000 4000 5000 6000
−10 −5 0 5 10
15 20 25 30 35
ID 200
15.0 15.5 16.0 16.5 17.0 17.5
2000 3000 4000 5000 6000
10 15 20 25 30 35
20 25 30 35 40
ID 218
21 22 23 24 25 26
3000 4000 5000 6000 7000
15 20 25 30 35 40
14 16 18 20 22 24
ID 231
14 16 18 20 22 24
2000 4000 6000 8000 1000012000
10 15 20 25 30
26 28 30 32 34 36

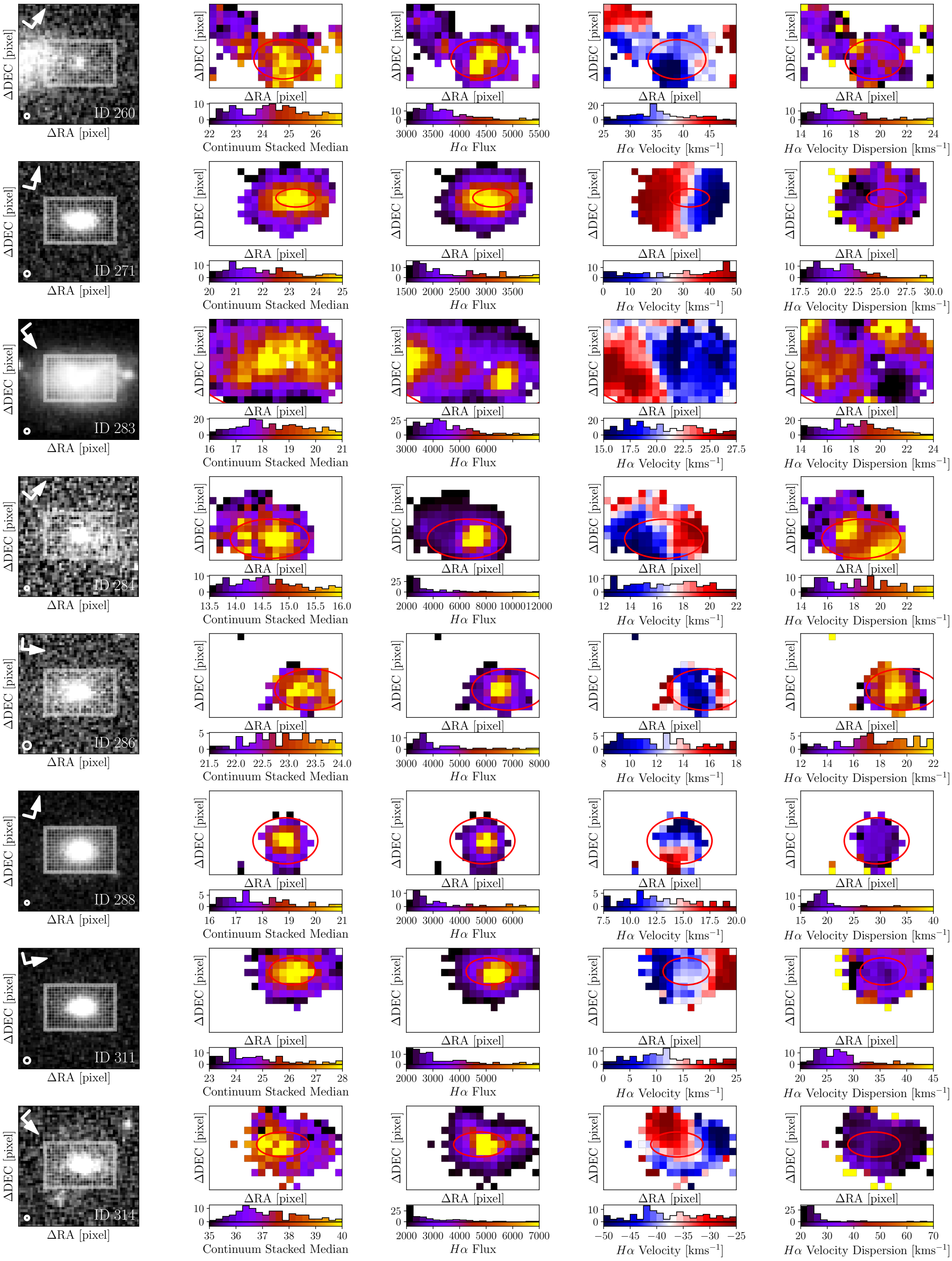
ID 260
ID 271
ID 283
ID 284
ID 286
ID 288
ID 311
ID 314
ΔDEC [pixel]
ΔRA [pixel]
Continuum Stacked Median
Hα Flux
Hα Velocity [kms^{-1}]
Hα Velocity Dispersion [kms^{-1}]
22 23 24 25 26
3000 3500 4000 4500 5000 5500
25 30 35 40 45
14 16 18 20 22 24
20 21 22 23 24 25
1500 2000 2500 3000 3500
0 10 20 30 40 50
17.5 20.0 22.5 25.0 27.5 30.0
16 17 18 19 20 21
3000 4000 5000 6000
15.0 17.5 20.0 22.5 25.0 27.5
14 16 18 20 22 24
13.5 14.0 14.5 15.0 15.5 16.0
2000 4000 6000 8000 10000 12000
12 14 16 18 20 22
14 16 18 20 22
21.5 22.0 22.5 23.0 23.5 24.0
3000 4000 5000 6000 7000 8000
8 10 12 14 16 18
12 14 16 18 20 22
16 17 18 19 20 21
2000 3000 4000 5000 6000
7.5 10.0 12.5 15.0 17.5 20.0
15 20 25 30 35 40
23 24 25 26 27 28
2000 3000 4000 5000
0 5 10 15 20 25
20 25 30 35 40 45
35 36 37 38 39 40
2000 3000 4000 5000 6000 7000
−50 −45 −40 −35 −30 −25
20 30 40 50 60 70

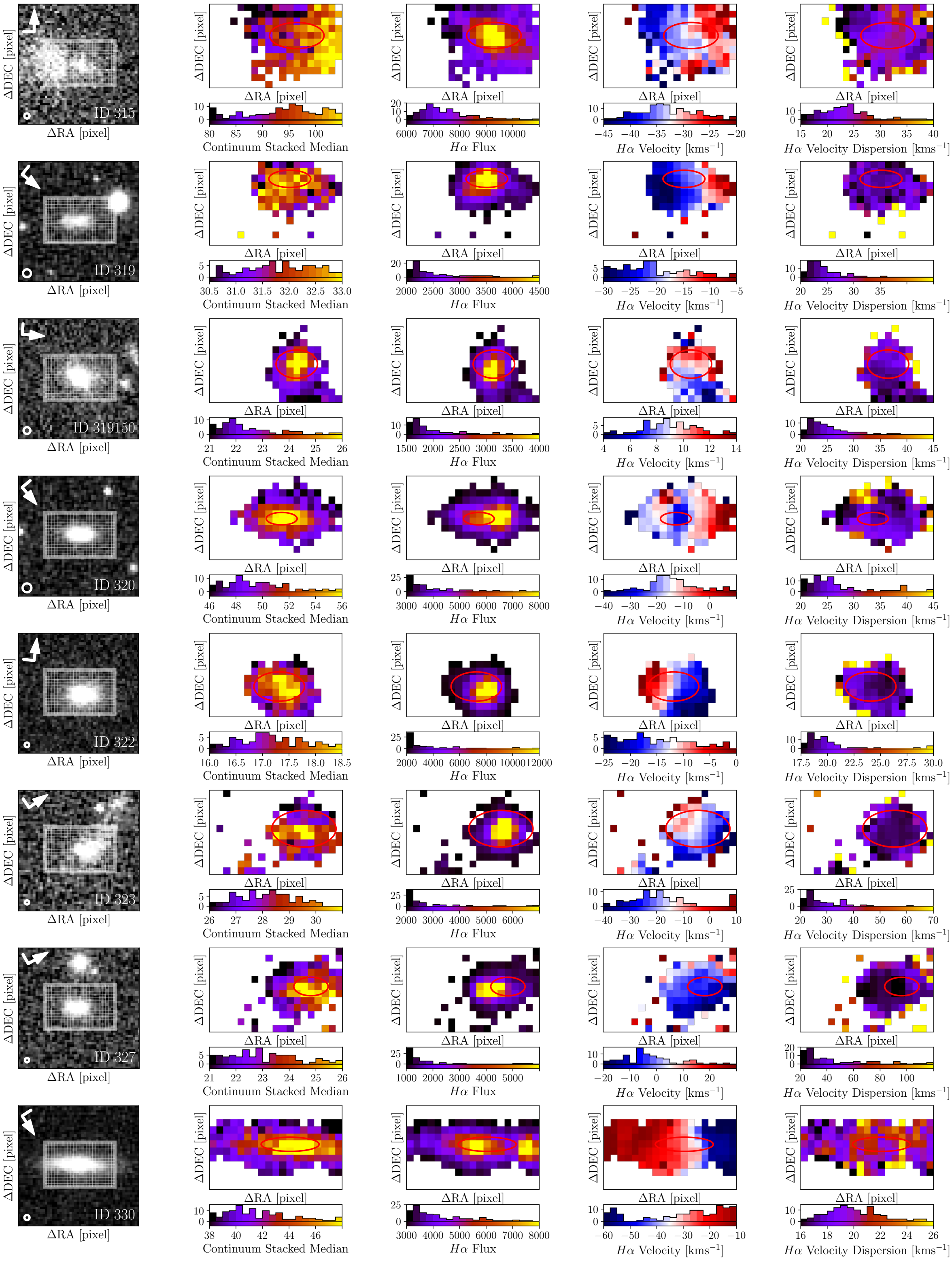
ID 315
ID 319
ID 319150
ID 320
ID 322
ID 323
ID 327
ID 330
ΔDEC [pixel]
ΔRA [pixel]
Continuum Stacked Median
$H\alpha$ Flux
$H\alpha$ Velocity [kms^{-1}]
$H\alpha$ Velocity Dispersion [kms^{-1}]

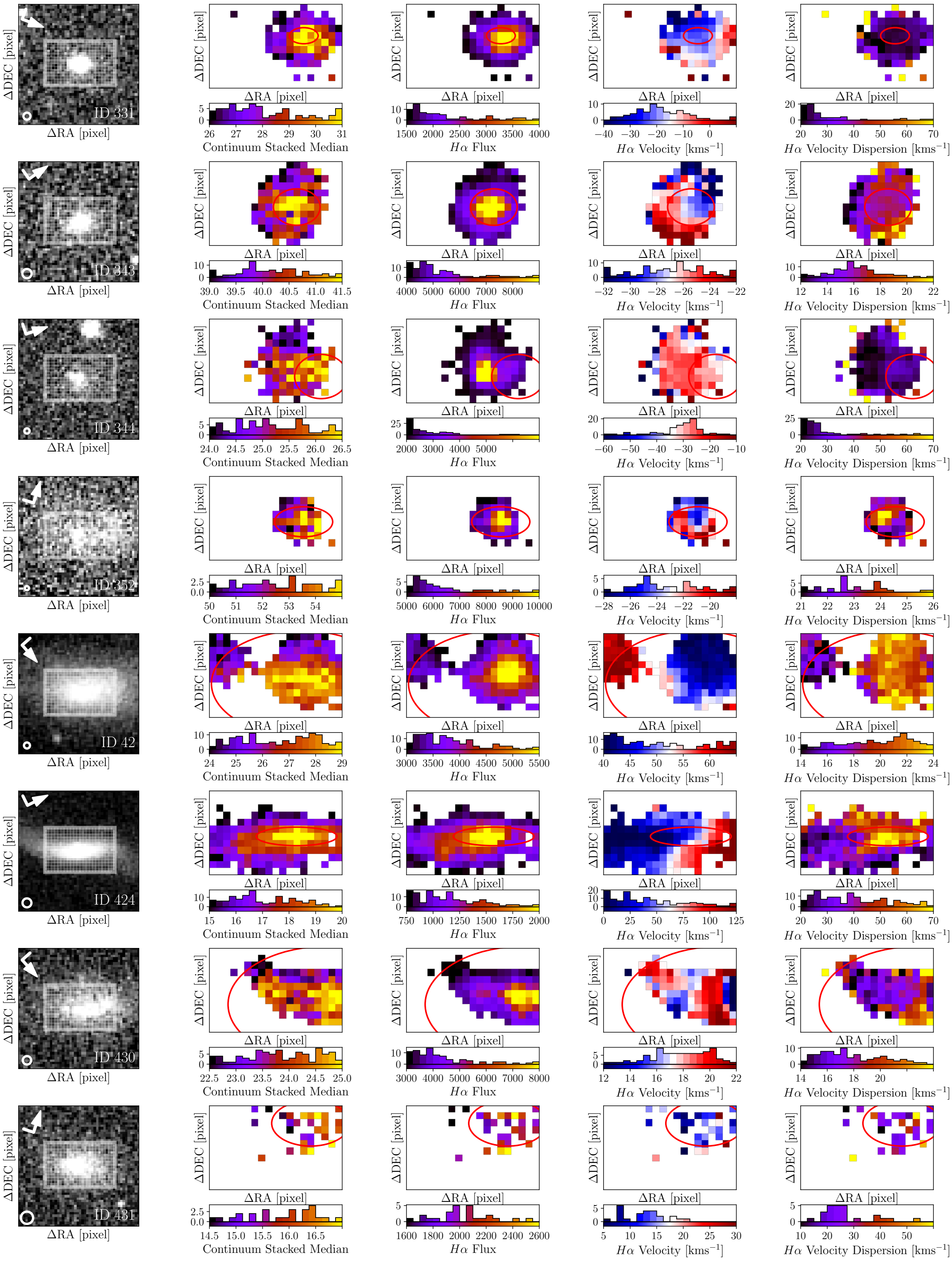
ID 331
ΔDEC [pixel]
ΔRA [pixel]
26 27 28 29 30 31
Continuum Stacked Median
1500 2000 2500 3000 3500 4000
Hα Flux
−40 −30 −20 −10 0
Hα Velocity [kms^{-1}]
20 30 40 50 60 70
Hα Velocity Dispersion [kms^{-1}]
ID 343
39.0 39.5 40.0 40.5 41.0 41.5
4000 5000 6000 7000 8000
−32 −30 −28 −26 −24 −22
12 14 16 18 20 22
ID 344
24.0 24.5 25.0 25.5 26.0 26.5
2000 3000 4000 5000
−60 −50 −40 −30 −20 −10
20 30 40 50 60 70
ID 352
50 51 52 53 54
5000 6000 7000 8000 9000 10000
−28 −26 −24 −22 −20
21 22 23 24 25 26
ID 42
24 25 26 27 28 29
3000 3500 4000 4500 5000 5500
40 45 50 55 60
14 16 18 20 22 24
ID 424
15 16 17 18 19 20
750 1000 1250 1500 1750 2000
0 25 50 75 100 125
20 30 40 50 60 70
ID 430
22.5 23.0 23.5 24.0 24.5 25.0
3000 4000 5000 6000 7000 8000
12 14 16 18 20 22
14 16 18 20
ID 431
14.5 15.0 15.5 16.0 16.5
1600 1800 2000 2200 2400 2600
5 10 15 20 25 30
10 20 30 40 50

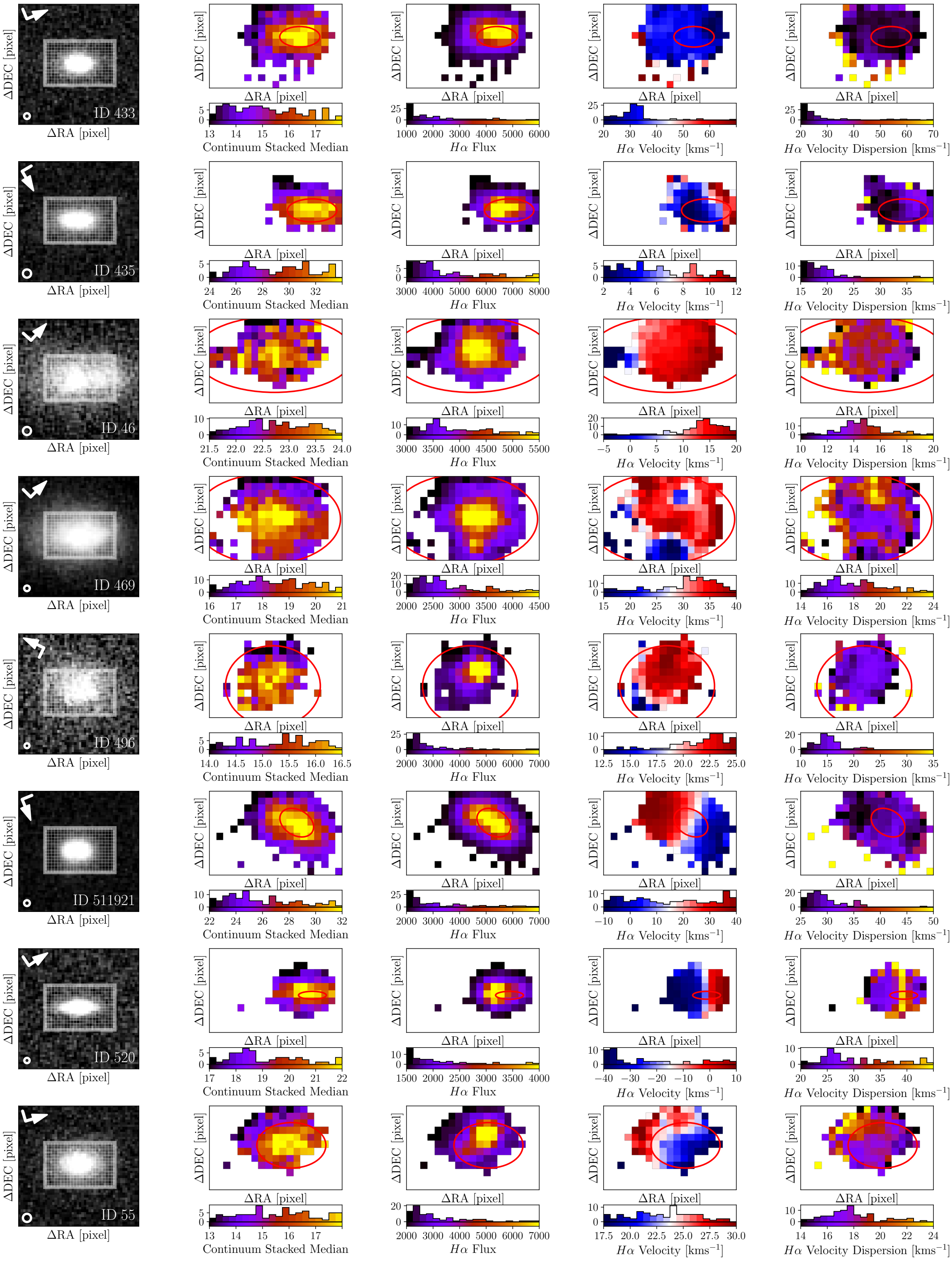
ID 433
ID 435
ID 46
ID 469
ID 496
ID 511921
ID 520
ID 55
ΔDEC [pixel]
ΔRA [pixel]
Continuum Stacked Median
Hα Flux
Hα Velocity [kms^{-1}]
Hα Velocity Dispersion [kms^{-1}]
13 14 15 16 17
1000 2000 3000 4000 5000 6000
20 30 40 50 60
20 30 40 50 60 70
24 26 28 30 32
3000 4000 5000 6000 7000 8000
2 4 6 8 10 12
15 20 25 30 35
21.5 22.0 22.5 23.0 23.5 24.0
3000 3500 4000 4500 5000 5500
−5 0 5 10 15 20
10 12 14 16 18 20
16 17 18 19 20 21
2000 2500 3000 3500 4000 4500
15 20 25 30 35 40
14 16 18 20 22 24
14.0 14.5 15.0 15.5 16.0 16.5
2000 3000 4000 5000 6000 7000
12.5 15.0 17.5 20.0 22.5 25.0
10 15 20 25 30 35
22 24 26 28 30 32
−10 0 10 20 30 40
25 30 35 40 45 50
17 18 19 20 21 22
1500 2000 2500 3000 3500 4000
−40 −30 −20 −10 0 10
20 25 30 35 40
17.5 20.0 22.5 25.0 27.5 30.0

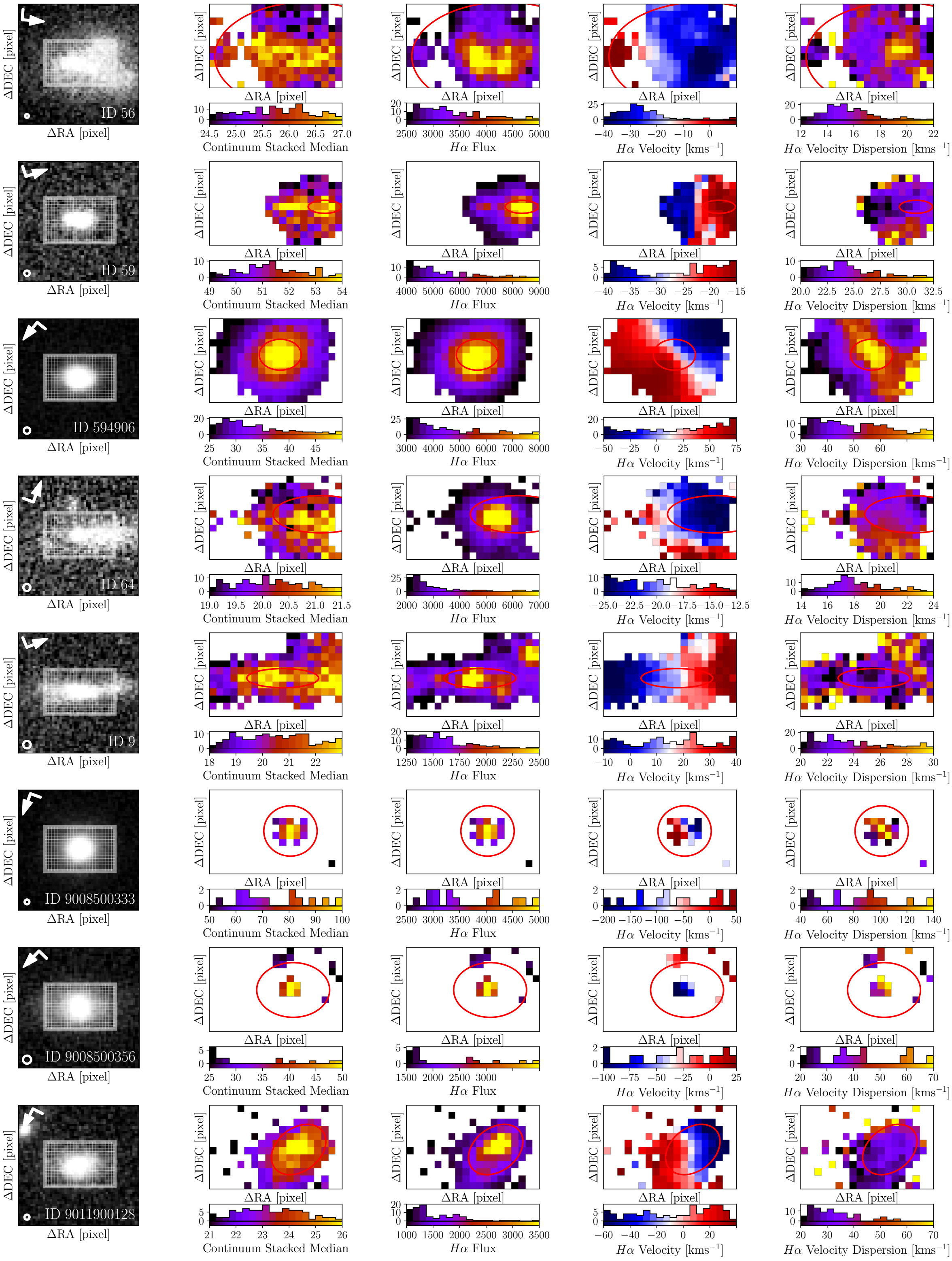
ID 56
ID 59
ID 594906
ID 64
ID 9
ID 9008500333
ID 9008500356
ID 9011900128
ΔDEC [pixel]
ΔRA [pixel]
24.5 25.0 25.5 26.0 26.5 27.0
Continuum Stacked Median
2500 3000 3500 4000 4500 5000
Hα Flux
−40 −30 −20 −10 0
Hα Velocity [kms^{-1}]
12 14 16 18 20 22
Hα Velocity Dispersion [kms^{-1}]
49 50 51 52 53 54
4000 5000 6000 7000 8000 9000
−40 −35 −30 −25 −20 −15
20.0 22.5 25.0 27.5 30.0 32.5
25 30 35 40 45
3000 4000 5000 6000 7000 8000
−50 −25 0 25 50 75
30 40 50 60
19.0 19.5 20.0 20.5 21.0 21.5
2000 3000 4000 5000 6000 7000
−25.0 −22.5 −20.0 −17.5 −15.0 −12.5
14 16 18 20 22 24
18 19 20 21 22
1250 1500 1750 2000 2250 2500
−10 0 10 20 30 40
20 22 24 26 28 30
50 60 70 80 90 100
2500 3000 3500 4000 4500 5000
−200 −150 −100 −50 0 50
40 60 80 100 120 140
25 30 35 40 45 50
1500 2000 2500 3000
−100 −75 −50 −25 0 25
20 30 40 50 60 70
21 22 23 24 25 26
1000 1500 2000 2500 3000 3500
−60 −40 −20 0 20
20 30 40 50 60 70

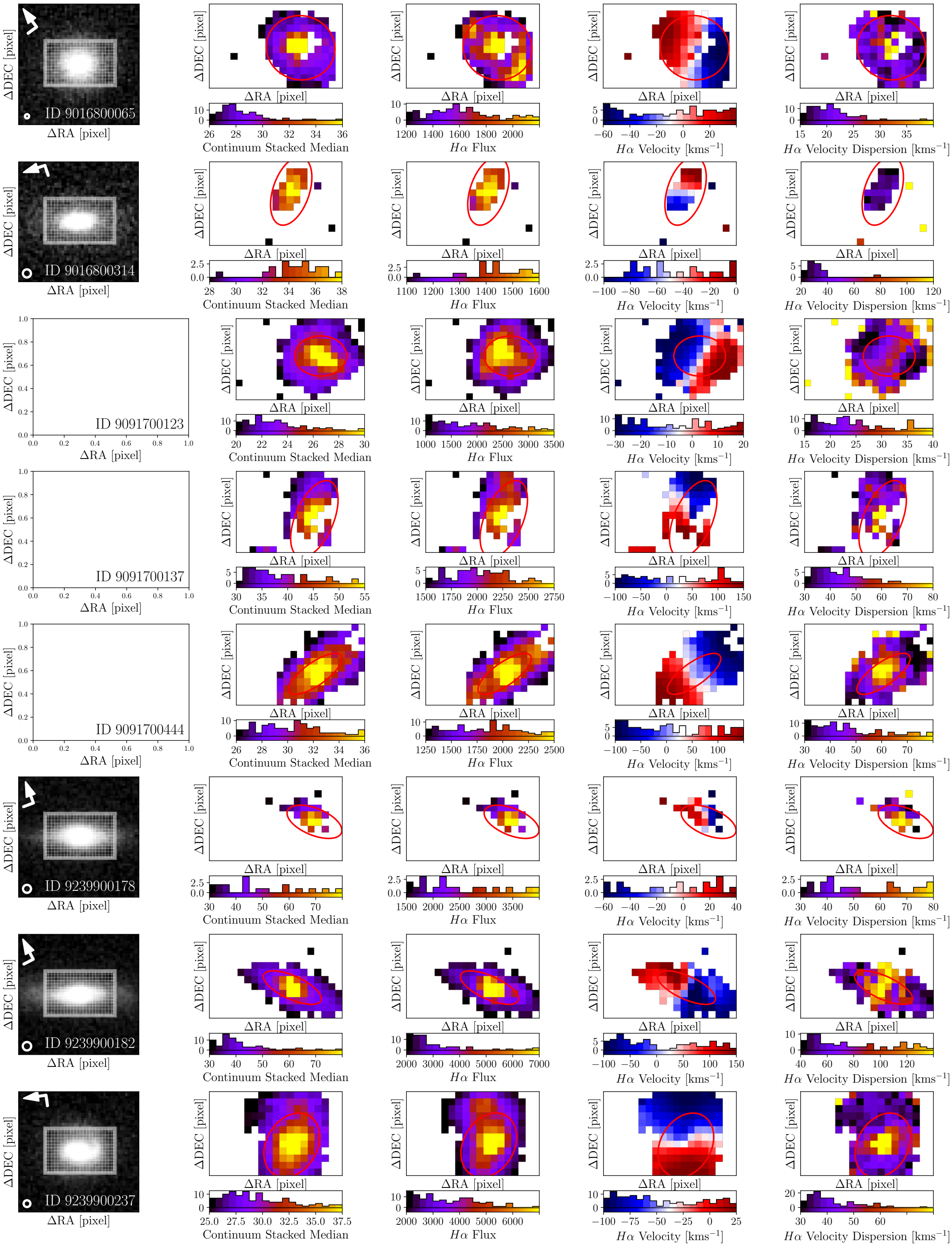
ID 9016800065
ΔDEC [pixel]
ΔRA [pixel]
10 0
26 28 30 32 34 36
Continuum Stacked Median
10 0
1200 1400 1600 1800 2000
Hα Flux
5 0
−60 −40 −20 0 20
Hα Velocity [kms^{-1}]
10 0
15 20 25 30 35
Hα Velocity Dispersion [kms^{-1}]
ID 9016800314
2.5 0.0
28 30 32 34 36 38
Continuum Stacked Median
2.5 0.0
1100 1200 1300 1400 1500 1600
Hα Flux
2.5 0.0
−100 −80 −60 −40 −20 0
Hα Velocity [kms^{-1}]
5 0
20 40 60 80 100 120
Hα Velocity Dispersion [kms^{-1}]
1.0 0.8 0.6 0.4 0.2 0.0
0.0 0.2 0.4 0.6 0.8 1.0
ID 9091700123
10 0
20 22 24 26 28 30
Continuum Stacked Median
10 0
1000 1500 2000 2500 3000 3500
Hα Flux
10 0
−30 −20 −10 0 10 20
Hα Velocity [kms^{-1}]
10 0
15 20 25 30 35 40
Hα Velocity Dispersion [kms^{-1}]
ID 9091700137
5 0
30 35 40 45 50 55
Continuum Stacked Median
5 0
1500 1750 2000 2250 2500 2750
Hα Flux
5 0
−100 −50 0 50 100 150
Hα Velocity [kms^{-1}]
5 0
30 40 50 60 70 80
Hα Velocity Dispersion [kms^{-1}]
ID 9091700444
10 0
26 28 30 32 34 36
Continuum Stacked Median
10 0
1250 1500 1750 2000 2250 2500
Hα Flux
5 0
−100 −50 0 50 100
Hα Velocity [kms^{-1}]
10 0
30 40 50 60 70
Hα Velocity Dispersion [kms^{-1}]
ID 9239900178
2.5 0.0
30 40 50 60 70
Continuum Stacked Median
2.5 0.0
1500 2000 2500 3000 3500
Hα Flux
2.5 0.0
−60 −40 −20 0 20 40
Hα Velocity [kms^{-1}]
2.5 0.0
30 40 50 60 70 80
Hα Velocity Dispersion [kms^{-1}]
ID 9239900182
10 0
30 40 50 60 70
Continuum Stacked Median
10 0
2000 3000 4000 5000 6000 7000
Hα Flux
5 0
−100 −50 0 50 100 150
Hα Velocity [kms^{-1}]
10 0
40 60 80 100 120
Hα Velocity Dispersion [kms^{-1}]
ID 9239900237
10 0
25.0 27.5 30.0 32.5 35.0 37.5
Continuum Stacked Median
10 0
2000 3000 4000 5000 6000
Hα Flux
10 0
−100 −75 −50 −25 0 25
Hα Velocity [kms^{-1}]
20 0
30 40 50 60
Hα Velocity Dispersion [kms^{-1}]

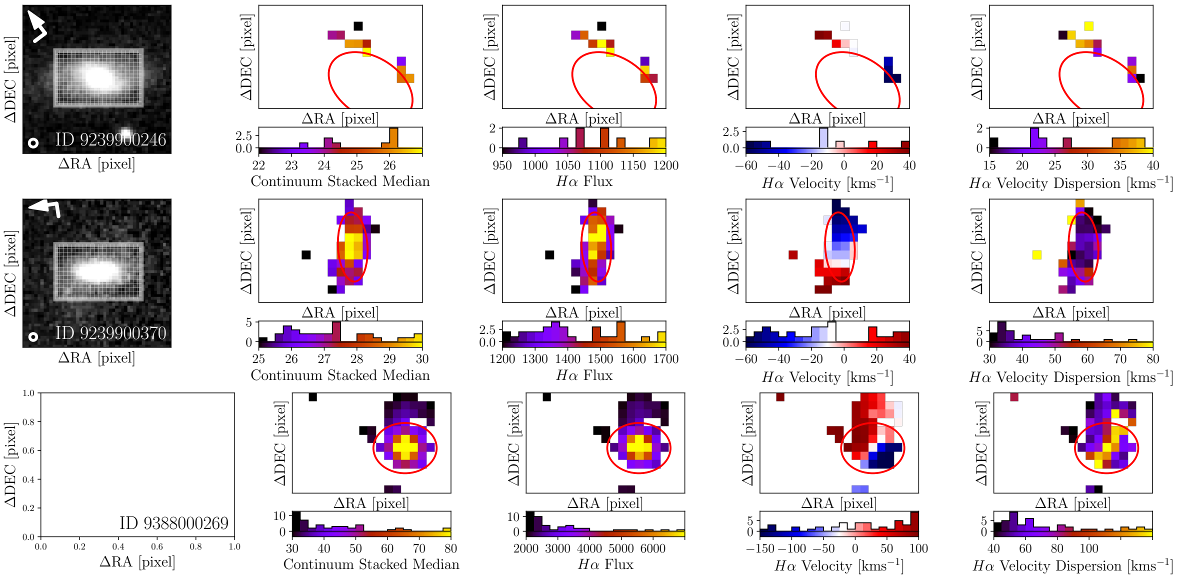

Figure A.1: SHαDE survey galaxy kinematic maps.

References

AAO Software Team 2015, 2dfdr: Data reduction software (ascl:1505.015) 113

Aguado D. S., et al., 2019, ApJS, 240, 23 20

Ahn C. P., et al., 2012, ApJS, 203, 21 37

Alam S., et al., 2015, ApJS, 219, 12 73

Allen J. T., et al., 2014, SAMI: Sydney-AAO Multi-object Integral field spectrograph pipeline, Astrophysics Source Code Library (ascl:1407.006) 32

Allen J. T., Croom S. M., Konstantopoulos I. S., et al 2015, MNRAS, 446, 1567 22, 32

Amorín R., Aguerri J. A. L., Muñoz-Tuñón C., Cairós L. M., 2009, A&A, 501, 75 67

Aquino-Ortíz E., Valenzuela O., Sánchez S. F., Hernández-Toledo H., et al 2018, MNRAS, 479, 2133 xiv, xx, 15, 30, 33, 38, 39, 40, 45, 54, 56, 59, 60, 69, 92, 99, 134, 135

Aquino-Ortíz E., et al., 2020, ApJ, 900, 109 26, 134

Artale M. C., et al., 2017, MNRAS, 470, 1771 64

Avila-Reese V., Zavala J., Firmani C., Hernández-Toledo H. M., 2008, AJ, 136, 1340 14, 28

Bacchini C., Fraternali F., Iorio G., Pezzulli G., Marasco A., Nipoti C., 2020, arXiv e-prints, p. arXiv:2006.10764 107

Bacon R., et al., 2001, MNRAS, 326, 23 20

Baldry I. K., et al., 2014, MNRAS, 441, 2440 123

Barat D., et al., 2019, MNRAS, 487, 2924 xx, xxv, 15, 16, 17, 69, 89, 90, 92, 94, 95, 97, 99

Barat D., D'Eugenio F., Colless M., Sweet S. M., Groves B., Cortese L., 2020, MNRAS, 16, 17, 23

Barnes J., Efstathiou G., 1987, ApJ, 319, 575 72

Behroozi P. S., Wechsler R. H., Conroy C., 2013, ApJ, 770, 57 13, 69

Bekeraité S., et al., 2016, A&A, 593, A114 134

Bell E. F., et al., 2004, ApJ, 608, 752 7

Bernardi M., Domínguez Sánchez H., Margalef-Bentabol B., Nikakhtar F., Sheth R. K., 2020, MNRAS, 494, 5148 8

Bertin E., 2011, in Evans I. N., Accomazzi A., Mink D. J., Rots A. H., eds, Astronomical

Society of the Pacific Conference Series Vol. 442, Astronomical Data Analysis Software and Systems XX. p. 435 84

Bertin G., Ciotti L., Del Principe M., 2002, A&A, 386, 149 7, 8

Bigiel F., Leroy A., Walter F., Brinks E., de Blok W. J. G., Madore B., Thornley M. D., 2008, AJ, 136, 2846 99

Binney J., Tremaine S., 2008, Galactic Dynamics: Second Edition. Princeton University Press 9, 10, 47, 58

Bland-Hawthorn J., et al., 2011, Optics Express, 19, 2649 22, 31

Blecha A., Cayatte V., North P., Royer F., Simond G., 2000, in Iye M., Moorwood A. F., eds, Society of Photo-Optical Instrumentation Engineers (SPIE) Conference Series Vol. 4008, Proc. SPIE. pp 467–474, doi:10.1117/12.395507 78

Bloom J. V., et al., 2017a, MNRAS, 465, 123 29, 70, 134

Bloom J. V., et al., 2017b, MNRAS, 472, 1809 xx, 70, 92, 93, 101

Bloom J. V., et al., 2018, MNRAS, 476, 2339 70

Bond J. R., Cole S., Efstathiou G., Kaiser N., 1991, ApJ, 379, 440 3

Bondi H., Gold T., 1948, MNRAS, 108, 252 2

Booth C. M., Schaye J., 2009, MNRAS, 398, 53 64

Borriello A., Salucci P., Danese L., 2003, MNRAS, 341, 1109 8

Boruah S. S., Hudson M. J., Lavaux G., 2020, arXiv e-prints, p. arXiv:2010.01119 134

Boselli A., Gavazzi G., 2006, PASP, 118, 517 10

Bournaud F., Elmegreen B. G., Teyssier R., Block D. L., Puerari I., 2010, MNRAS, 409, 1088 106

Bournaud F., et al., 2014, ApJ, 780, 57 106

Branch M., Coleman T., Li Y., 1999, SIAM Journal on Scientific Computing, 21 81

Brown D. M., et al., 2014, in Navarro R., Cunningham C. R., Barto A. A., eds, Society of Photo-Optical Instrumentation Engineers (SPIE) Conference Series Vol. 9151, Advances in Optical and Mechanical Technologies for Telescopes and Instrumentation. p. 91511A (`arXiv:1805.10761`), doi:10.1117/12.2055594 25

Bryant J. J., O'Byrne J. W., Bland-Hawthorn J., Leon-Saval S. G., 2011, MNRAS, 415, 2173 22

Bryant J. J., Bland-Hawthorn J., Fogarty L. M. R., Lawrence J. S., Croom S. M., 2014, MNRAS, 438, 869 31, 84

Bryant J. J., et al., 2015, MNRAS, 447, 2857 30, 31, 32, 65

Bryant J. J., et al., 2016, in Ground-based and Airborne Instrumentation for Astronomy VI. p. 99081F (`arXiv:1608.03921`), doi:10.1117/12.2230740 56

Buckley M. R., Peter A. H. G., 2018, Phys. Rep., 761, 1 12

Bullock J. S., Boylan-Kolchin M., 2017, ARA&A, 55, 343 12

Bullock J. S., Dekel A., Kolatt T. S., Kravtsov A. V., Klypin A. A., Porciani C., Primack J. R., 2001, ApJ, 555, 240 3

Bundy K., et al., 2015, ApJ, 798, 7 20, 65

Campbell L. A., et al., 2014, MNRAS, 443, 1231 9, 25

Cannon J. M., et al., 2016, AJ, 152, 202 68

Cappellari M., 2002, MNRAS, 333, 400 84, 85

Cappellari M., 2012, arXiv e-prints, p. arXiv:1211.7009 14

Cappellari M., 2016, ARA&A, 54, 597 8, 135

Cappellari M., 2017, MNRAS, 466, 798 82, 113

Cappellari M., Emsellem E., 2004, PASP, 116, 138 32, 125

Cappellari M., et al., 2007, MNRAS, 379, 418 7

Cappellari M., et al., 2011, MNRAS, 413, 813 14, 20

Cappellari M., et al., 2013, MNRAS, 432, 1709 14, 69, 135

Cappellari M., et al., 2015, ApJ, 804, L21 104

Casoli F., et al., 1998, A&A, 331, 451 10

Catelan P., Theuns T., 1996a, MNRAS, 282, 436 72

Catelan P., Theuns T., 1996b, MNRAS, 282, 455 72

Catinella B., Haynes M. P., Giovanelli R., 2005, AJ, 130, 1037 33, 89

Catinella B., et al., 2012, MNRAS, 420, 1959 28, 36

Chabrier G., 2003, PASP, 115, 763 23, 66

Childress M. J., et al., 2017, MNRAS, 472, 273 113, 115, 124

Chu Y.-H., Kennicutt Robert C. J., 1994, ApJ, 425, 720 107

Ciotti L., Lanzoni B., Renzini A., 1996, MNRAS, 282, 1 8

Colless M., et al., 2001, MNRAS, 328, 1039 111, 115

Cortese L., Fogarty L. M. R., Ho I.-T., Bekki K., 2014, ApJ, 795, L37 xiv, xx, 15, 30, 33, 38, 39, 40, 45, 47, 54, 55, 60, 68, 69, 89, 92, 99, 135

Cortese L., et al., 2016, MNRAS, 463, 170 37, 72, 134

Cortese L., Catinella B., Cook R. H. W., Janowiecki S., 2020, MNRAS, 494, L42 68

Courteau S., Rix H.-W., 1999, ApJ, 513, 561 14

Courteau S., Dutton A. A., van den Bosch F. C., MacArthur L. A., Dekel A., McIntosh D. H., Dale D. A., 2007, ApJ, 671, 203 28

Courteau S., et al., 2014, Reviews of Modern Physics, 86, 47 13, 134

Courtois H. M., Tully R. B., 2012, ApJ, 749, 174 67

Covington M. D., Kassin S. A., Dutton A. A., et al 2010, The Astrophysical Journal, 170, 279 30, 54, 59

Croom S. M., et al., 2012, MNRAS, 421, 872 16, 22, 30, 32, 65

DESI Collaboration et al., 2016, arXiv e-prints, p. arXiv:1611.00036 113

D'Eugenio F., Houghton R. C. W., Davies R. L., Dalla Bontà E., 2013, MNRAS, 429, 1258 21

D'Onofrio M., Capaccioli M., Caon N., 1994, MNRAS, 271, 523 7

Dekel A., Woo J., 2003, MNRAS, 344, 1131 72

Desmond H., 2017, MNRAS, 464, 4160 29, 69

Desmond H., Wechsler R. H., 2015, MNRAS, 454, 322 67

Desmond H., Katz H., Lelli F., McGaugh S., 2019, MNRAS, 484, 239 68

Di Cintio A., Lelli F., 2015, Monthly Notices of the Royal Astronomical Society: Letters, 456, L127 69

Djorgovski S., Davis M., 1987, ApJ, 313, 59 8, 28

Dressler A., Lynden-Bell D., Burstein D., Davies R. L., Faber S. M., Terlevich R., Wegner G., 1987, ApJ, 313, 42 8, 28

Driver S. P., et al., 2011, MNRAS, 413, 971 22

Dubois Y., et al., 2014, MNRAS, 444, 1453 64

Duc P.-A., et al., 2011, MNRAS, 417, 863 6

Dutton A. A., 2012, MNRAS, 424, 3123 68

Dutton A. A., Macciò A. V., Buck T., Dixon K. L., Blank M., Obreja A., 2019, MNRAS, 486, 655 64

Eisenstein D. J., et al., 2011, AJ, 142, 72 73

Elmegreen B. G., Zhang H.-X., Hunter D. A., 2012, ApJ, 747, 105 70

Emsellem E., Monnet G., Bacon R., 1994, A&A, 285, 723 33, 84

Faber S. M., Gallagher J. S., 1979, ARA&A, 17, 135 11

Faber S. M., Jackson R. E., 1976, ApJ, 204, 668 7, 28, 68

Fall S. M., 1983, in Athanassoula E., ed., IAU Symposium Vol. 100, Internal Kinematics and Dynamics of Galaxies. pp 391–398 29, 71

Fall S. M., Romanowsky A. J., 2013, ApJ, 769, L26 72, 73

Fall S. M., Romanowsky A. J., 2018, ApJ, 868, 133 72

Farrell T., Birchall M., Croom S., Lidman C., 2019, in Molinaro M., Shortridge K., Pasian F., eds, Astronomical Society of the Pacific Conference Series Vol. 521, Astronomical Data Analysis Software and Systems XXVI. p. 675 117

Federrath C., Klessen R. S., 2012, ApJ, 761, 156 71

Federrath C., et al., 2017, MNRAS, 468, 3965 97

Ferrarese L., et al., 2006, ApJS, 164, 334 7

Forbes D. A., Ponman T. J., Brown R. J. N., 1998, ApJ, 508, L43 8

Foreman-Mackey D., Hogg D. W., Lang D., Goodman J., 2013, PASP, 125, 306 42

Foster C., et al., 2017, MNRAS, 472, 966 40

Foucaud S., Conselice C. J., Hartley W. G., Lane K. P., Bamford S. P., Almaini O., Bundy K., 2010, MNRAS, 406, 147 97

Freeman K. C., 1970, ApJ, 160, 811 11

Frenk C. S., White S. D. M., 2012, Annalen der Physik, 524, 507 13

Gaia Collaboration et al., 2016, A&A, 595, A1 75

Gaia Collaboration et al., 2018, A&A, 616, A1 75

Gallazzi A., Charlot S., Brinchmann J., White S. D. M., Tremonti C. A., 2005, MNRAS, 362, 41 7

Gaspari M., Brighenti F., Temi P., 2012, MNRAS, 424, 190 47

Gilhuly C., Courteau S., Sánchez S. F., 2019, MNRAS, 482, 1427 15, 69, 99, 135

Gillingham P., Smoker J., Colless M., Kaufer A., 2004, in Moorwood A. F. M., Iye M., eds, Society of Photo-Optical Instrumentation Engineers (SPIE) Conference Series Vol. 5492, Ground-based Instrumentation for Astronomy. pp 643–650, doi:10.1117/12.550966 21

Gioia I. M., Fabbiano G., 1987, ApJS, 63, 771 9

Glazebrook K., 2013, Publ. Astron. Soc. Australia, 30, e056 68, 106

Goldbaum N. J., Krumholz M. R., Forbes J. C., 2015, ApJ, 814, 131 106

Graham A., Colless M., 1997, MNRAS, 287, 221 8

Graham A. W., Guzmán R., 2003, AJ, 125, 2936 7

Graham A. W., Janz J., Penny S. J., Chilingarian Igor V.and Ciambur B. C., 2017, Apj, 840, 68 51

Green A. W., et al., 2010, Nature, 467, 684 71, 106

Green A. W., et al., 2014, MNRAS, 437, 1070 106

Green A. W., et al., 2018, MNRAS, 475, 716 20

Gunn J. E., et al., 2006, AJ, 131, 2332 111

Hafen Z., et al., 2019, MNRAS, 488, 1248 65

Hall M., Courteau S., Dutton A. A., McDonald M., Zhu Y., 2012, MNRAS, 425, 2741 14

Hanuschik R. W., 2003, A&A, 407, 1157 xxv, 80, 81

Hatfield P., Laigle C., Jarvis M., Devriendt J., Davidzon I., Ilbert O., Pichon C., Dubois Y., 2019, arXiv e-prints, p. arXiv:1909.03843 64

Hill J. M., Angel J. R. P., Scott J. S., Lindley D., Hintzen P., 1980, ApJ, 242, L69 111

Hinton S. R., Davis T. M., Lidman C., Glazebrook K., Lewis G. F., 2016, Astronomy and Computing, 15, 61 113, 123, 124

Ho I.-T., Kewley L. J., Dopita M. A., 2014, MNRAS, 444, 3894 32

Hopkins P. F., Kereš D., Oñorbe J., Faucher-Giguère C.-A., Quataert E., Murray N., Bullock J. S., 2014, MNRAS, 445, 581 64

Horne K., 1986, PASP, 98, 609 79

Hoyle F., 1948, MNRAS, 108, 372 2

Hubble E. P., 1926, ApJ, 64, 321 4

Hubble E., 1929, Proceedings of the National Academy of Science, 15, 168 2

Hubble E. P., 1936, Realm of the Nebulae. Yale University Press 5

Humphrey P. J., Buote D. A., 2010, MNRAS, 403, 2143 8

Hunter D. A., et al., 2012, AJ, 144, 134 65, 67

Ianjamasimanana R., de Blok W. J. G., Walter F., Heald G. H., 2012, AJ, 144, 96 105

Iodice E., Arnaboldi M., Bournaud F., Combes F., 2003, ApJ, 585, 730 29

Iorio G., Fraternali F., Nipoti C., Di Teodoro E., Read J. I., Battaglia G., 2017, MNRAS, 466, 4159 15, 67

Jiang F., et al., 2019, MNRAS, 488, 4801 72

Jing Y. P., Suto Y., 2002, ApJ, 574, 538 3

Jones D. H., et al., 2004, MNRAS, 355, 747 111, 115

Jorgensen I., Franx M., Kjaergaard P., 1996, MNRAS, 280, 167 8

Kalberla P. M. W., Dedes L., Kerp J., Haud U., 2007, A&A, 469, 511 10

Kassin S. A., et al., 2007, ApJ, 660, L35 15, 30, 53

Kassin S. A., Weiner B., Faber S. M., et al 2012, ApJ, 758, 106 29, 30

Kelvin L. S., et al., 2012, MNRAS, 421, 1007 85

Kelvin L. S., et al., 2014, MNRAS, 444, 1647 37

Kennicutt Jr. R. C., 1998, ApJ, 498, 541 xxi, 96, 97

Kleiner D., Pimbblet K. A., Jones D. H., Koribalski B. S., Serra P., 2017, MNRAS, 466, 4692 47

Klessen R. S., Hennebelle P., 2010, A&A, 520, A17 71

Klypin A., Gottlöber S., Kravtsov A. V., Khokhlov A. M., 1999, ApJ, 516, 530 3

Kormendy J., 1977, ApJ, 218, 333 7, 28

Kormendy J., Fisher D. B., Cornell M. E., Bender R., 2009, ApJS, 182, 216 7

Krumholz M. R., Burkhart B., 2016, Monthly Notices of the Royal Astronomical Society, 458, 1671 71, 106

Krumholz M. R., Burkhart B., Forbes J. C., Crocker R. M., 2018, MNRAS, 477, 2716 105, 106

Kuehn K., et al., 2014, in Ramsay S. K., McLean I. S., Takami H., eds, Society of Photo-Optical Instrumentation Engineers (SPIE) Conference Series Vol. 9147, Ground-based and Airborne Instrumentation for Astronomy V. p. 914710, doi:10.1117/12.2055677 116

Lacey C., Cole S., 1993, MNRAS, 262, 627 3

Lagos C. d. P., et al., 2017, preprint, (`arXiv:1701.04407`) 29, 72

Lagos C. d. P., et al., 2018, MNRAS, 473, 4956 72

Leavitt H. S., 1908, Annals of Harvard College Observatory, 60, 87 4

Lee Y. H., Ann H. B., Park M.-G., 2019, ApJ, 872, 97 9

Lees J. F., Knapp G. R., Rupen M. P., Phillips T. G., 1991, ApJ, 379, 177 7, 47

Lehnert M. D., Nesvadba N. P. H., Le Tiran L., Di Matteo P., van Driel W., Douglas L. S., Chemin L., Bournaud F., 2009, ApJ, 699, 1660 71, 106

Lehnert M. D., Le Tiran L., Nesvadba N. P. H., van Driel W., Boulanger F., Di Matteo P., 2013, A&A, 555, A72 71, 106

Lelli F., Verheijen M., Fraternali F., 2014, A&A, 566, A71 15, 67

Lelli F., McGaugh S. S., Schombert J. M., 2016, ApJ, 816, L14 15, 67

Lelli F., McGaugh S. S., Schombert J. M., Desmond H., Katz H., 2019, MNRAS, 484, 3267 10

Lemaître G., 1931, MNRAS, 91, 483 2

Lenz D. D., Ayres T. R., 1992, PASP, 104, 1104 127

Lidman C., et al., 2020, MNRAS, 496, 19 113, 115

Lim S., et al., 2020, ApJ, 899, 69 12

Marinacci F., Sales L. V., Vogelsberger M., Torrey P., Springel V., 2019, MNRAS, 489, 4233 64

Martimbeau N., Carignan C., Roy J. R., 1994, AJ, 107, 543 10

Masters K. L., Springob C. M., Huchra J. P., 2008, AJ, 135, 1738 11

Mateo M. L., 1998, ARA&A, 36, 435 12

Matthews L. D., van Driel W., Gallagher J. S. I., 1998, AJ, 116, 2196 67

McGaugh S. S., 2005, ApJ, 632, 859 15, 67

McGaugh S. S., 2012, AJ, 143, 40 67, 68

McGaugh S. S., Wolf J., 2010, ApJ, 722, 248 67

McGaugh S. S., Schombert J. M., Bothun G. D., de Blok W. J. G., 2000, ApJ, 533, L99 14, 15, 28, 67, 69

Menon S. H., Federrath C., Kuiper R., 2020, MNRAS, 493, 4643 107

Metropolis N., Rosenbluth A. W., Rosenbluth M. N., Teller A. H., Teller E., 1953, The

Journal of Chemical Physics, 21, 1087 95

Milgrom M., 1983, ApJ, 270, 371 67

Mitchell P. D., et al., 2018, MNRAS, 474, 492 72

Mo H. J., White S. D. M., 1996, MNRAS, 282, 347 3

Mo H. J., Mao S., White S. D. M., 1998, MNRAS, 295, 319 67, 72

Mo H., van den Bosch F. C., White S., 2010, Galaxy Formation and Evolution. Cambridge University Press 2, 3, 6, 9, 10

Moiseev A. V., Tikhonov A. V., Klypin A., 2015, MNRAS, 449, 3568 105

Moore B., Governato F., Quinn T., Stadel J., Lake G., 1998, ApJ, 499, L5 3

Moster B. P., Somerville R. S., Maulbetsch C., van den Bosch F. C., Macciò A. V., Naab T., Oser L., 2010, ApJ, 710, 903 102, 103, 104

Moster B. P., Naab T., White S. D. M., 2013, MNRAS, 428, 3121 68

Navarro J. F., Frenk C. S., White S. D. M., 1997, ApJ, 490, 493 3

Neistein E., Maoz D., Rix H.-W., Tonry J. L., 1999, AJ, 117, 2666 7, 29

Nicholls D. C., Dopita M. A., Jerjen H., Meurer G. R., 2011, AJ, 142, 83 65

Noeske K. G., et al., 2007, ApJ, 660, L43 71

Obreja A., Stinson G. S., Dutton A. A., Macciò A. V., Wang L., Kang X., 2016, MNRAS, 459, 467 72

Obreschkow D., Glazebrook K., 2014a, ApJ, 784, 26 29

Obreschkow D., Glazebrook K., 2014b, ApJ, 784, 26 72

Obreschkow D., Glazebrook K., Kilborn V., Lutz K., 2016, ApJ, 824, L26 72

Oh S.-H., et al., 2015, AJ, 149, 180 67

Oh S., et al., 2016, ApJ, 832, 69 68

Oke J. B., Gunn J. E., 1983, ApJ, 266, 713 66

Ouellette N. N., Courteau S., Holtzman J. A., Dutton A. A., et al 2017, ApJ, 843, 74 29

Owers M. S., et al., 2017, MNRAS, 468, 1824 31, 33, 85

Pacifici C., Charlot S., Blaizot J., Brinchmann J., 2012, MNRAS, 421, 2002 114

Padoan P., Federrath C., Chabrier G., Evans N. J. I., Johnstone D., Jørgensen J. K., McKee C. F., Nordlund Å., 2014, in Beuther H., Klessen R. S., Dullemond C. P., Henning T., eds, Protostars and Planets VI. p. 77 (`arXiv:1312.5365`), doi:10.2458/azu_uapress_9780816531240-ch004 71

Park H. S., Moon D.-S., Zaritsky D., Kim S. C., Lee Y., Cha S.-M., Lee Y., 2019, ApJ, 885, 88 12

Pasquini L., et al., 2002, The Messenger, 110, 1 21, 76

Peebles P. J. E., 1969, ApJ, 155, 393 29

Penny S. J., Conselice C. J., de Rijcke S., Held E. V., 2009, MNRAS, 393, 1054 69

Perlmutter S., et al., 1999, ApJ, 517, 565 2

Pickles A. J., 1998, PASP, 110, 863 123

Pizagno J., Prada F., Weinberg D., et al 2005, ApJ, 633, 844 28

Pizagno J., et al., 2007, AJ, 134, 945 14

Poci A., Cappellari M., McDermid R. M., 2017, MNRAS, 467, 1397 104

Pogge R. W., Eskridge P. B., 1993, AJ, 106, 1405 10

Pohlen M., Trujillo I., 2006, A&A, 454, 759 9

Ponomareva A. A., Verheijen M. A. W., Peletier R. F., Bosma A., 2017, MNRAS, 469, 2387 11, 67

Popesso P., et al., 2019, MNRAS, 483, 3213 76

Porter T. A., Johnson R. P., Graham P. W., 2011, ARA&A, 49, 155 12

Posti L., Pezzulli G., Fraternali F., Di Teodoro E. M., 2018a, MNRAS, 475, 232 72

Posti L., Fraternali F., Di Teodoro E. M., Pezzulli G., 2018b, A&A, 612, L6 72, 73

Posti L., Marasco A., Fraternali F., Famaey B., 2019, A&A, 629, A59 72

Pota V., et al., 2013, MNRAS, 428, 389 7

Prugniel P., Simien F., 1996, A&A, 309, 749 8

Prugniel P., Simien F., 1997, A&A, 321, 111 8

Renzini A., Ciotti L., 1993, ApJ, 416, L49 8

Renzini A., Peng Y.-j., 2015, ApJ, 801, L29 71, 76

Riess A. G., et al., 1998, AJ, 116, 1009 2

Robaina A. R., et al., 2009, ApJ, 704, 324 70

Roberts M. S., 2008, in Bridle A. H., Condon J. J., Hunt G. C., eds, Astronomical Society of the Pacific Conference Series Vol. 395, Frontiers of Astrophysics: A Celebration of NRAO's 50th Anniversary. p. 283 11

Robotham A. S. G., Obreschkow D., 2015, Publications of the Astronomical Society of Australia, 32 42

Romanowsky A. J., Fall S. M., 2012, ApJS, 203, 17 72

Rownd B. K., Dickey J. M., Helou G., 1994, AJ, 108, 1638 10

Royer F., Blecha A., North P., Simond G., Baratchart S., Cayatte V., Chemin L., Palsa R., 2002, in Starck J.-L., Murtagh F. D., eds, Society of Photo-Optical Instrumentation Engineers (SPIE) Conference Series Vol. 4847, Proc. SPIE. pp 184–194, doi:10.1117/12.460552 78, 80

Ryan-Weber E. V., Webster R. L., Staveley-Smith L., 2003, MNRAS, 343, 1195 10

Saglia R. P., Bertschinger E., Baggley G., Burstein D., Colless M., Davies R. L., McMahan

Robert K. J., Wegner G., 1997, ApJS, 109, 79 7

Said K., Kraan-Korteweg R. C., Jarrett T. H., 2015, MNRAS, 447, 1618 68

Sales L. V., et al., 2017, MNRAS, 464, 2419 67

Salim S., et al., 2007, ApJS, 173, 267 72

Sánchez S. F., 2020, ARA&A, 58, annurev 20, 21

Sánchez S. F., et al., 2012, A&A, 538, A8 20

Sánchez S. F., et al., 2013, A&A, 554, A58 30

Sandage A., 2005, ARA&A, 43, 581 6

Sandage A., Binggeli B., 1984, AJ, 89, 919 6, 12

Sandage A., Visvanathan N., 1978, ApJ, 225, 742 7

Sanders R. H., 1990, A&ARv, 2, 1 67

Saulder C., Steer I., Snaith O., Park C., 2019, arXiv e-prints, p. arXiv:1905.12970 9

Schawinski K., et al., 2014, MNRAS, 440, 889 10

Schaye J., et al., 2015, MNRAS, 446, 521 13, 64

Schlafly E. F., Finkbeiner D. P., 2011, ApJ, 737, 103 7

Scodeggio M., Gavazzi G., Franzetti P., Boselli A., Zibetti S., Pierini D., 2002, A&A, 384, 812 72

Scott N., et al., 2015, MNRAS, 451, 2723 134

Scott N., et al., 2018, MNRAS, 481, 2299 20, 31, 32

Searle L., Zinn R., 1978, ApJ, 225, 357 64

Searle L., Sargent W. L. W., Bagnuolo W. G., 1973, ApJ, 179, 427 9

Serra P., Oosterloo T., Cappellari M., den Heijer M., Józsa G. I. G., 2016, MNRAS, 460, 1382 135

Shanks T., et al., 2015, MNRAS, 451, 4238 33

Sharp R., et al., 2006, in Society of Photo-Optical Instrumentation Engineers (SPIE) Conference Series. p. 62690G (`arXiv:astro-ph/0606137`), doi:10.1117/12.671022 22, 31

Sharp R., et al., 2015, MNRAS, 446, 1551 32

Sheinis A., et al., 2014, in Ramsay S. K., McLean I. S., Takami H., eds, Society of Photo-Optical Instrumentation Engineers (SPIE) Conference Series Vol. 9147, Ground-based and Airborne Instrumentation for Astronomy V. p. 91470Y, doi:10.1117/12.2055595 115

Shen S., Mo H. J., White S. D. M., Blanton M. R., Kauffmann G., Voges W., Brinkmann J., Csabai I., 2003, MNRAS, 343, 978 76

Shostak G. S., 1978, A&A, 68, 321 10

Sil'chenko O. K., Moiseev A. V., Egorov O. V., 2019, ApJS, 244, 6 47

Simon J. D., 2019, ARA&A, 57, 375 12

Simons R. C., Kassin S. A., Weiner B. J., Heckman T. M., Lee J. C., Lotz J. M., Peth M., Tchernyshyov K., 2015, MNRAS, 452, 986 30

Smith G. A., et al., 2004, in Moorwood A. F. M., Iye M., eds, Society of Photo-Optical Instrumentation Engineers (SPIE) Conference Series Vol. 5492, Ground-based Instrumentation for Astronomy. pp 410–420, doi:10.1117/12.551013 115

Somerville R. S., Davé R., 2015, ARA&A, 53, 51 12

Speagle J. S., Steinhardt C. L., Capak P. L., Silverman J. D., 2014, ApJS, 214, 15 71

Springel V., et al., 2018, MNRAS, 475, 676 64

Stanford S. A., Eisenhardt P. R., Dickinson M., 1998, ApJ, 492, 461 7

Staszak N. F., et al., 2016, in Navarro R., Burge J. H., eds, Society of Photo-Optical Instrumentation Engineers (SPIE) Conference Series Vol. 9912, Advances in Optical and Mechanical Technologies for Telescopes and Instrumentation II. p. 991223, doi:10.1117/12.2233796 113

Stevens A. R. H., Croton D. J., Mutch S. J., 2016, MNRAS, 461, 859 72, 73

Straatman C. M. S., et al., 2017, ApJ, 839, 57 30

Strigari L. E., 2018, Reports on Progress in Physics, 81, 056901 12

Sweet S. M., Drinkwater M. J., Meurer G., Kilborn V., Audcent-Ross F., Baumgardt H., Bekki K., 2016, MNRAS, 455, 2508 69

Sweet S. M., Fisher D., Glazebrook K., Obreschkow D., Lagos C., Wang L., 2018, ApJ, 860, 37 72

Tamburro D., Rix H. W., Leroy A. K., Mac Low M. M., Walter F., Kennicutt R. C., Brinks E., de Blok W. J. G., 2009, AJ, 137, 4424 71

Tapia T., Eliche-Moral M. C., Aceves H., Rodríguez-Pérez C., Borlaff A., Querejeta M., 2017, A&A, 604, A105 68

Tasker E. J., Tan J. C., 2009, ApJ, 700, 358 71

Taylor E. N., et al., 2011, MNRAS, 418, 1587 22, 84

Thomas H. C., Alexander P., Clemens M. S., Green D. A., Dunne L., Eales S., 2004, MNRAS, 351, 362 102

Thomas D., Maraston C., Bender R., Mendes de Oliveira C., 2005, ApJ, 621, 673 7

Thomas D., Maraston C., Johansson J., 2011, MNRAS, 412, 2183 77

Thorp M. D., Ellison S. L., Simard L., Sánchez S. F., Antonio B., 2019, MNRAS, 482, L55 70

Tiley A. L., et al., 2019, MNRAS, 482, 2166 134

Tody D., 1986, in Crawford D. L., ed., Society of Photo-Optical Instrumentation Engineers (SPIE) Conference Series Vol. 627, Instrumentation in astronomy VI. p. 733, doi:10.1117/12.968154 113

Tolstoy E., Hill V., Tosi M., 2009, ARA&A, 47, 371 65

Tonini C., Jones D. H., Mould J., Webster R. L., Danilovich T., Ozbilgen S., 2014, MNRAS, 438, 3332 14, 29

Tortora C., La Barbera F., Napolitano N. R., de Carvalho R. R., Romanowsky A. J., 2012, MNRAS, 425, 577 8

Trager S. C., Faber S. M., Worthey G., González J. J., 2000, AJ, 119, 1645 7

Tremmel M., Karcher M., Governato F., Volonteri M., Quinn T. R., Pontzen A., Anderson L., Bellovary J., 2017, MNRAS, 470, 1121 64

Tremonti C. A., et al., 2004, ApJ, 613, 898 72

Trujillo I., Burkert A., Bell E. F., 2004, ApJ, 600, L39 8

Trujillo I., Roman J., Filho M., Sánchez Almeida J., 2017, ApJ, 836, 191 12

Tully R. B., Fisher J. R., 1977, A&A, 500, 105 11, 28, 67

Varidel M. R., et al., 2020, arXiv e-prints, p. arXiv:2005.04874 105, 107

Vazdekis A., Sánchez-Blázquez P., Falcón-Barroso J., Cenarro A. J., Beasley M. A., Cardiel N., Gorgas J., Peletier R. F., 2010, MNRAS, 404, 1639 114

Vogelsberger M., et al., 2014, Nature, 509, 177 13

Vogelsberger M., Marinacci F., Torrey P., Puchwein E., 2019, arXiv e-prints, p. arXiv:1909.07976 65

Walch S. K., Whitworth A. P., Bisbas T., Wünsch R., Hubber D., 2012, MNRAS, 427, 625 107

Warren M. S., Quinn P. J., Salmon J. K., Zurek W. H., 1992, ApJ, 399, 405 3

Wechsler R. H., Tinker J. L., 2018, ARA&A, 56, 435 3

Weijmans A.-M., et al., 2014, MNRAS, 444, 3340 39

Weiner B. J., Willmer C. N. A., Faber S. M., 2006, ApJ, 653, 1027 15, 30, 51, 68

Williams M. J., Bureau M., Cappellari M., 2010, MNRAS, 409, 1330 29

Yegorova I. A., Salucci P., 2007, MNRAS, 377, 507 93

Young L. M., 2002, AJ, 124, 788 7, 47

Young J. S., Scoville N. Z., 1991, ARA&A, 29, 581 10

Young L. M., et al., 2011, MNRAS, 414, 940 7, 47

Yu X., et al., 2019, MNRAS, 486, 4463 106, 107

Yuan F., et al., 2015, MNRAS, 452, 3047 113, 115

Zaritsky D., et al., 2014, AJ, 147, 134 14

Zhao G., Zhao Y.-H., Chu Y.-Q., Jing Y.-P., Deng L.-C., 2012, Research in Astronomy and Astrophysics, 12, 723 113

Zhou L., et al., 2017, MNRAS, 470, 4573 65, 71

Zwaan M. A., van der Hulst J. M., de Blok W. J. G., McGaugh S. S., 1995, MNRAS, 273, L35 14

da Cunha E., et al., 2017, Publ. Astron. Soc. Australia, 34, e047 9, 18, 24, 113, 137

de los Reyes M. A. C., Kennicutt Robert C. J., 2019, ApJ, 872, 16 97

den Heijer M., et al., 2015, A&A, 581, A98 68

van Driel W., van Woerden H., 1994, A&A, 286, 395 10

van de Sande J., et al., 2017, ApJ, 835, 104 32, 33, 45, 91

van den Bergh S., 1976, ApJ, 206, 883 9

van der Burg R. F. J., Muzzin A., Hoekstra H., 2016, A&A, 590, A20 12